# Università degli Studi di Trieste

## Dipartimento di Fisica

Corso di Laurea Magistrale in Fisica

## Ottimizzazione dei rivelatori al diamante sui dati e studi di efficienza di tracciatura nell'esperimento Belle II

Candidato:
Riccardo Manfredi

Relatore:
Dott. Diego Tonelli

Corelatore:
Prof. Lorenzo Vitale

ANNO ACCADEMICO 2018–2019

# Università degli Studi di Trieste

## Dipartimento di Fisica

### Corso di Laurea Magistrale in Fisica

# Diamond-detector commissioning and tracking-efficiency studies in the Belle II experiment

Candidato:
Riccardo Manfredi

Relatore:
Dott. Diego Tonelli

Corelatore:
Prof. Lorenzo Vitale

ANNO ACCADEMICO 2018–2019

**Sommario**

Lo scopo di questo lavoro di fisica sperimentale delle particelle è ottimizzare e preservare le prestazioni di ricostruzione di particelle cariche dell'esperimento Belle II. Belle II è un rivelatore ottimizzato per la ricostruzione di miliardi di decadimenti di mesoni pesanti e leptoni $\tau$, prodotti in collisioni elettrone-positrone a 10 GeV, per cercare prove indirette di fisica oltre il Modello Standard.

La prima parte del lavoro consiste nel perfezionare le prestazioni del monitor di radiazione basato su rivelatori al diamante sintetico. Questo sistema protegge la parte più interna di Belle II da radiazioni dovute all'intensità dei fasci in collisione. Col mio lavoro sull'esperimento durante la delicata fase di inizio della presa dati, ho ottimizzato le prestazioni del sistema dei diamanti grazie ad efficaci procedure di controllo quotidiano, all'analisi e risoluzione di problemi inaspettati, ed analisi fondi di fascio. Parallelamente, ho proposto un metodo innovativo per misurare l'efficienza di tracciatura dell'esperimento, basato sui decadimenti $D^{*+} \rightarrow D^0[\rightarrow K_S^0(\rightarrow \pi^+\pi^-)\pi^+\pi^-]\pi^+$. L'idea fondamentale è che la bassa ($Q \simeq 7\,\mathrm{MeV}$) energia cinetica disponibile nella transizione $D^{*+} \rightarrow D^0\pi^+$ vincola sufficientemente la cinematica da rendere visibile un segnale nella distribuzione di differenza di massa $D^{*+} - D^0$ anche se un pione della $D^0$ non viene ricostruito. Il rapporto tra il numero di eventi ricostruiti completamente e quelli ricostruiti senza un pione determina l'efficienza di ricostruzione per il pione mancante.

Il mio lavoro ha portato ad un significativo miglioramento delle prestazioni del sistema dei diamanti, garantendo una presa dati più fluida ed efficiente, e maggior sicurezza per i rivelatori più interni; ha inoltre introdotto in Belle II un approccio innovativo alla determinazione dell'efficienza di tracciatura, basato unicamente sui dati, che estende la misura ad impulsi finora inaccessibili, affiancando e completando i metodi esistenti.

**Abstract**

This is an experimental particle-physics thesis aimed at preserving and optimizing the charged-particle tracking performance of the Belle II experiment. Belle II is a detector designed to reconstruct billions of decays of heavy mesons and $\tau$ leptons from 10 GeV electron-positron collisions in search for indirect indications of non-Standard-Model physics.

The first part of the work focuses on the data-commissioning of the radiation-monitoring system based on synthetic-diamond sensors. Diamonds protect the inner subdetectors from radiation due to the intense colliding beams. As a local expert in Japan during the critical phase of early data taking, I optimized diamond operations by providing daily maintenance, analysis and troubleshooting of unexpected events, operation improvements, and beam-background analyses. The second part describes a novel method I proposed for determining the charged-particle finding efficiency, based on $D^{*+} \rightarrow D^0[\rightarrow K_S^0(\rightarrow \pi^+\pi^-)\pi^+\pi^-]\pi^+$ decays. The key idea is that the small ($Q \simeq 7\,\mathrm{MeV}$) kinetic energy available in the $D^{*+} \rightarrow D^0\pi^+$ transition imposes sufficient kinematic constraints to distinguish a signal in the $D^{*+} - D^0$ mass-difference even if one pion from the $D^0$ decay is not reconstructed. The ratio between yields of fully reconstructed decays and decays reconstructed without that pion determines the efficiency for reconstructing the unbiased pion.

My work resulted in significantly streamlined and improved operations of the diamond system, ensuring smoother, more efficient data taking, and significantly safer conditions for the tracking detectors. In addition, it introduces in Belle II an innovative approach to determine the track-finding efficiency that relies only on data and probes previously inaccessible ranges in momentum, complementing and supplementing existing methods.

# Contents

# Introduction

The Standard Model of elementary particles and their interactions (SM) is the currently accepted theory of particle physics. It is often recognized as the ultimate success of the reductionist paradigm for describing microphysics at its most fundamental level: by means of less than twenty parameters, it describes accurately thousands of measurements involving processes mediated by the electromagnetic, weak, and strong interactions that span many orders of magnitude in energy. However, theoretical considerations and experimental inconsistencies support the general prejudice that the Standard Model might still be an effective theory valid at the energies probed so far, that is incorporated in a yet-unknown, more general theory. Completing the Standard Model is the main goal of today's particle physics.

A "direct" approach, which broadly consists in searching for decay products of non-SM particles produced on mass-shell in high-energy collisions, has been traditionally fruitful. However, its current reach is limited by the available energy of today's colliders and by the large investments needed to further it in the near future. A complementary approach consists in performing precise measurements in lower-energy processes where virtual non-SM particles could contribute, such as the weak interactions of quarks, and searching for deviations of experimental results from theory predictions. Such "indirect" approach is not constrained by collision energy, but rather by the precision attainable, both in measurements and predictions.

The Belle II experiment is an international collaboration of more than 800 physicists that aims at indirectly testing the Standard Model by studying billions of decays of $\tau$ leptons (heaviest partners of the electron) and mesons containing the quarks $b$ and $c$ (heavier and longer-lived partners of the fundamental constituents of nuclear matter) produced in electron-positron collisions.

Precise reconstruction of final states is key in Belle II, especially those containing charged particles, which make for a large fraction of the decay channels sensitive to non-SM physics. Good performance in reconstructing the trajectories of charged particles (tracks) offer both precise invariant-mass reconstruction, which enhances separation between distinctively narrow signal peaks and smoothly distributed background, and determination of the time evolution of decays, an essential capability in many quark-flavor measurements.

My work is targeted at optimizing two distinct, but synergic, aspects of charged-particle tracking. I optimized the operating configuration of the diamond detector, which protects the tracking detectors from damaging radiation, and proposed and developed a novel original approach for determining track-finding efficiency.

The high collision frequency needed to produce data sets sufficiently large to achieve high experimental precision comes with significant radiation backgrounds, due to the intensity of the colliding beams. The innermost tracking detectors, based on semiconductor technology, may suffer performance degradation, or even irreversible damage, if the radiation field is not monitored and safety measures not implemented. This is the goal of the

radiation-monitoring and beam-abort system, an array of 28 synthetic-diamond $1 \times 1$ cm$^2$ sensors installed on the beam pipe and on the inner layers of the tracking detector. Diamond sensors work as solid-state drift chambers offering great sensitivity to charged and neutral radiation across a broad energy spectrum, which makes them ideally suited for radiation monitoring. While stationed three months in Japan, I led the start-up and early operations of the system during first physics collisions. The goal was to understand and optimize its performances to ensure smooth, efficient, and safe operations of the silicon tracker. In the second part of the work, I developed a novel method for determining the tracking efficiency of the Belle II detector using charm decays that requires no direct input from simulation, and probes a kinematic range inaccessible to previous standard approaches.

This thesis is structured as follows: Chapter 1 outlines the physics of the flavor sector of the Standard Model; in Chapter 2 the Belle II experiment is described, focusing on charged-particle tracking; Chapter 3 describes my work on the diamond-detector-based radiation-monitoring system; in Chapter 4 my work for developing a novel method for determining track-finding efficiency is presented.

The work of this thesis is being documented in one internal Belle II document and two technical papers in preparation.

# Chapter 1

# Flavor Physics to overcome the Standard Model

I begin with a concise introduction to the weak interactions of quarks (flavor physics) and how they are incorporated in the Standard Model of particle physics. Then, I outline the main concepts subtending the use of flavor physics to search for as-yet unknown particles that may complete the Standard Model at high energies.

## 1.1 The Standard Model of particle physics

The Standard Model is a quantum field theory that describes three of the four fundamental interactions in nature (gravity is not included). Particles and their interactions are described in a Lagrangian formalism, in which every term that is not forbidden by the symmetries of the dynamics is, in principle, included. Local gauge symmetry, i.e., the invariance of the Lagrangian under space-time-dependent transformations applied to the phases of fields, is the key overarching concept. Interaction terms appear in the free-field Lagrangian after requiring it to be invariant under local gauge symmetries. The Standard Model is based on the symmetry group

$$SU_C(3) \otimes SU_L(2) \otimes U_Y(1),$$

where $SU_C(3)$ is the standard unitary group that describes the strong interactions (quantum chromodynamics, QCD), and $C$ stands for color, while $SU_L(2) \otimes U_Y(1)$ is the product of groups that describe the combination of weak and electromagnetic interactions, $L$ stands for *left* and $Y$ stands for *hypercharge*. The group $SU_C(3)$ has 8 generators, $SU_L(2)$ has 3 generators $W_{1,2,3}$, and $U_Y(1)$ has only one, $B$. Elementary particles are excitations of fields: matter particles correspond to spin-$\frac{1}{2}$ fields and are called *fermions*, while interactions are mediated by spin-1 particles called *gauge bosons*. Particles acquire mass via the interaction with the Higgs field, mediated by a spin-0 particle, the Higgs boson.

Strong interactions occur between quarks, the fundamental constituents of nuclear matter, and are mediated by eight massless bosons corresponding to the $SU_C(3)$ generators; they are called *gluons* and carry a charge that can be of three kinds, called *color*. Weak interactions occur between all particles and are mediated by two charged massive bosons, $W^{\pm}$, and a neutral massive boson, $Z^0$. Electromagnetic interactions occur between particles carrying electric charge and are mediated by a neutral massless boson, the photon $\gamma$.

The electroweak physical bosons ($W^\pm$, $Z^0$, $\gamma$) arise from the following linear combinations of $SU_L(2) \otimes U_Y(1)$ generators:

$$W^\pm = \frac{1}{\sqrt{2}}(W_1 \mp iW_2) \ \ \text{and} \ \ \begin{pmatrix} \gamma \\ Z^0 \end{pmatrix} = \begin{pmatrix} \cos(\theta_W) & \sin(\theta_W) \\ -\sin(\theta_W) & \cos(\theta_W) \end{pmatrix} \begin{pmatrix} B \\ W_3 \end{pmatrix},$$

where $\theta_W$ is a free parameter, called *Weinberg angle*. Fermion masses are free parameters of the model, while the $W^\pm$ mass depends from the $Z$ mass via $\theta_W$.

Each fermion is also associated with an anti-particle, that has the same mass and opposite internal quantum numbers. Fermions are classified into two families, quarks and leptons, each organized in weak-isospin doublets as follows:

- Lepton doublets are composed each by a massless neutral neutrino and a massive particle with electric charge $-e$;

$$\begin{pmatrix} \nu_e \\ e \end{pmatrix} \begin{pmatrix} \nu_\mu \\ \mu \end{pmatrix} \begin{pmatrix} \nu_\tau \\ \tau \end{pmatrix} .$$

  They couple only with the electroweak interaction. Each lepton has a quantum number, so-called "lepton family number"; the global lepton number, which is the sum of the three of them, is found to be conserved in all interactions although no symmetry of the dynamics prescribes that; individual lepton numbers are not conserved in some processes, notably neutrino oscillations.

- Quark doublets are composed each of an up-type quark, with charge $\frac{2}{3}e$, and a down-type quarks, with charge $-\frac{1}{3}e$,

$$\begin{pmatrix} u \\ d \end{pmatrix} \begin{pmatrix} c \\ s \end{pmatrix} \begin{pmatrix} t \\ b \end{pmatrix} .$$

  Each quark has a quantum number, called "flavor", which comes in six varieties and is conserved in the electromagnetic and strong interactions but not in the weak interactions, and another quantum number, called "color" (three types). Due to color confinement [1] free quarks are not observable. They are only observed in their colorless bound states, which include mesons, typically composed of a quark and an anti-quark, and baryons, composed of three quarks. Baryons are assigned a quantum number, called "baryon number", found to be conserved even if no symmetry of the Lagrangian requires that.

Figure 1.1 shows a scheme of the Standard Model particles and the interactions among them.

In addition to gauge symmetry, discrete symmetries are important in defining the dynamics. Parity ($\mathcal{P}$) is a transformation that reverts all spatial coordinates, charge conjugation ($\mathcal{C}$) is the exchange of every particle with its own anti-particle, and time reversal ($\mathcal{T}$) inverts the time axis. The product of the discrete symmetries is found to be conserved in all interactions, but they are not conserved individually. The $\mathcal{P}$ symmetry is maximally violated in the weak interactions, while the $\mathcal{CP}$ combined symmetry is violated in weak interactions [2, 3] at the 0.1% level. In principle, the strong interaction too could violate $\mathcal{CP}$ symmetry, but no experimental evidence of that has ever been observed. The existence of as-yet unobserved particles (axions) has been postulated to account for that.
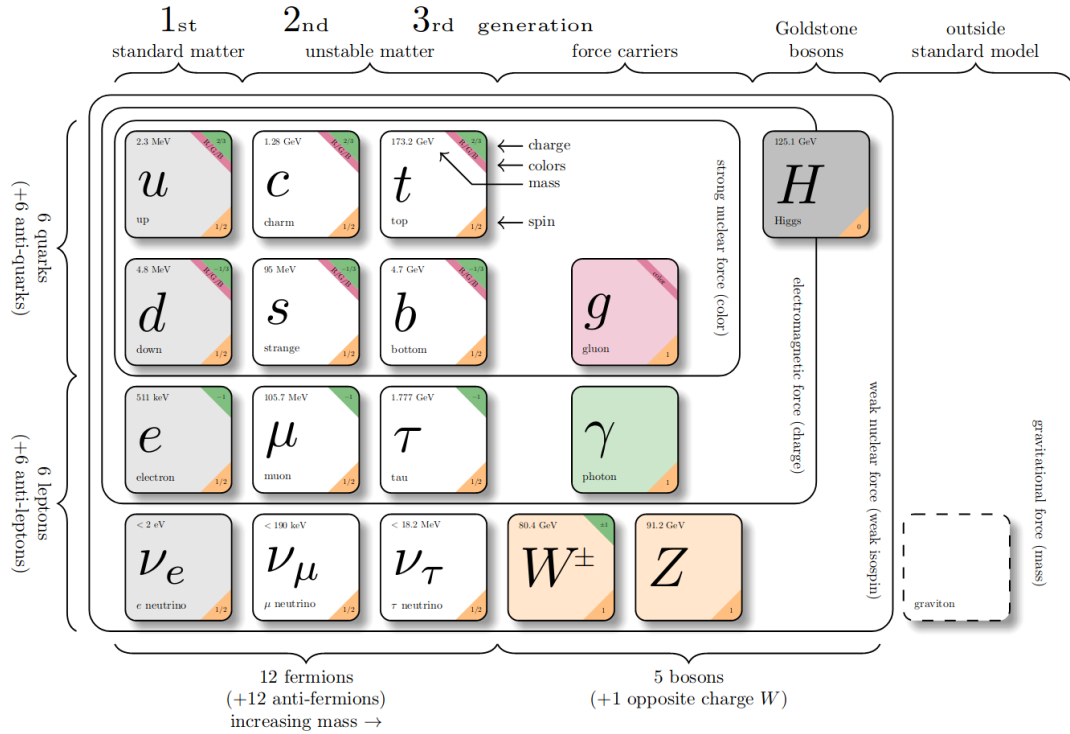
Figure 1.1: Scheme of particles and interactions in the Standard Model.

## 1.2   Landscape

The Standard Model was completed in the 1970's and has been successfully tested since, in thousands of different measurements whose precisions reach $O(10^{-12})$ [4]. However, observations and theoretical considerations suggest that the Standard Model is likely to be an effective theory, valid at the eV-TeV energies probed so far, but that should be completed by a more general "full theory" valid over a broader range of energies. Examples of open questions that support this prejudice include the missing explanation of a dynamical origin for the observed asymmetry between matter and antimatter in the universe, the strikingly large differences observed between fermion masses, or the postulated large amounts of non interacting matter (dark matter), introduced to justify cosmological observations.

Extending the Standard Model to higher energy-scales is the main goal of today's particle physics, as it is believed that such extensions may address these and other open issues. Current strategies to achieve that can broadly be classified into two complementary approaches. The energy-frontier, *direct approach* aims to use high-energy collisions to produce on-shell particles not included in the SM and directly detect their decay products, thus gaining direct evidence of their existence. Historically this has offered striking experimental evidence of new phenomena, when energetically accessible, but its reach is limited by the maximum available energy in colliders. The intensity-frontier, *indirect approach* broadly consists in searching for significant differences between precise measurement and equally precise SM predictions of lower-energy processes sensitive to non-SM contributions. The idea is that exchanges of virtual (off-mass-shell) particles of arbitrary high mass can occur in the amplitude thus altering the process rates in an observable manner. Experimental evidence is typically harder to establish, but the reach is not bounded by the maximum collision energy reachable by experiments. A large portion of the effort in this approach is centered on the weak-interactions of quarks (so called "flavor sector").

5

## 1.3   Flavor physics in the Standard Model

Although technically the flavor sector includes also lepton flavor, in this work I will restrict its meaning by referring solely to the quark interactions.

The role of flavor in shaping the Standard Model has been fundamental since the early days of particle physics. However, its preminence in determining the theory can perhaps be tracked down to the early 1960's with the apparent inconsistency between weak coupling constants measured in muon decay, neutron decay, and strange-particle decays. Such inconsistency was first addressed by Gell-Mann and Levy [5] and then Cabibbo [6], who postulated differing mass ($d$) and weak ($d'$) eigenstates for down-type quarks. This was implemented by introducing a mixing angle ($\theta_C$) between the $s$-quark and $d$-quark, the only two down-type quarks known at the time. While Cabibbo's theory addressed the difference of weak coupling constants, it also predicted a rate for the $K^0 \to \mu^+\mu^-$ decay much higher than the experimental exclusion limits at the time. Glashow, Iliopoulos, and Maiani addressed the inconsistency by postulating the existence of a fourth quark ($c$) of mass of about $2\,\mathrm{GeV}/c^2$, whose contribution in the $K^0 \to \mu^+\mu^-$ decay amplitude would cancel the $u$-quark contribution, suppressing the branching fraction to values consistent with experimental limits [7]. In the early 1970's, when only three quarks were known, Kobayashi and Maskawa generalized Cabibbo's theory from a four-quark model to a six-quark model to accommodate the observed phenomenon of $\mathcal{CP}$ violation [8]. They introduced a matrix to describe the relation between mass and weak quark eigenstates as seen by $W^\pm$ bosons. This is known as the "Cabibbo-Kobayashi-Maskawa quark-mixing matrix" or $V_{\mathrm{CKM}}$, a complex matrix that is unitary because the sum of all the transition probabilities must equal one. The $N \times N$ CKM matrix has $(N-1)^2$ free parameters [9], where $N$ is the number of quarks families. If $N = 2$, the only free parameter is the Cabibbo angle $\theta_C$, whereas if $N = 3$, the free parameters are three Euler angles ($\theta_{12}$, $\theta_{13}$, and $\theta_{23}$) and a complex phase ($\delta$), which allows for $\mathcal{CP}$-violating couplings. The matrix is written as

$$\begin{pmatrix} d' \\ s' \\ b' \end{pmatrix} = \begin{pmatrix} V_{ud} & V_{us} & V_{ub} \\ V_{cd} & V_{cs} & V_{cb} \\ V_{td} & V_{ts} & V_{tb} \end{pmatrix} \begin{pmatrix} d \\ s \\ b \end{pmatrix} \ ,$$

where $j'$ indicates the weak-interaction eigenstate of the $j$th quark and $j$ its mass eigenstate. The $V_{ij}$ matrix element expresses the coupling between any up-type $i$ quark and any down-type $j$ quark. Since the free parameters are only four, the $V_{\mathrm{CKM}}$ is conveniently written in the so-called *Wolfenstein parametrization* [10], an expansion in the small parameter $\lambda = \sin\theta_C \approx 0.23$ that makes explicit the observed hierarchy between its elements,

$$V_{\mathrm{CKM}} = \begin{pmatrix} 1 - \lambda^2/2 & \lambda & A\lambda^3(\rho - i\eta) \\ -\lambda & 1 - \lambda^2/2 & A\lambda^2 \\ A\lambda^3(1 - \rho - i\eta) & -A\lambda^2 & 1 \end{pmatrix} + \mathcal{O}(\lambda^4) \ ,$$

where

$$\lambda = \frac{V_{us}}{\sqrt{V_{ud}^2 + V_{us}^2}} \quad A\lambda^2 = \lambda\frac{V_{cb}}{V_{us}} \quad A\lambda^3(\rho + i\eta) = V_{ub}^* \ .$$

Parameter $\lambda$ encapsulates the mixing between the first and second quark generations, $A$ and $\rho$ are real parameters, and $\eta$ is a complex phase that allows for $\mathcal{CP}$ violation. The unitarity condition $V_{\mathrm{CKM}}V_{\mathrm{CKM}}^\dagger = \mathbb{1}$ yields nine relations,

$$|V_{ud}|^2 + |V_{cd}|^2 + |V_{td}|^2 = 1 \quad V_{us}^*V_{ud} + V_{cs}^*V_{cd} + V_{ts}^*V_{td} = 0 \quad V_{ud}V_{cd}^* + V_{us}V_{cs}^* + V_{ub}V_{cb}^* = 0 \; ,$$
$$|V_{us}|^2 + |V_{cs}|^2 + |V_{ts}|^2 = 1 \quad V_{ub}^*V_{ud} + V_{cb}^*V_{cd} + V_{tb}^*V_{td} = 0 \quad V_{ud}V_{td}^* + V_{us}V_{ts}^* + V_{ub}V_{tb}^* = 0 \; ,$$
$$|V_{ub}|^2 + |V_{cb}|^2 + |V_{tb}|^2 = 1 \quad V_{ub}^*V_{us} + V_{cb}^*V_{cs} + V_{tb}^*V_{ts} = 0 \quad V_{cd}V_{td}^* + V_{cs}V_{ts}^* + V_{cb}V_{tb}^* = 0 \; ,$$

which, as sums of complex numbers, prompt a convenient representation in terms of so-called *unitarity triangles* in the complex plane. A $\mathcal{CP}$ conserving theory would yield null-area triangles. All elements of the second equation in the middle column above have similar magnitudes and that equation is referred to as "The Unitarity Triangle", shown in Figure 1.2. Conventionally, side sizes are normalized to the length of the base, and the three angles are labelled $\alpha$ or $\phi_2$, $\beta$ or $\phi_1$, and $\gamma$ or $\phi_3$.

## 1.4 Flavor physics to overcome the standard model

Many physicists find our understanding of flavor dynamics and $\mathcal{CP}$ violation unsatisfactory. The observed hierarchies between quark masses and couplings seem too regular to be accidental and the abundance of free parameters (6 quark masses and 4 couplings) prompts the quest for a deeper, more fundamental theory with a possibly reduced set of parameters. In addition, while the CKM mechanism offers a framework to include $\mathcal{CP}$ violation in the SM, it does not really enlighten the origin for such a singular phenomenon. These and other considerations subtend the notion that a more detailed and complete study of the phenomenology of quarks dynamics and $\mathcal{CP}$ violation may reveal useful information to guide our search for Standard Model extensions.
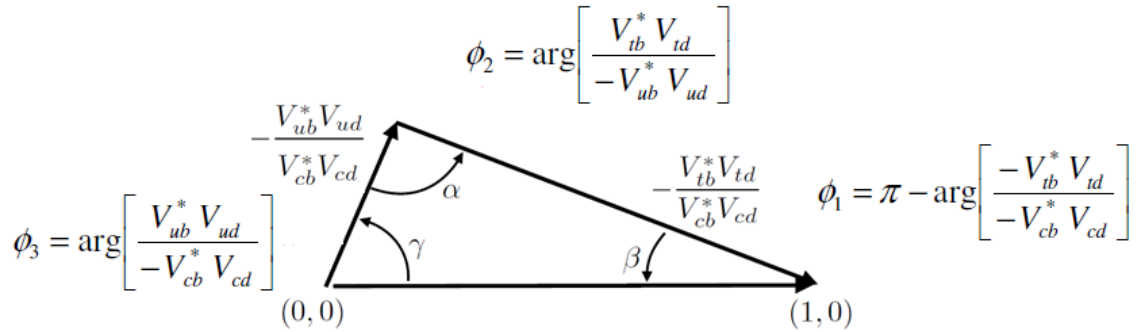


Figure 1.2: Graphical representation of the Unitarity Triangle.

The large abundance and diversity of experimentally accessible processes to measure redundantly a reduced set of parameters makes indirect searches in the flavor sector a powerful and promising option for exploring non-SM dynamics. In fact, even if no deviations from the Standard Model are found, the resulting stringent constraints on SM extensions are expected to inform future searches. The two classes of flavor-physics processes most promising for probing contributions of non-SM particles are *flavor-changing-neutral-currents* (FCNC) and $\mathcal{CP}-violating$ processes.

### 1.4.1 Flavor-changing neutral currents

Flavor-changing neutral currents are processes in which particle flavor changes but charge does not. The processes are suppressed in the Standard Model, because they are allowed

only through second-order amplitudes involving the internal exchange of $W^{\pm}$ bosons ("loop processes"), as shown in Fig. 1.3. They are naturally sensitive to non-SM contributions, since any particle with proper quantum number and nearly arbitrary mass can replace the SM-quarks closed-line in these diagrams thus enhancing the rate. FCNC can therefore be used to identify contribution from non-SM particles by measuring rate enhancement or suppressions with respect to Standard Model expectations.
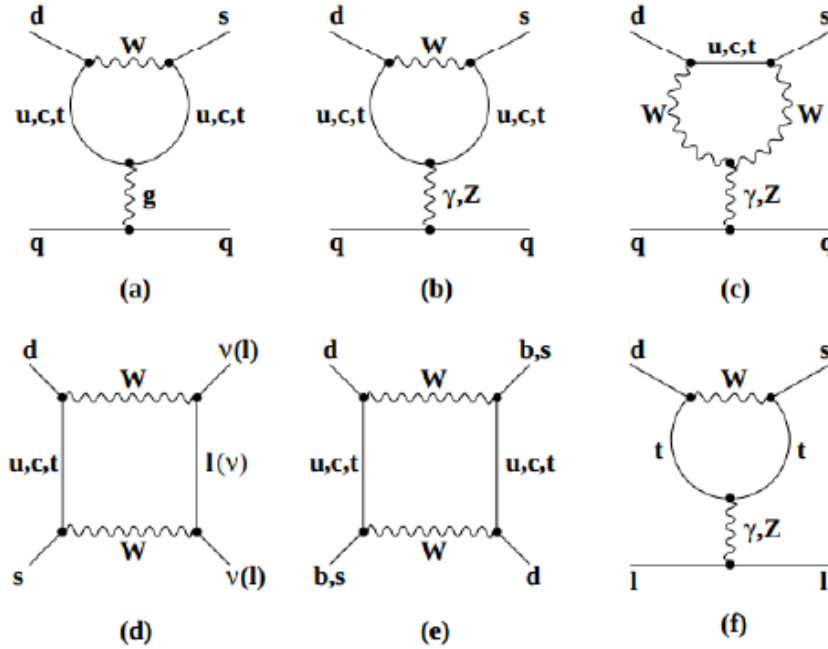


Figure 1.3: Examples of leading FCNC diagrams.

### 1.4.2  $\mathcal{CP}$ violation

Non-SM contributions may exist that do not change appreciably the rate of a process, but could introduce large biases in the amplitude phases. These can be identified by studying processes sensitive to $\mathcal{CP}$ violation, which allow comparing measurements of amplitude's phases and their theoretical predictions. The phenomenology is further enriched by the phenomenon of neutral meson mixing [11]. Neutral meson mixing are particle-antiparticle oscillation as a function of time that occur because the mass and the flavor eigenstate of neutral flavored mesons differ.

The experimental phenomenology of $\mathcal{CP}$ violation in hadrons is typically classified in three classes of phenomena:

- Direct $\mathcal{CP}$ violation (or $\mathcal{CP}$ violation in the decay amplitudes) occurs when the pure decay rate of the $X$ hadron ($X \to f$) and the rate of the $\mathcal{CP}-$conjugate ($\overline{X} \to \overline{f}$) differ. The observable typically used to measure it is the partial-width asymmetry

$$\mathcal{A}_f = \frac{\Gamma(X \to f) - \Gamma(\overline{X} \to \overline{f})}{\Gamma(X \to f) + \Gamma(\overline{X} \to \overline{f})} \; . \tag{1.1}$$

This is the only $\mathcal{CP}$-violating phenomenon possible for charged mesons and baryons.

- Indirect $\mathcal{CP}$ violation in mixing occurs when the probability of neutral-meson mixing from one state to its $\mathcal{CP}-$conjugate $(X^0 \rightarrow \overline{X}^0)$ differs from the $\mathcal{CP}-$conjugate process $(\overline{X}^0 \rightarrow X^0)$. The observable typically used is the semileptonic asymmetry

$$\mathcal{A}_{\mathrm{SL}} = \frac{d\Gamma\left(X^0(t) \rightarrow \overline{f}\right)/dt - d\Gamma\left(\overline{X}^0(t) \rightarrow f\right)/dt}{d\Gamma\left(X^0(t) \rightarrow \overline{f}\right)/dt + d\Gamma\left(\overline{X}^0(t) \rightarrow f\right)/dt} \ , \tag{1.2}$$

  where the final state $\overline{f}$ is chosen such that $X^0$ cannot directly decay into $f$ while its conjugate can and vice versa.

- If both particle and antiparticle decay into the same final state, indirect $\mathcal{CP}$ violation may occur between direct decays and decays following mixing, since the final state can be reached either from direct decay or from decay following oscillations. The observable used is

$$\mathcal{A}_{f_{\mathrm{CP}}} = \frac{d\Gamma(X^0(t) \rightarrow f_{CP})/dt - d\Gamma(\overline{X}^0(t) \rightarrow f_{CP})/dt}{d\Gamma(X^0(t) \rightarrow f_{CP})/dt + d\Gamma(\overline{X}^0(t) \rightarrow f_{CP})/dt} \ . \tag{1.3}$$

## 1.5 Current experimental status

Measurements of parameters associated with quark-flavor physics have been performed in many dedicated, or general-purpose, experiments in the last three decades, including CLEO, NA48, KTeV, OPAL, L3, ALEPH, DELPHI, BaBar, Belle, CDF, LHCb, Atlas, and CMS [12]. The resulting global picture is that the CKM interpretation of quark-flavor phenomenology is the dominant mechanism at play in the dynamics.

The current status of constraints on sides and angles of the Unitarity Triangle is shown in Fig. 1.4 [13]. Measurements of $\sin 2\beta$ reached a precision of 2.5 %, mainly due to the study of large samples of $B^0 \rightarrow J/\psi K_s^0$ decays in $e^+e^-$ collisions, while the angle $\alpha$ is known down to 5% precision from the decays $B \rightarrow \pi\pi$, $\pi\rho$, $\rho\rho$ in $e^+e^-$ and $pp$ collisions. The angle $\gamma$ is measured with 7% precision using combinations of several measurements involving $B \rightarrow DK$ decays reconstructed in $e^+e^-$ and $pp$ collisions. Mild discrepancies in the determinations of $|V_{cb}|$ and $|V_{ub}|$ are found between values measured in different semileptonic decays, mainly performed in $e^+e^-$ collisions.

The decay width difference of the $B_s^0 - \overline{B_s^0}$ system is determined with 6% precision in $pp$ collisions, while measurements are not yet precise enough to discern the expected non-zero value for the $B^0 - \overline{B}^0$ system. Mass differences in both systems are known with 1% precision from $pp$ and $p\overline{p}$ collisions. In addition, many other measurements in charm and kaon physics contribute that are not straightforwardly represented in the Unitarity Triangle. One example is the recent observation of direct $\mathcal{CP}$ violation in charm decays at LHCb [14].

Direct searches for non-SM physics, mainly at the Large Hadron $p\overline{p}$ Collider (LHC) at CERN, have excluded large portions of the parameter space for several proposed SM extensions, but showed no conclusive evidence of non-SM physics so far. Since plans for a higher-energy collider in the near future are still fluid, flavor physics makes up for the most promising instrument to search for non-SM in the next decade. In fact, despite the first-order consistency of the experimental flavor picture with the CKM theory, possible deviations of up to 10-15 % are still unconstrained, leaving sufficient room for non-SM physics to appear. It is especially promising that most of the relevant flavor-physics measurements are currently dominated by statistical uncertainties, offering therefore a fruitful
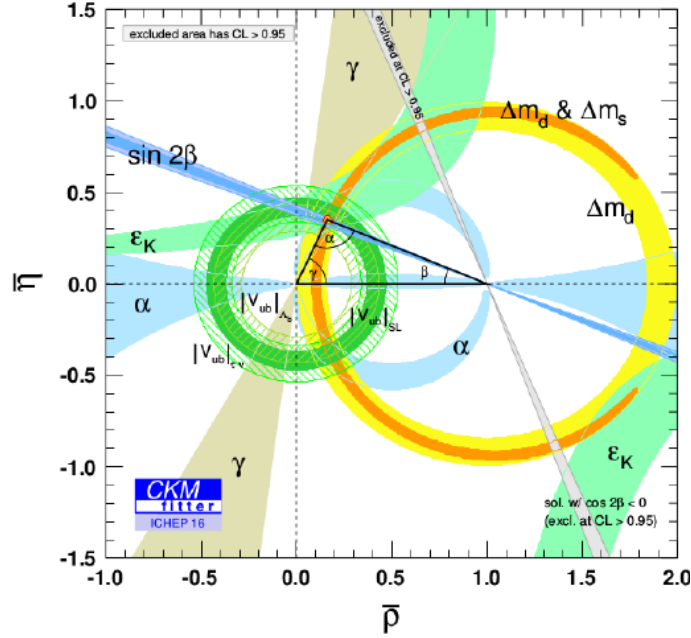
Figure 1.4: Current constrains on sides and angles values of the Unitarity Triangle.

landscape of opportunities for the two main experiments that will contribute in the next decay, LHCb and Belle II.

LHCb is a forward spectrometer that operates at the LHC. It studies proton-proton collisions at energies up to 14 TeV where incoherent QCD production yields large samples of $b\bar{b}$ pairs ($\approx 45\,\mathrm{kHz}$) and $c\bar{c}$ pairs ($\approx 1\,\mathrm{MHz}$). The high production rate allows for low statistical uncertainties, and TeV collision energy leads to the production of all species of $b-$hadrons, and therefore to the possibility of investigating a broader amount of processes. LHCb drawbacks are large backgrounds associated with composite-particle collisions, which require challenging online selections, and the fact that the collision energy occurs between proton constituents whose energy is not known, resulting in looser constraints on the production kinematics.

Belle II is an experiment operating at the energy asymmetric $e^+e^-$ collider SuperKEKB at KEK, which produces $B\overline{B}$ pairs from $\Upsilon(4S)$ decays at $\approx 1\,\mathrm{kHz}$ rate. Compared to LHCb, Belle II has a lower production rate but a better sensitivity to $B$ and $D$ final states that include neutral particles, because of the much lower background and additional kinematic constraints provided by the point-like nature of colliding particles. Belle II aims to operate for the next years at the intensity frontier of the flavor sector to explore indirectly of non-SM physics, in competition and synergy with LHCb [15].
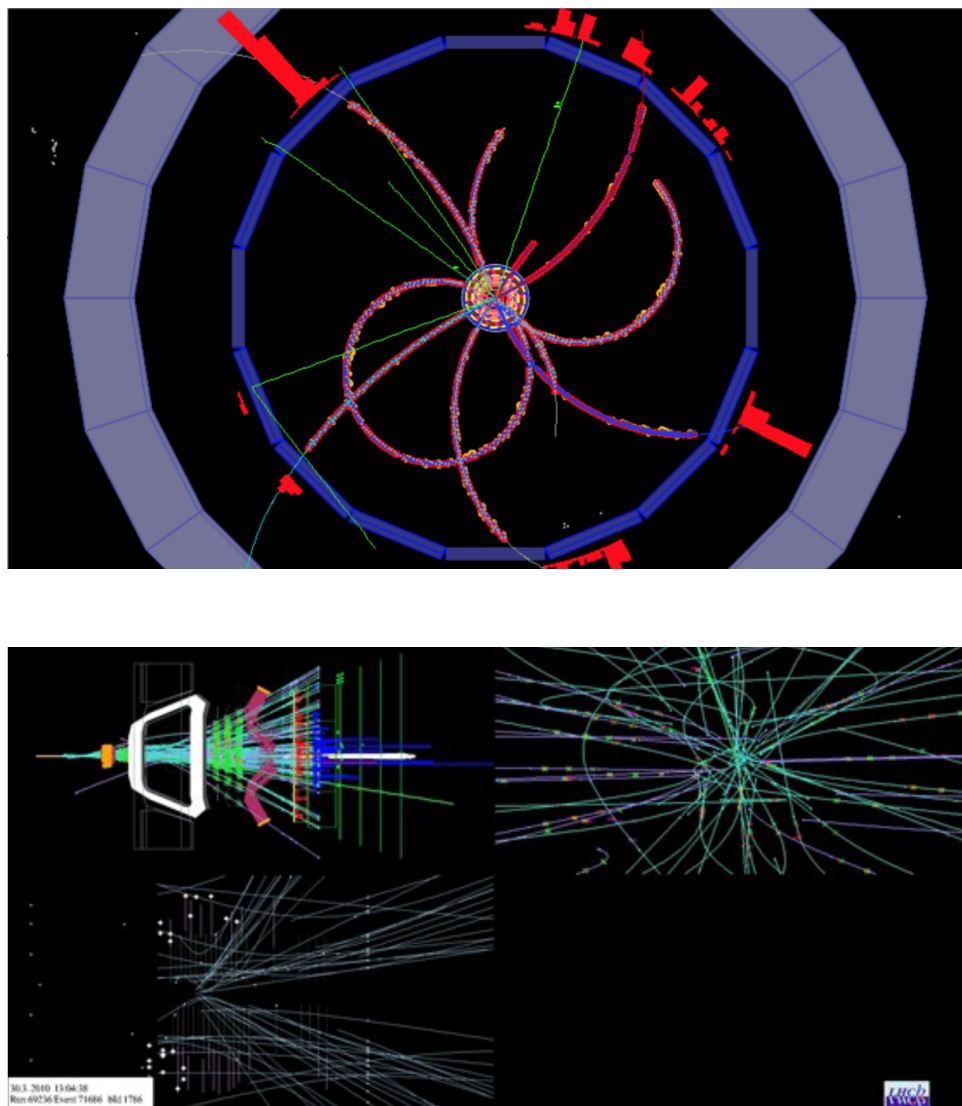
Figure 1.5: Typical event display for Belle II (top) and LHCb (bottom).

# Chapter 2

# The Belle II detector at the SuperKEKB collider

This chapter introduces the Belle II experiment, where I conducted my thesis work. It discusses the SuperKEKB collider and the Belle II detector, especially focusing on those subsystems relevant for charged-particle tracking and radiation monitoring, which are more closely related to my work.

## 2.1 The SuperKEKB collider at the KEK laboratory

SuperKEKB is a high-luminosity electron-positron ($e^+e^-$) energy-asymmetric collider [16], designed to produce nearly 1000 $B\overline{B}$ pairs ($B^0\overline{B^0}$ and $B^+B^-$ in approximately equal proportions) per second via decays of $\Upsilon(4S)$ mesons produced at threshold. Such colliders are called "$B$-factories", and were proposed in the 1990's for $\mathcal{CP}$-violation measurements in $B$ mesons. The main goal of $B$-factories is to produce low-background quantum-correlated $B\overline{B}$ pairs at high rates.

Intense beams of electrons and positrons are brought to collision at the energy corresponding to the $\Upsilon(4S)$ meson mass, which is just above the $B\overline{B}$ production kinematic threshold. Such finely tuned collision energy is key. The enhancement in production rate of $\Upsilon(4S)$ mesons, which decay in $B\overline{B}$ pairs 96% of the times with little available energy to produce additional particles, suppresses backgrounds, which are mainly due to competing non-resonant hadron production. In addition, beams of point-like particles allow knowing precisely the collision energy, which sets stringent constraints on the final-state kinematic properties, resulting in further background suppression. Since bottom mesons are produced in a strong-interaction decay, flavor is conserved, and the null net bottom content of the initial state implies production of a $B\overline{B}$ pair, which has null net bottom flavor; even though $B^0$ and $\overline{B^0}$ undergo flavor oscillations, their time-evolution is quantum-correlated in such a way that no $B^0B^0$ or $\overline{B^0}\overline{B^0}$ pairs are present at any time. In fact, angular-momentum conservation implies that the decay of a spin-1 meson in two spin-0 mesons yields final states with total angular momentum L=1. Because the simultaneous presence of two identical particles in an antisymmetric state would violate Bose statistics, the system evolves coherently as an oscillating $B^0\overline{B^0}$ particle-antiparticle pair until either one decays. This allows identification of the bottom (or antibottom) content of one meson at the time of decay of the other, if the latter decays in a final state accessible only by either bottom or antibottom states (flavor-specific decay). This feature is called "flavor tagging" and is fundamental because it allows measurements of flavor-dependent decay rates, as needed in

determinations of $\mathcal{CP}$-violating quantities. Not just $\Upsilon(4S)$ mesons are produced in 10 GeV $e^+e^-$ collisions; Figure 2.1 shows the hadron-production cross-section in $e^+$ $e^-$ collisions as a function of the final-state mass. The various peaks are excitations of the $\Upsilon$ meson and the nearly uniform baseline at $\approx 4\,\mathrm{nb}$ represents the so-called continuum ($e^+e^- \to q\bar{q}$) production, which exceeds $\Upsilon(4S)$ production in rate.
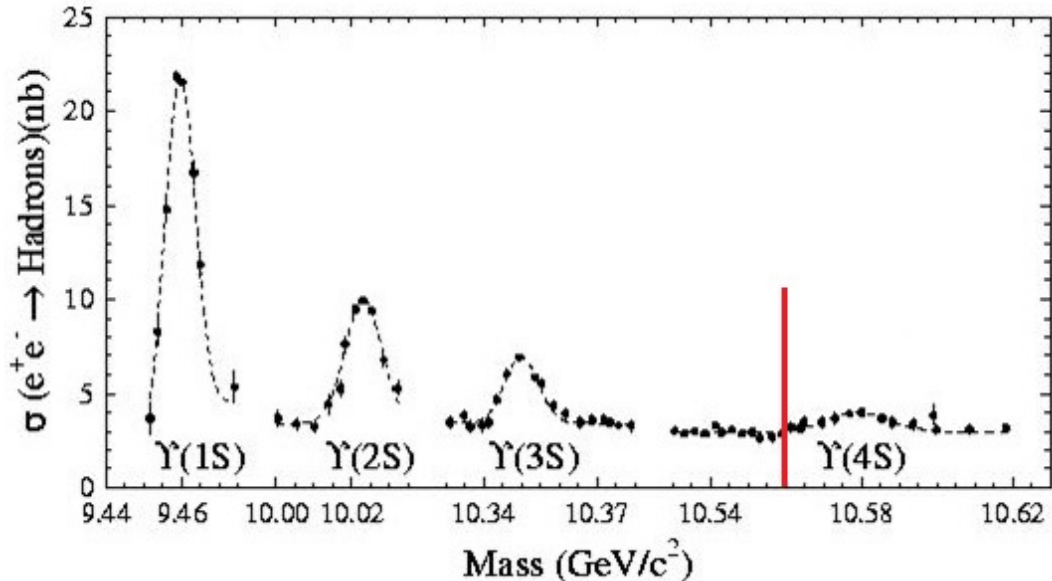


Figure 2.1: Hadron production cross section from $e^+$ $e^-$ collisions as a function of the final-state mass. $\Upsilon$ resonances are visible. The red vertical line indicates the $B\overline{B}$ production threshold.

Because the $\Upsilon(4S)$ mesons are produced at threshold, in an energy-symmetric collider they would be nearly at rest in the laboratory frame. Hence, the resulting $B$ mesons would too be produced with low momentum ($\approx 10\,\mathrm{MeV}/c$) in the laboratory, because of the $21\,\mathrm{MeV}/c^2$ difference between $\Upsilon(4S)$ and $B\overline{B}$ pair masses. With such low momenta they would travel approximately $1\,\mu$m before decaying. The $10\,\mu$m typical spatial resolution of vertex detectors would not be sufficient to separate $B$-decay vertices and study the decay time evolution for measurements involving mixing. Asymmetric beam energies are used to circumvent this limitation, because they boost the collision center-of-mass along the beam in the laboratory frame, thus achieving $B$-decay vertices separation. SuperKEKB (Fig. 2.3) implements a 7-4 GeV energy-asymmetric double-ring design, which achieves a vertex displacement of about $150\,\mu$m. SuperKEKB is designed to reach, by 2025, $50\,\mathrm{ab}^{-1}$ of integrated luminosity, corresponding $\approx 5.28 \times 10^{10}$ $B\overline{B}$ pairs, about 40 times the amount collected by its predecessor KEKB.

Electrons are produced via photoelectric effect by targeting a cold cathode with a pulsed laser, then accelerated to $7\,\mathrm{GeV}$ with a linear accelerator (Linac) and injected in the High-Energy Ring (HER). Positrons are produced by colliding electrons on tungsten; they are first injected in a damping ring to reduce their emittance (spread in position and momentum), then accelerated to $4\,\mathrm{GeV}$ with the Linac and injected in the Low-Energy Ring (LER). When sufficiently intense beams circulate in the LER and HER, they are brought to collision. The collision products fly from the interaction point (IP) trough the volume of the detector, where various final states (Table 2.1) can be detected.

To achieve high luminosities, a nano-beam, large crossing-angle collision scheme is implemented [17]. This is an innovative configuration based on keeping small horizontal and vertical emittance and large crossing angle, as shown in Figure 2.2. This is obtained

with a final-focus superconducting-quadrupole-magnet system (QCS), made of magnets, corrector coils, and compensation solenoids; a QCS magnet is installed at each longitudinal end of the interaction region. Conceptually the nano-beam scheme mimics a collision with many short micro-bunches, allowing great advantages in luminosity with respect to previous standard schemes. The reduction of the luminous volume size to about 5% with respect to the predecessor KEKB, combined with doubling of beam currents, is expected to yield a factor 40 gain in intensity.
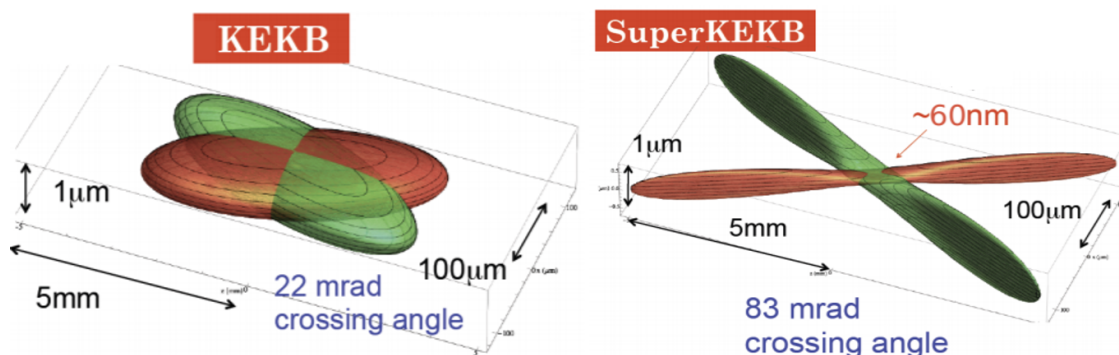


Figure 2.2: Two-dimensional sketch of the nano-beam mechanism implemented in SuperKEKB (right) compared with the previous KEKB collision scheme (left).
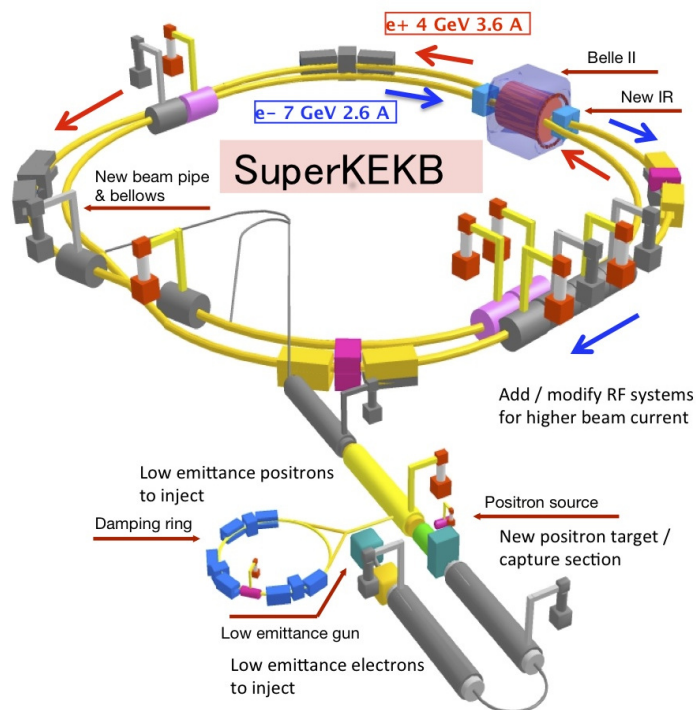


Figure 2.3: Scheme of the SuperKEKB collider.

### 2.1.1 Beam conditions in spring 2019

In March-July 2019, the first months of operations with a complete detector, beam parameters changed repeatedly to optimize the trade-off between luminosity increase and

| Final state | Cross section (nb) |
|:---:|:---:|
| $\Upsilon(4S)$ | 1.05 |
| $c\bar{c}(\gamma)$ | 1.30 |
| $s\bar{s}(\gamma)$ | 0.38 |
| $d\overline{d(\gamma)}$ | 0.40 |
| $u\bar{u}(\gamma)$ | 1.61 |
| $e^+e^-(\gamma)$ | 300 |
| $\mu^+\mu^-(\gamma)$ | 1.148 |
| $\tau^+\tau^-(\gamma)$ | 0.919 |
| $\nu\bar{\nu}(\gamma)$ | $0.25 \times 10^{-3}$ |
| $\gamma\gamma(\gamma)$ | 4.99 |

Table 2.1: Cross sections of the main final states produced in $e^+$ $e^-$ collision at the $\Upsilon(4S)$ center-of-mass energy [15].

beam-background radiation. Figure 2.4 shows a summary of the major changes that characterized SuperKEKB spring 2019 operations. Beam currents started from 100 mA in March and steadily increased up to 700 mA by the end of June. The number of bunches in both rings changed several times between 395, 789, and 1576, depending on the observed beam-background conditions. Physics data taking started with a "normal" injection configuration, i.e., new particles were injected in the circulating bunches to restore high luminosities approximately every two hours. When sufficient control was gained over background associated with injection, a "continuous" injection mode was implemented to increase luminosity: injection gates were kept open and bunches were refilled with small injections at 25 Hz. Luminosity grew from $0.1 \times 10^{34}\,\mathrm{cm^{-2}s^{-1}}$ to $1.2 \times 10^{35}\,\mathrm{cm^{-2}s^{-1}}$. Such frequent changes of beams parameters, even if aiming at improving data-taking conditions, represented a challenge for the detectors, whose working points had to continuously adapt to the frequently changing conditions. Careful operations of dedicated systems aimed at monitoring and protection, like the diamond-sensor system I have been working on, had been an essential asset in this phase.
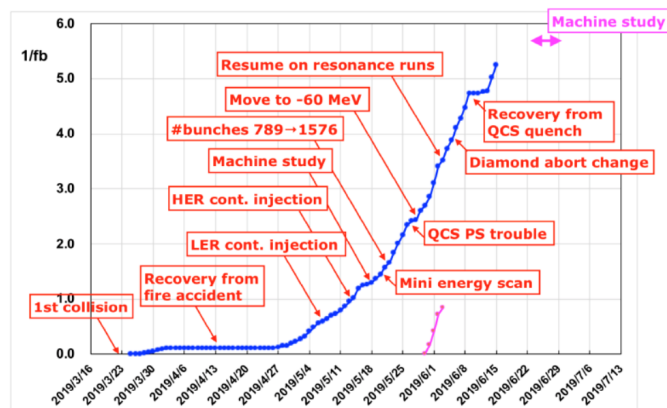


Figure 2.4: Plot summarizing the main events that characterized SuperKEKB operations in the 2019 spring run.

## 2.2 Overview of Belle II

The Belle II detector is a significant upgrade of its predecessor, Belle, and targets more ambitious physics goals. While it is located in the same experimental hall and has a similar design to its predecessor, most of its subdetectors are new or considerably upgraded. A more efficient charged hadron identification (PID) is implemented, for increased separation oh final-state charged hadrons, reducing backgrounds, and improving flavor-tagging; a better resolution in the reconstruction of the decay positions (vertices) of long lived particles is achieved, to enhance background suppression and sensitivity in measurements of decay-time dependent quantities; one important accelerator upgrade impacts the detector too: a smaller boost of the center of mass of the collision is employed, to improve acceptance for final states with neutrinos. These improvements are achieved through technologies designed to sustain the higher luminosity SuperKEKB delivers: detectors closer to the beam pipe are subjected to high occupancies and radiation damages, associated with higher beam-induced backgrounds; an increased pile-up noise affects the electromagnetic calorimeter, along with more neutron hits in the muon detectors.

The main subsystems are summarized in Table 2.2 and shown in Figure 2.5. They are detailed in next sections and can be broadly classified as follows:

- **Detectors for charged particle tracking**: silicon pixel and strip detectors close to the beam pipe and a wire drift chamber, all immersed in a $1.5\,\mathrm{T}$ magnetic field parallel to the beam axis, are used for reconstruction of charged-particle trajectories (tracks).

- **Detectors for particle identification**: particle identification is achieved through Cherenkov radiators, an electromagnetic calorimeter and scintillators for muon and long-lived neutral hadrons.

- **Data acquisition system**: a two-stage online trigger is designed to acquire interesting events at the high rates expected at design luminosities.

Figure 2.5: Top view of Belle II, the beam pipe at IP and final-focus magnets, all subdetectors are highlighted.

| Purpose | Name | Component | Configuration | Readout channels | $\theta$ coverage |
|---|---|---|---|---|---|
| Beam pipe | Beryllium | | Cylindrical, inner radius 10 mm, 10 $\mu m$ Au, 0.6 mm Be, 1 mm paraffin, 0.4 mm Be | | |
| Tracking | PXD | Silicon pixel (DEPFET) | Sensor size: 15×(L1 136, L2 170) mm², Pixel size: 50×(L1a 50, L1b 60, L2a 75, L2b 85) $\mu m^2$; two layers at radii: 14, 22 mm | 10M | [17°;150°] |
| | SVD | Silicon strip | Rectangular and trapezoidal, strip pitch: 50(p)/160(n) - 75(p)/240(n) $\mu m$, with one floating intermediate strip; four layers at radii: 38, 80, 115, 140 mm | 245k | [17°;150°] |
| | CDC | Drift chamber with He-$C_2H_6$ gas | 14336 wires in 56 layers, inner radius of 160mm outer radius of 1130 mm | 14k | [17°;150°] |
| Particle ID | TOP | RICH with quartz radiator | 16 segments in $\phi$ at $r \approx 120$ cm, 275 cm long, 2cm thick quartz bars with 4×4 channel MCP PMTs | 8k | [31°;128°] |
| | ARICH | RICH with aerogel radiator | 2×2 cm thick focusing radiators with different $n$, HAPD photodetectors | 78k | [14°;30°] |
| Calorimetry | ECL | CsI(Tl) | Barrel: $r = 125 - 162$cm, end-cap: $z = -102-+196$cm | 6624 (Barrel), 1152 (FWD), 960 (BWD) | [12.4°;31.4°], [32.2°;128.7°], [130.7°;155.1°], |
| Muon ID | KLM | barrel:RPCs and scintillator strips | 2 layers with scintillator strips and 12 layers with 2 RPCs | $\theta$ 16k, $\phi$ 16k | [40°;129°] |
| | KLM | end-cap: scintillator strips | 12 layers of (7-10)×40 mm² strips | 17k | [25°;40°], [129°;155°] |

Table 2.2: Summary of the Belle II components and specifications.

## 2.3 Tracking detectors

The innermost detectors are used for charged-particle vertexing. Strong track reconstruction is of great importance since flavor-physics final states are mostly composed of charged particles and analyses rely strongly on precise measurements of their momentum and the decay position of their long-lived parent particles. Precisely measured momenta and vertices allow separation of signal from backgrounds via narrower, and therefore more distinctive, invariant-mass signal peaks compared to smoothly distributed backgrounds, and higher mean-valued decay lengths. Moreover, information on the decay time is key for measurements of $\mathcal{CP}$-violating asymmetries involving mixing.

### 2.3.1 Silicon-pixel vertexing detector

The innermost detector is a pixel vertexing detector (PXD). Its goal is to sample the trajectories of final-state charged particles in the vicinity of the decay position (vertex) of their long lived ancestors, so that the decay point can be inferred by extrapolation inward.

PXD sensors are based on depleted field-effect transistor technology [18]. They are made of p-channel MOSFET integrated on a silicon substrate, which is fully depleted by applying an appropriate voltage. Incident particles generate electron-hole pairs in the depleted region, and thus induce a current passing through the MOSFET. Sensors are 75 $\mu$m thick, which allows on-pixel integration of most of the electronics.
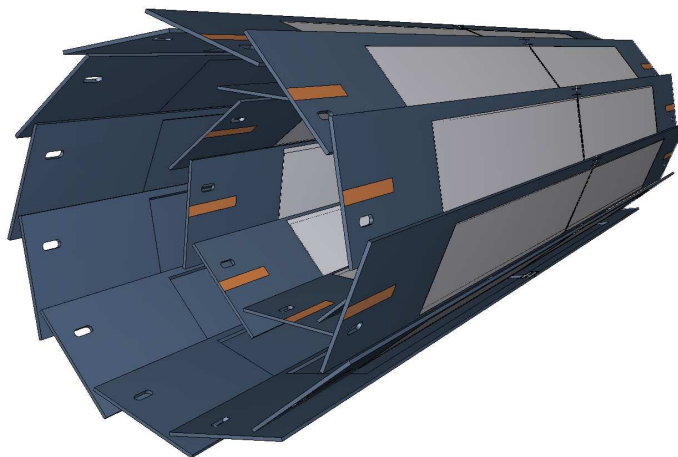


Figure 2.6: Scheme of the PXD detector.

The PXD has two layers at 14 mm and 22 mm radius, respectively, and a full length of 174 mm at the radius of the outer layer. It comprises around 8 million pixels, $50 \times (50-55)\mu\text{m}^2$ (inner layer) and $50 \times (70-85)\mu\text{m}^2$ (outer layer) each. The polar acceptance ranges from 17° to 150°. The design impact-parameter resolution is 12 $\mu$m, achieved by weighting the charge deposited in neighbouring pixels. To simplify pattern recognition, tracks are first reconstructed in the outer tracking volume, where lower occupancy aids track finding, and extrapolated to the PXD radius, to define regions of interest around their expected intersection points. If a firing pixel is found inside this region, it is kept in the pattern recognition algorithm, otherwise it is discarded. At the moment only one PXD layer is installed; the second layer will be added in the next years, if occupancy from higher luminosities will require it for disambiguation.

### 2.3.2 Silicon-microstrip vertexing detector

Around the PXD is SVD [19], a silicon detector aimed at reconstructing decay vertices and low-momentum charged-particle tracks at high resolution.

SVD uses a double-sided silicon strip technology. Each sensor is made of a silicon n-doped bulk with an highly p-doped implant on one side. An applied bias enhances the depletion region at the p-n junction, and removes intrinsic charge-carriers from the region. Traversing charged particles ionize the silicon, freeing electron-hole pairs that drift due to the electric field, inducing a signal in highly granular strip electrodes implanted at both ends of the depletion region. The fine segmentation of SVD sensors reduces latency, in order to deal with the high expected rates.
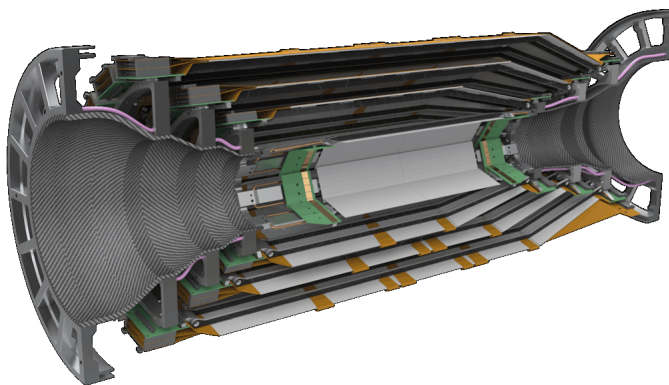


Figure 2.7: Exploded view of a SVD detector half.

SVD is structured into four concentric layers at radii of 39, 80, 104 and 135 mm, composed by, respectively, 7, 10, 12, and 16 independently-readout modules called ladders, arranged in a cylindrical geometry. As shown in Figure 2.7, SVD has a polar-asymmetric geometry that mirrors the asymmetry in particle density resulting from the center-of-mass boost. The polar acceptance ranges from 17° to 150°.

Sensors are 300 $\mu$m thick, and the separation between adjacent strips ($d_{pitch}$) ranges from 50 $\mu$m to 240 $\mu$m. Hence, the spatial resolution $d_{pitch}/\sqrt{12}$ varies with the polar angle. Since the charge associated with an incident particle is usually distributed among several strips, position resolution is improved by interpolation.

### 2.3.3 Tracking drift chamber

The CDC [20] is a drift chamber. It samples charged-particle trajectories at large radii, thus providing trigger signals for events containing charged particles, and it contributes to identification of charged-particle species by measuring their specific-ionization energy-loss ($dE/dx$).

When a charged particle traverses the CDC volume, it ionizes the gas, freeing electrons and positive ions from gas atoms. An applied electric field then moves these charges until they approach the sense wires, where high field gradients cause an abrupt acceleration with secondary ionizations that induce an electric signal. The particle trajectory is inferred from the time between the collision and the signal, whose time is digitized.

The CDC inner radius is 16 cm and outer radius is 113 cm. The chamber is composed of 14336 30-$\mu$m-diameter sense wires, divided in 56 layers, immersed in a gaseous mixture of 50% He and 50% $C_2H_6$, while 42240 126-$\mu$m-diameter aluminum wires shape the electric field. The azimuthal acceptance ranges from 17° to 180°.

The spatial resolution is about 100 $\mu$m and the $dE/dx$ resolution is 11.9% for an incident angle of 90°. Figure 2.8 shows a reconstructed cosmic ray track in the CDC.
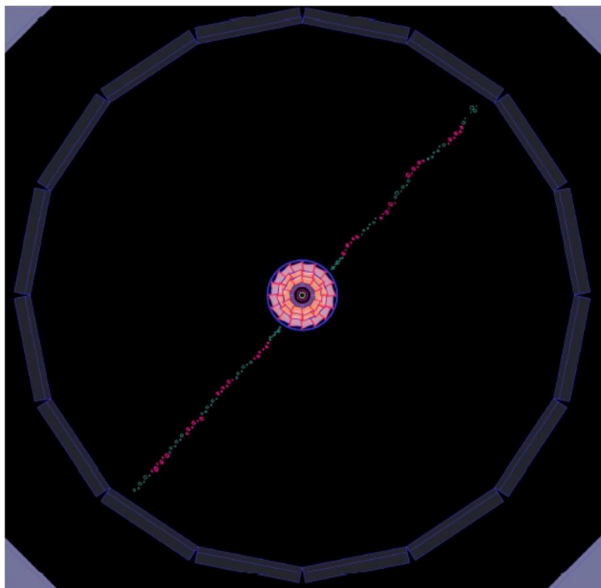


Figure 2.8: Reconstruction of a cosmic-ray track in the CDC.

## 2.4 Other detectors

Belle II features several other detectors, mainly used for particle identification. Because these are less relevant in my thesis work, I only offer an overview of them here.

The TOP detector [21] measures the time of propagation of the Cherenkov photons emitted from charged particles passing through its quartz bars and internally reflected within a radiator. It is made of 16 quartz bars mounted at 1.2 m from the IP. Each bar has three main components (Fig. 2.9): a long bar acts as Cherenkov radiator, where photons are generated and propagated; a focusing mirror is mounted at the forward end; and a prism mounted at the backward end collects photons and guides them to a photomultiplier. The polar coverage ranges from 31° to 128°. On average, photons originated from slower particles take more time to reach the PMT, because of the inverse proportionality between $\beta$ and $\cos\theta_C$. The time resolution is about 100 ps, allowing separation of pions from kaons at $0.4 - 4\,\mathrm{GeV}/c$ momenta with design kaon detection efficiency of 90% and pion misidentification rate of 5%.

The ARICH detector [22] identifies charged particles by measuring the Cherenkov ring produced when passing through a radiator. It consists of 420 modules for photon detection in seven layers extending from 0.56 to 1.14 m radius, and 248 aerogel tiles installed on the detector endcaps. The aerogel radiator produces Cherenkov photons when traversed by charged particles in a certain momentum range. Next to the radiator is an expansion volume where photons are propagated, to form rings on position-sensitive photodiodes. Photocathodes are then used to convert photons into photoelectrons and generate electric signals. Two adjacent radiators with different refraction indexes are used to generate enough photons for achieving sufficient resolution, as shown in Figure 2.10. The ARICH separates pions from kaons across all their momentum spectrum and discriminates also pions, electrons, and muons below 1 GeV/$c$ with $4\sigma$ separation or more.
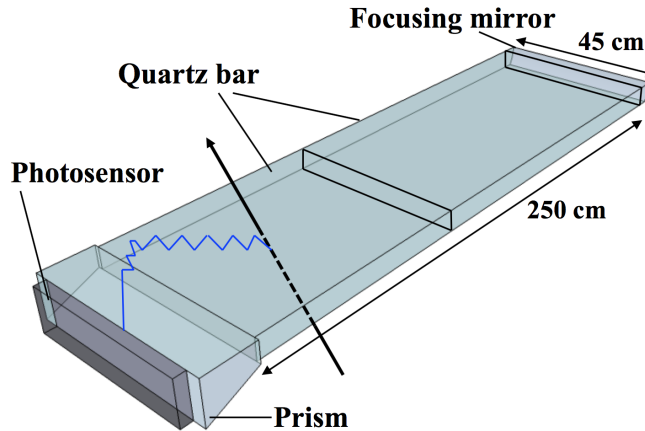
Figure 2.9: Scheme of a TOP bar. A charged particle crossing the radiator and emitting Cherenkov photons, which are collected at the PMT, is also represented.
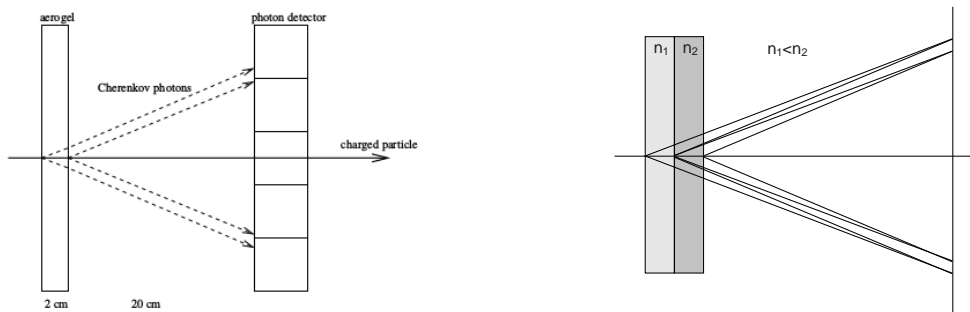


Figure 2.10: Scheme of the ARICH detector.

The ECL [23] measures the energy of photons, pions, and electrons. The active material is CsI(Tl), which has short radiation length, high light output, and convenient mechanical properties. Endcaps are made of CsI crystals, characterized by shorter scintillation decay time, to reduce beam-background photons. Particles impinging on the calorimeter release energy through scintillation processes, energy that is partially converted into photons collected by photodiodes. The ECL has a 3-m-long barrel geometry with inner radius of 1.25 m and annular endcaps at $z = 1.96$ m (forward) and $z = -1.02$ m (backward) from the interaction point. The polar coverage ranges from 12.4° to 155.1°. The energy resolution ranges from $\sigma_E/E = 4\%$ at 100 MeV to 1.6% at 8 GeV. The expected resolution on the reconstructed $\pi^0$ mass is of $4.5\,\mathrm{MeV}/c^2$. The ECL uses Bhabha scattering to measure luminosity. Because the Bhabha cross section is predicted with high accuracy in QED, a precise inference of luminosity is achieved from the measured rate of Bhabha events in a volume of known acceptance.

The KLM [24] detects muons and neutral particles that do not get absorbed in the inner detectors, such as $K_L^0$. It is made of alternating 4.7-cm-thick iron plates and active detector elements. Iron elements act also as magnetic flux returns for the tracking solenoid. In the inner layers, the active material is scintillator, while in the outer layers are glass-electrode resistive-plates chambers, with a gas mixture filling the space between electrodes. When particles cross the KLM, they produce charges that are collected by applying an appropriate voltage. The barrel section of the detector covers 45° to 125° in polar angle. The endcaps cover 20° to 45° and 125° to 155°. Design reconstruction efficiency exceeds 80% for muons with momentum greater than 1 GeV/$c$ and $K_L^0$ with momentum greater than 3 GeV/$c$.

## 2.5 Online event selection

Various processes may occur in 10 GeV $e^+e^-$ collisions (Tab. 2.1). Since the events of physical interest are a fraction of the total cross section, the goal of the online event selection (trigger) is to identify them in real time while rejecting background events, to reduce the data-writing rate. The trigger must be efficient for recording hadronic event from $\Upsilon(4S) \to B\overline{B}$ and for the continuum to a manageable level, up to a maximum accept rate of about $30\,\text{kHz}$, due to data acquisition restrictions. $B\overline{B}$ events have distinctive high-track multiplicity, and therefore are relatively straightforward to select; events containing $\tau$ decays are harder, since they have fewer tracks in the final state and can therefore be misclassified as backgrounds. The trigger must also reject processes that are not interesting for Belle II physics, like $e^+e^- \to e^+e^-$ or $e^+e^- \to \mu^+\mu^-$.

The trigger is composed by a hardware trigger called Level1 (L1) [25] followed by a software high level trigger (HLT) [25]. The L1 decision is mainly based on informations from CDC and ECL, but also TOP and KLM informations can be used. The L1 decision feeds the global decision logic [25], that sends out the final trigger based on the informations it receives from the detector. HLT is based on a more complete software reconstruction of the event similar to the offline reconstruction, using charged particles from the CDC and energy deposits in the ECL. It selects events on the base of tracking multiplicity, vertex position, and total energy deposition. HLT is expected to achieve a 30% event rate reduction without efficiency loss for signal processes.

## 2.6 Status

An overview of the SuperKEKB and Belle II operations is in Table 2.3.

| Phase | Period | Main goals | Detectors |
|-------|--------|------------|-----------|
| Phase 1 | February-July 2016 | Accelerator tuning and background tests w/o final focusing | w/o Belle II, other detectors for background studies |
| Phase 2 | March-July 2018 | Verification of nano-beam, background study and physics data | w/ partial Belle II (partial PXD and SVD) |
| Phase 3 | From March 2019 | Complete physics program | w/ Belle II |

Table 2.3: Summary of the three commissioning phases of SuperKEKB and Belle II.

The 2018 pilot-run, with a partially incomplete detector, conventionally dubbed Phase 2, has concluded. It had the goal of validating the nano-beam scheme while learning how to operate Belle II detector with controlled backgrounds.

The goal of 2019 operations, called Phase 3, was to take physics data with the full detector, steadily increasing the instantaneous luminosity. The first part of Phase 3, including the three months I spent at KEK, was aimed at starting operations and to keep improving detector and accelerator conditions, in order to increment the luminosity whenever possible without jeopardizing the detector.

By summer 2019 luminosity reached $1.2 \times 10^{34}\,\mathrm{cm}^{-2}\mathrm{s}^{-1}$. The main limitations encountered to further increase luminosity from the machine side were the incomplete control of the injection backgrounds and some issues in QCS control, leading to uncontrolled beam accidents that damaged the SuperKEKB collimators (metallic surfaces mounted inside the beam pipe). From the detector side, the main issues where an unexpected increase of leakage currents in the CDC and of photon multiplicity in the TOP, along with some difficulties of the trigger to sustain high rates of events. Improvement are currently under development both on accelerator and detectors.

# Chapter 3

# Diamond detector commissioning for physics

In this chapter the description of my original contribution begins. I introduce the main sources of SuperKEKB beam backgrounds and discuss features and capabilities of the diamond sensors used as radiation monitors in Belle II. I then discuss my contribution to the diamond-system operations at the inception of the physics run, outlining the tasks associated with standard operations and discussing in more detail the specific improvements I introduced.

## 3.1 Diamond system overview

While beams circulate in the accelerators, various processes can occur that perturb the motion of the particles. Their interactions with residual gas and the vacuum pipe walls generate background particles and radiation that cross the active parts of the detector and need to be monitored and mitigated, to protect the detector and ensure smooth, efficient data taking. Such "beam-backgrounds" become more frequent and severe as the collision luminosity increases. The diamond system is devoted to measure the absorbed dose by the inner detector and abort the beams if background radiation becomes too intense.

### 3.1.1 Beam backgrounds

The most important effects that generate relevant beam background in SuperKEKB [26] are as follows.

- **Beam-gas scattering:** this is the interaction of the accelerated particles with residual gas molecules in the evacuated beam pipe. Coulomb scattering changes the particle trajectory and bremsstrahlung degrades particle energy via photon emission. The beam-gas scattering rate is roughly proportional to beam current ($I$) and to the pressure ($P$) inside the beam pipe,

$$r_{BG} \propto p_0 I + p_1 I^2,$$

where the two components in the right-hand side of the equation refer to the pressure without beams ($p_0$) and to a dynamical component that depends on the beam current ($p_1$). This second component is related to gas molecules previously absorbed in the walls of the beam enclosure that are re-emitted following electromagnetic "heating" of the walls due to circulating currents. Techniques to mitigate such phenomenon,

thus improving vacuum conditions, include *vacuum scrubbing*, i.e., circulating beams without collisions, and *baking*, i.e., heating sections of the beam pipe. In these processes, thermal emission of gas particles from the beam pipe walls is stimulated, and freed particles are then extracted using vacuum pumps. In addition, beam-gas background is reduced by reducing the beam-size and by moving collimators closer to the beams, to intercept and eliminate the beam tails.

- **Touschek scattering:** this is the electromagnetic scattering between particles of the same bunch. It is due to the betatron and synchrotron oscillations particles undergo during their motion, resulting in a momentum and energy spread. As a result of the scattering, some of the particles may deviate out of the beam orbit, resulting in their loss. Lost particles can hit the beam pipe and produce electromagnetic showers: if these losses happen near the IP, they can induce detector signals not related to electron-positron collisions. The Touschek scattering rate is

$$r_T \propto \frac{n_b I_b^2}{\sigma_x \sigma_y \sigma_z E^3},$$

  where $n_b$ is the number of bunches in the beam pipe, $I_b$ is the current of the single bunch, $\sigma_x$, $\sigma_y$, and $\sigma_z$ are, respectively, horizontal, vertical, and longitudinal bunch sizes, and $E$ is the particle energy. To reduce the flux of off-trajectory particles due to Touschek effect, collimators are used.

- **Synchrotron radiation:** these are photons emitted by accelerated charged particles. The emitted power is

$$W_S \propto \frac{E^2 B^2}{m^4 \rho^2},$$

  where $E$ is the beam energy, $B$ the magnetic field strength, $m$ the particle mass, and $\rho$ the curvature radius. Because of the proportionality to the squared beam energy, HER is the dominant source of synchrotron radiation in SuperKEKB. The energy spectrum ranges from few keV to tens of keV. The beam pipe around the IP is shaped such that photons emitted in this region are unlikely to directly hit the detector. In addition the inner surface is coated with gold to absorb the remaining ones, but a small fraction of such photons occasionally illuminates the detector.

- **Radiative Bhabha scattering:** this is electron-positron scattering that produces an additional photon in the final state, $e^+ e^- \to e^+ e^- \gamma$. Electron and positron lose momentum following photon emission, therefore they can hit the beam pipe walls and produce electromagnetic showers. Radiative Bhabha photons can also hit the SuperKEKB magnets producing low-energy gamma-rays or neutrons. Gamma-rays contribute to the background of the CDC and of the barrel PID system, while neutrons are the principal source of KLM background.

- **Injection background:** this is the background associated with new injections of particles into already circulating bunches, which happen at 25 Hz to keep the luminosity high. Injected particles have larger oscillations around the ideal bunch orbit with respect to stored particles, these oscillations are damped by synchrotron radiation and bunch-by-bunch feedback the system. This causes higher particle losses during injection and a generally higher background rate in Belle II in the first few milliseconds after injections.

The prevalences and proportions of these sources depend on the configuration of the SuperKEKB beam optics and many other subtle details that are difficult to reproduce precisely in simulation. Hence, they typically require trial and error on data to be understood.

### 3.1.2 Radiation damage

The beam backgrounds can damage the inner layers of the silicon detector and degrade its performances as the integrated dose increases. Preliminary estimates of the projected lifetime of Belle II at the design integrated luminosity $(50\,\mathrm{ab}^{-1})$ are of a total PXD integrated dose ranging from 15 to 18 Mrad. Estimates for SVD [27], which is less exposed to IP background, are of 4.5 Mrad approximately. Here and in the following, I adopt the practical unit $1\,\mathrm{rad} = 10^{-2}\,\mathrm{Gy}$.

The nature and severity of damage in silicon detectors depends on the energy and on the type of the radiation. The interaction may be with the electrons of the silicon crystal or with the silicon nuclei in the lattice. While the interaction with electrons leads to transitory effect, interactions with lattice atoms lead to permanent damage to the sensors. Displacement of the nuclei results in the appearance of atoms between regular lattice sites (interstitials) and empty lattice sites (vacancies). While these defects are temporary, they can combine with other defects to form stable defects that could change the electrical properties of the sensor. Such defects can act as recombination-generation centers, by capturing and emitting electrons and holes, and trapping centers, since this re-emission may happen in a longer timescale. If defects are charged, they affect spatial charge-density in the depletion-region. Radiation may also damage the dielectric layers in the silicon devices, at the interface between them and silicon. The main effect is charge build-up in the oxide and a higher interface trap density.

These lattice defects based on silicon devices induce various changes in the performances and operational parameters of the detector.

- **Reverse-bias current:** electrons and holes released by defects can generate reverse bias-currents in the depletion region. A linear relation exists between the leakage current increase and the impinging particle fluence (number of particles that intersect a unit area of the detector), since the defect-generation rate is proportional to the latter. If reverse-bias currents increase, the detector noise grows, and tracking performances are deteriorated.

- **Operating voltage:** since defects change the spatial-charge density in the depletion region, the bias voltage necessary to deplete the bulk increases. Defects interact with dopant atoms changing their charge, preventing them to act as donor and acting as active acceptors themselves. Therefore effective doping of the detector decreases with the impinging particle fluence until reaching an intrinsic-like condition. Further increasing generates a type inversion of the silicon substrate.

- **Trapping of signal charge:** trapping probability of signal charges is proportional to trap concentration, which increases with radiation-induced defects. Trapped charges are released after a certain time, and they contribute to the signal only if this happens during charge collection. This reduces the ratio between signal and noise, like reverse-bias currents do, because signal is reduced.

Besides these slowly-building defects, rapid beam-background energy releases induce damage the detector too. During intense spike-like irradiation, a large amount of charge carriers is created. This causes silicon to temporarily behave like an electric conductor,

making the biasing voltage to drop; this high-voltage difference can cause the dielectric to breakdown. Moreover, radiation affects also the readout electronics installed on the detector, inducing malfunctions and degraded performances.

### 3.1.3 Synthetic diamond as radiation sensor

Because of the fundamental role the vertex detector has in the Belle II experiment and the important efforts and costs associated with building it, a reliable protection system is key to keep it safe from beam-background radiation and ensure its optimal performance for the expected lifetime. Primary requirements for radiation-monitor detectors are

1. to rapidly measure sudden intense radiation bursts so as to allow immediate countermeasures;

2. to reliably measure integrated radiation dose for long-term studies of detector degradation;

3. to be radiation resistant;

4. to contribute low additional material in the detector volume, in order not to interfere excessively with the particle-reconstruction performance.

Various radiation monitoring technologies have been used in high-energy physics experiments. Gas ionization chambers are the most common instrument, but they require significant space which is hardly available in the vicinity of typical collider interaction regions. Indeed silicon PiN diodes, which are much smaller, were usually adopted in previous $B$-factory experiments [28–30]. However, this technology suffers from a major drawback: the reverse-bias current, which measures the instantaneous dose-rate, depends strongly on the temperature. The leakage current grows as the integrated dose increases. Therefore PiN diodes need to be frequently re-calibrated, which introduces a significant operation overhead and important systematic uncertainties in the recorded doses.

Because of superior performances with respect to the other radiation monitors, system based on high-purity diamond crystals have been recently implemented in several high-energy physics experiments. Table 3.1 summarizes and compares the main features of synthetic diamond compared with silicon. High-purity diamonds can be considered as "wide-gap intrinsic semiconductors": the high intrinsic forbidden energy gap and the extreme thermal conductivity results in radiation resistance and little temperature dependence, making them suited for radiation monitoring in high-radiation environments. The wide gap assures low leakage currents, while temperature independence allows to install diamond sensors also in areas where implementing powerful cooling is challenging. The high charge mobility allows for fast signals. The drawbacks are that costs per unit area are still high and that the technology is not yet as mature as that of silicon semiconductors, which implies significant R&D efforts before any large-scale deployment.

The charged-particle detection mechanism in diamond sensors is summarized in Fig. 3.1. An incident charged particle releases energy in the diamond bulk by ionization, promoting electrons from the valence band to the conduction band. This mechanism creates pairs of opposite charge carriers, each consisting in an electron in the conduction band and a vacancy in the valence band [31]. Electrons and holes drift due to an externally applied bias voltage $V_{\text{bias}}$ of a few hundreds Volts and are collected on the metallic ends of the sensors. The time-dependent component of the current in the circuit, generated by the impinging particle, is decoupled and measured by an external readout system.

| Property | Diamond | Silicon |
|---|---|---|
| Atomic number $Z$ | 6 | 12 |
| Number of atoms $N$ [$10^{22}$cm$^{-3}$] | 17.7 | 5.0 |
| Mass density $\rho$ [$g$ cm$^{-3}$] | 3.53 | 2.33 |
| Band gap $E_g$ [eV] | 5.47 | 1.12 |
| Resistivity $\rho_c$ [$\Omega$ cm] | $> 10^{12}$ | $2.3{\times}10^5$ |
| Electron mobility $\mu_e$ [cm$^2$V$^{-1}$s$^{-1}$] | 1800 | 1350 |
| Hole mobility $\mu_h$ [cm$^2$V$^{-1}$s$^{-1}$] | 1200 | 480 |
| Electron saturation velocity $v_e^s$ [$10^6$cm s$^{-1}$] | 26 | 10 |
| Hole saturation velocity $v_h^s$ [$10^6$cm s$^{-1}$] | 16 | 7 |
| Thermal conductivity $k$ [W cm$^{-1}$K$^{-1}$] | 21.9 | 1.5 |
| Energy to create e-h pair $E_{eh}$ [eV] | 13 | 3.6 |
| Displacement energy $E_d$ [eV/atom] | 42 | 15 |

Table 3.1: Comparison between diamond and silicon main properties at T = 300 K.
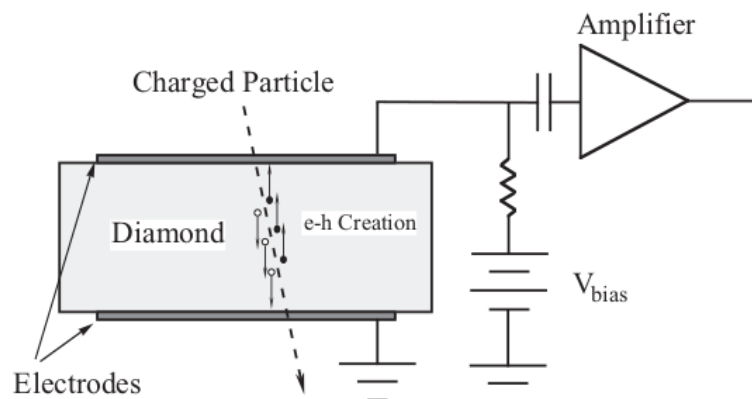


Figure 3.1: Schematic layout of a diamond sensor.

Diamond sensors detect neutral particles too. Photon detection depends on the incident photon energy. Photons with $E_\gamma < 1$ MeV free a shell electron via the photoelectric effect; photons with $0.1 < E_\gamma < 10$ MeV transfer their energy to electrons via Compton scattering; high energy $\gamma$ rays undergo $e^+e^-$ pair production after interacting wit nuclei [32]. The probability for these processes are small, because of the reduced amount of material present in the diamond crystal. Photons are more likely detected if they produce electromagnetic shower in the materials around the sensor, generating $e^-$ and $e^+$.

### 3.1.4 The Belle II diamond detectors
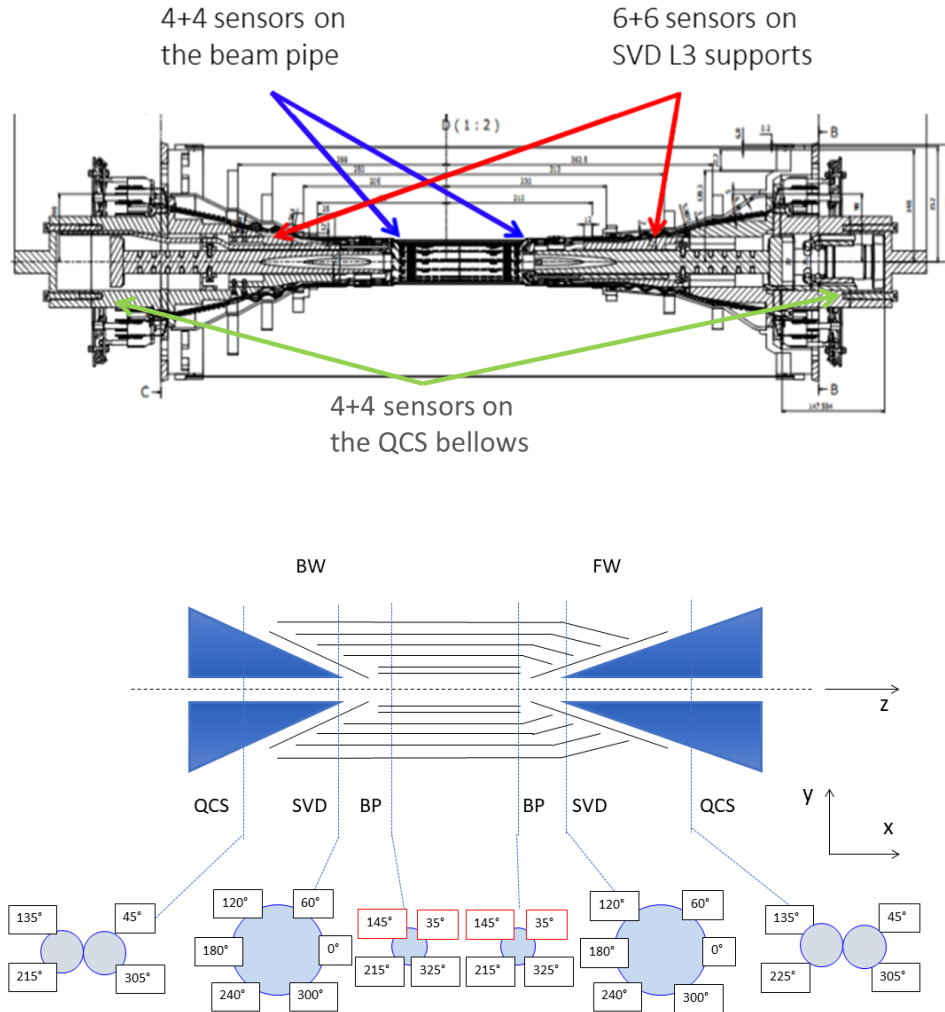


Figure 3.2: Radiation-monitor diamond sensors in the Belle II Phase 3 setup. Eight sensors are installed on the beam pipe, twelve on the SVD support, and eight on the QCS magnets bellows. Azimuthal position and labelling of each diamond is shown. Only the four diamonds indicated with red boxes in the bottom panel are used to deliver the beam-abort signal, the others monitor radiation.

The Belle II radiation monitoring system consists of 28 artificial single-crystal $1 \times 1$ cm$^2$ diamond sensors, installed around the interaction region as shown in Fig. 3.2 and detailed in Sec. 3.1.5. Their properties and labels are summarized in Table 3.2. The system has multiple goals:

- **Beam abort triggering:** if the dose rate in some sensors exceeds a predetermined threshold, the diamond system sends SuperKEKB a signal requiring to abort beams. The comparison is performed at 100 kHz, to match the beam-revolution period ($\approx 10\,\mu$s). When the threshold is exceeded, the abort-request signal is sent to the SuperKEKB control room in less than 1 μs.

  The parameters to define the abort logic are the threshold value, the integration time-window, and the multiplicity of over-threshold sensors. Two thresholds are set, *fast* and *slow*. The fast threshold is set on the dose integrated in a moving time window of 1 ms and is targeted at protecting the detector from sudden, large beam-background

spikes. The slow threshold is set on the dose integrated in 1 s and aims at limiting the radiation dose over longer time ranges. Thresholds and integration windows are configurable. Four out of twenty-eight diamonds were used for beam aborting during spring 2019 operations.

- **Radiation monitoring:** radiation doses measured by the diamond sensors are digitized and recorded at 10 Hz, to offer online and offline monitoring of the instantaneous dose rates. This information is also used to estimate the integrated dose in the vertex detector, and to optimize the accelerator operations: indications on beam backgrounds from diamond data are used by SuperKEKB operators during beam-optic tuning or collimator setting. Twenty out of twenty-eight diamonds were used for radiation monitoring during spring 2019 operations.

- **Injection inhibiting:** the inhibition of beam injection is a functionality not originally envisaged. It was introduced during my stay in Japan, after observing a correlation between the dose-rate measured in diamonds and the occupancy of the innermost layer of the SVD. A threshold was set on the combination of the dose rate of two of the innermost diamonds installed in longitudinally symmetric positions (BP_FW_325 and BP_BW_325, see Fig. 3.2), and beam injections are inhibited as long as this value is over threshold. The success of this feature prompted the implementation of a further injection inhibit mechanism by SuperKEKB, using two of the diamonds installed in longitudinally symmetric positions on the quadrupole squeezers (QCS_FW_135 and QCS_BW_135, see Fig. 3.2).

### 3.1.5 Setup

The radiation monitor setup in Phase 3 comprises 28 diamond detectors installed as shown in Fig. 3.2: eight on the beam pipe, twelve on the SVD structure, eight on the QCS bellows. Half are installed in the forward polar (FW) region, the others symmetrically in the backward (BW) region.

Diamonds are biased and read out by "diamond control units" (DCU), in group of four sensors. Since one DCU was still under construction at the time of this work, four diamonds from the SVD backward cone were not included in spring 2019.

| DCU number | Diamonds | Purpose |
|---|---|---|
| DCU # 1 | BP_{FW, BW}_{45, 135} | Beam-abort delivery |
| DCU # 2 | SVD_{FW, BW}_{0, 180} | Background monitoring |
| DCU # 3 | BP_{FW, BW}_{225, 315} | Background monitoring |
| DCU # 4 | SVD_{FW, BW}_{60, 120, 240, 300} | Background monitoring |
| DCU # 5 | QCS_{FW, BW}_{45, 135} | Background monitoring |
| DCU # 6 | QCS_{FW, BW}_{215,325} | Background monitoring |

Table 3.2: List of DCUs at the beginning of Phase 3 operations with corresponding diamonds and purpose.

The digital core is a board hosting a field-programmable gate-array (FPGA), that receives commands via an Ethernet interface, drives 4 high-voltage (HV) modules independently through a digital-to-analog converter (DAC), and accepts input data from an analog module including amplifiers and analog-to-digital converters (ADC). The diamond

currents are individually amplified by trans-impedance amplifiers, digitized by ADCs, and processed by FPGAs in the DCUs (Fig. 3.3).
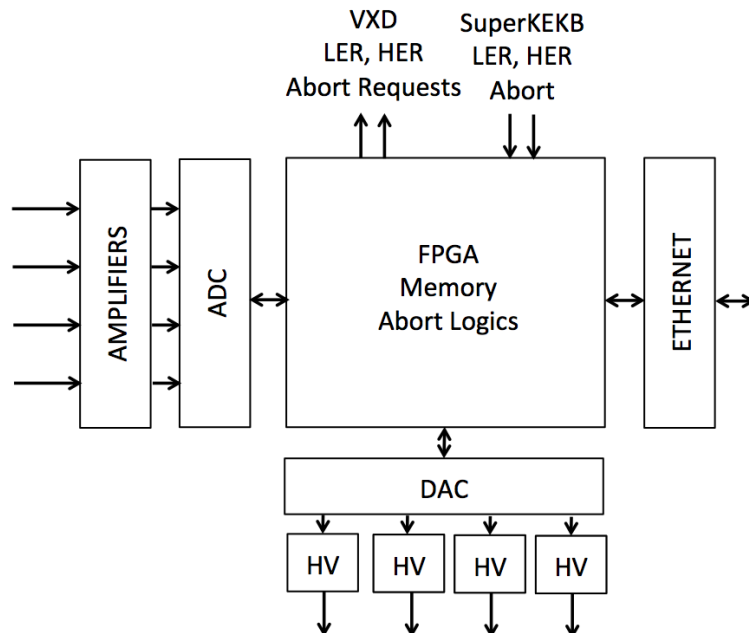


Figure 3.3: Block diagram representing the main DCU functional components.

In the amplifier section, three independent current ranges can be set (Tab. 3.3): lower current ranges offer higher sensitivity, allowing to measure smaller dose rates, but suffer from saturation at large currents. Increasing the current range enables measurements of large background spikes, which would otherwise saturate the analog front end, but degrades sensitivity to low doses.

| Current range | Dose-rate range | Current sensitivity (10 Hz) | Current sensitivity (100 kHz) | Dose-rate sensitivity (10 Hz) | Dose-rate sensitivity (100 kHz) |
|---|---|---|---|---|---|
| 0 - 36 nA | 540 mrad/s | 0.54 pA | 54 pA | 8 $\mu$rad/s | 1 mrad/s |
| 0 - 9 $\mu$A | 135 rad/s | 135 pA | 13.5 nA | 2.0 mrad/s | 0.13 rad/s |
| 0 - 4.5 mA | 45 krad/s | 67.5 nA | 6.75 $\mu$A | 1.0 rad/s | 4 rad/s |

Table 3.3: Summary of the ranges and sensitivities for various DCU configurations and data frequencies.

### 3.1.6 Beam-abort logic

Figure 3.4 shows a simplified scheme of the logic implemented in the FPGA. The amplified diamond currents, digitized and oversampled at 50 MHz by ADCs, are summed ($\Sigma_{N_1}$) in blocks of 500 samplings to achieve the 100 kHz-sampling data stream that is used in the abort logic. Two different moving sums ($\Sigma_{T_1}$, $\Sigma_{T_2}$) run on this data stream, adding every 10 $\mu$s the latest value and discarding the oldest one: these sums achieve the aforementioned integration over time windows. Results of these sums are compared with thresholds. Both

the amount of data summed (i.e., the length of the time window) and the threshold values are configurable. In addition, 100 kHz data are independently summed again in blocks of $10^4$ samplings, resulting in a 10 Hz data stream that is archived and used for online and offline analysis.

If the result of a moving sum exceeds the corresponding programmed threshold, a logical abort signal is generated; in total, eight signals are available per DCU, four for fast and four for slow threshold aborts. Individual masks can be applied to exclude noisy channels. The selected signals are combined in a "majority" logic in each DCU, to generate abort requests, separately for LER and HER, requiring a minimum number of signals above threshold. If a programmed "abort request" condition is met, the reaction time is 10 $\mu$s for all moving sums, independently of their integration time. The corresponding programmable logic is sketched in the block diagram shown in Fig. 3.4. The abort request signals are propagated to the output connectors only if the "abort enable" condition is set by the corresponding command to the FPGA; the purpose of such condition is to prevent a DCU from issuing a beam abort if needed. According to SuperKEKB specifications, these signals are ON (high logic-level) in normal conditions and go OFF (low logic-level) when an abort request is present. The output level remains OFF after an abort, until reset by a software command to the FPGA, to confirm that SuperKEKB is ready again for injection.

Hence, DCUs abort outputs are logic levels that are always ON except when an abort is issued. This choice for the logic ensures that an abort is issued also if the power supplies or communications with accelerator are lost, guaranteeing that the beams are prevented from circulating and the detector is safe in whatever condition occurs when no full control of the system is available. All the DCUs are daisy chained, each sending its output to the next. The final DCU sends the output to the SuperKEKB control room, where it is combined with the signals coming from all other independent radiation monitors installed on the rings, which too can issue beam-abort requests. The logic "OR" of the abort requests is sent to the beam-abort mechanism, which works with the same complementary logic (ON for normal conditions).

Beams are aborted by a magnet, named *kicker*, that deviates the beams into an absorption area in a specific position along the ring, opposite to the interaction region. Only one kicker is currently installed on each of the two SuperKEKB rings. Kickers are activated only in correspondence of the transit of a dedicated spatial gap (abort gap) between sequences of circulating bunches. This is essential not to perturb the beam orbit and risk a catastrophic dump on the detector when an abort is issued. To start a beam-abort, the system waits for the transit of the abort gap; all circulating bunches must pass trough the kicker to complete it. Completing the aborting procedure takes therefore a longer time than the beam revolution period. This setup causes a sizeable delay between the instant an abort request is issued and completion. This is discussed later in this chapter.

Whenever SuperKEKB initiates a beam abort, a signal is also sent back from SuperKEKB to the DCUs: when this signal is received by the DCUs, they dump the last second of their internal memories, sampled at 100 kHz, on files that can be analysed for post-mortem studies.

## 3.2   Diamond system operations

I have been the on-site expert in charge of diamond-system operations for three months during the beginning of Phase 3. This implied various duties at different levels: I had to perform some normal daily operations, I was in charge to intervene in case of exceptional issues to fix malfunctions and recover the system, and I analyzed offline diamond data for
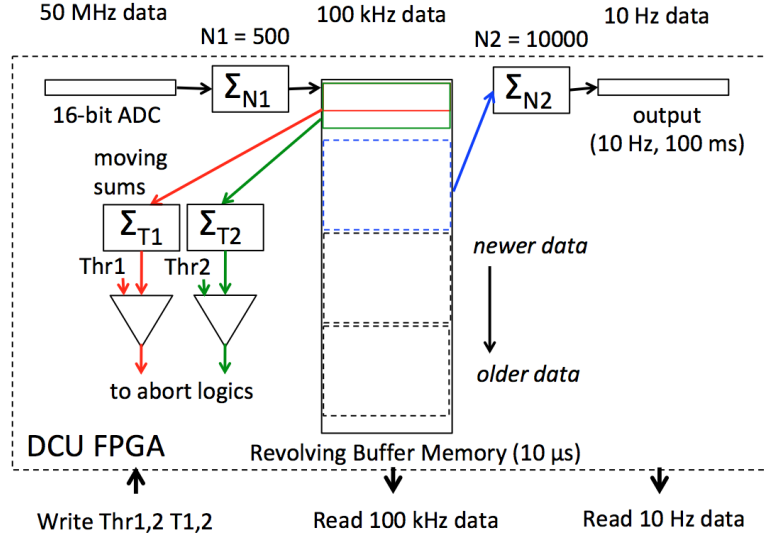
Figure 3.4: Block diagram representing the DCU data stream.

longer-term improvements.

### 3.2.1 Normal operations

Normal operations included daily monitoring of the system, continuous coordination with all the other subdetectors, reporting on the operation status in daily and weekly meetings, and resolution of minor issues. Since the beginning of Belle II physics run in March 2019, machine parameters have been changing frequently to steadily improve the luminosity (see Fig. 2.4). Therefore, it was essential to keep the system consistently under control to ensure safe, smooth, and efficient Belle II data taking under such fluid conditions.

In a typical day of standard, uneventful operations, I checked roughly every hour the live plots of various quantities to gain a quick glance of the situation: e.g., when beam current increased I would check the diamond behavior by looking at a live plot of currents and diamond dose-rates; an example screenshot of such plot is shown in Fig. 3.5. I also occasionally analyzed the correlations of archived data with other relevant variables, like beam currents, collimator openings, or SVD-layer occupancies in search for causal indications of effects. I used archived data also to monitor the 10 Hz dose rate and the above beam-related observables in real-time and in specifically chosen time ranges, gaining a fast quantitative picture of the system and accelerator status at any time. An example of this is represented in Fig. 3.6, which shows various interesting correlations: SuperKEKB loss monitors show spikes over the standard baseline whenever injection is performed, while the two diamonds considered in this plot are very sensitive to beam-current variations; in the second part of the time range represented in Fig. 3.6 both the loss monitor and the diamond readout become noisy, in correlation with the progressive opening of collimators (light-green).

One outstanding task was controlling pedestals, especially for the four sensors participating in the abort logic. In this context "pedestals" are the measured values of currents or dose rates from each diamond detector when no significant ionizing radiation is present, that is, in the absence of circulating beams. Pedestal values may vary systematically in time due to various causes related to environmental changes. Normally pedestal drifts showed monotone or oscillating trends, but sudden large shifts were observed occasionally,
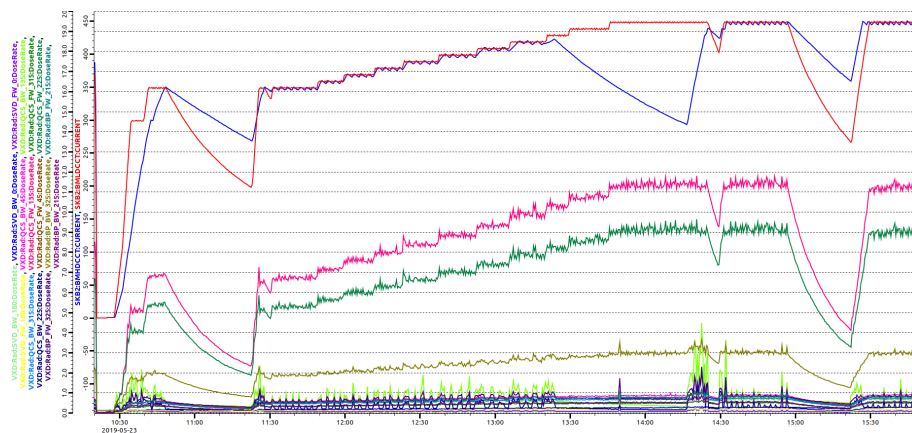
Figure 3.5: Screenshot of a live plot of beam currents (red and blue lines) and diamond readouts (other colored lines) as a function of time. I used this live plot to observe diamond behaviour when currents were being increased.
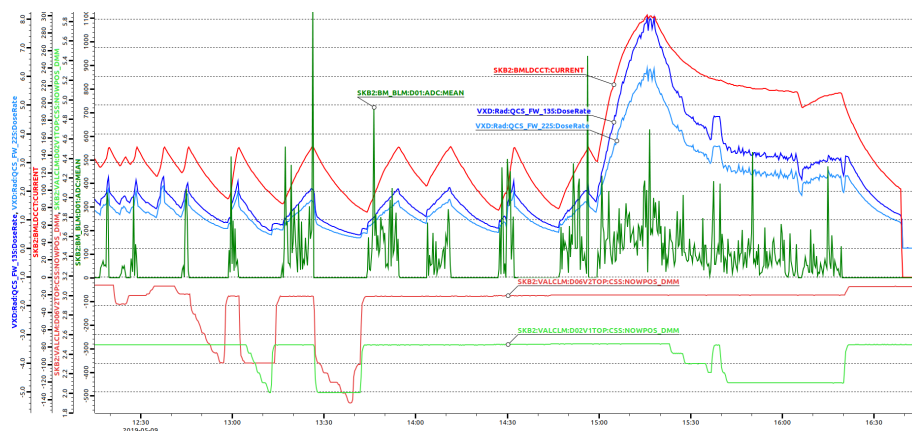


Figure 3.6: Diamonds dose rates (blue and light-blue), LER beam current (red), collimators aperture (orange and light-green), and SuperKEKB loss monitor (green) archived data, displayed as a function of time. I used such plots to explore correlations between different variables.

as shown in Fig. 3.7. Shifts were observed after large radiation losses or, more frequently, after reconfigurations or restarts of the DCUs. These pedestal variations were more evident in the abort-enabled diamonds, which were set on a larger measurement range. The pedestal variations of abort diamonds are more critical. Sufficiently large pedestal shifts modify the effective value of the abort threshold, thus exposing the detector to risk of dangerous irradiation or of disrupted data taking, if the beams are unnecessarily aborted due to misguided abort requests triggered by pedestal drifts.

Pedestal updates were done in no-beam condition, so that diamonds were not exposed to significant radiation and a realistic estimate of noise fluctuations was possible. At the beginning of my work, the procedure to update pedestals required the visual evaluation of pedestal values and their manual updates in configuration files on a local PC. This procedure was quite error-prone and inefficient, as it needed at least 30 minutes, resulting often in excessive data-taking time losses. I proposed an automatized procedure whose implementation improved the data-taking efficiency significantly by reducing the whole operation to less than 10 minutes.

I also intervened on the diamond abort logic, by updating and improving the values of thresholds and moving dose-integration windows based on analyses of past abort
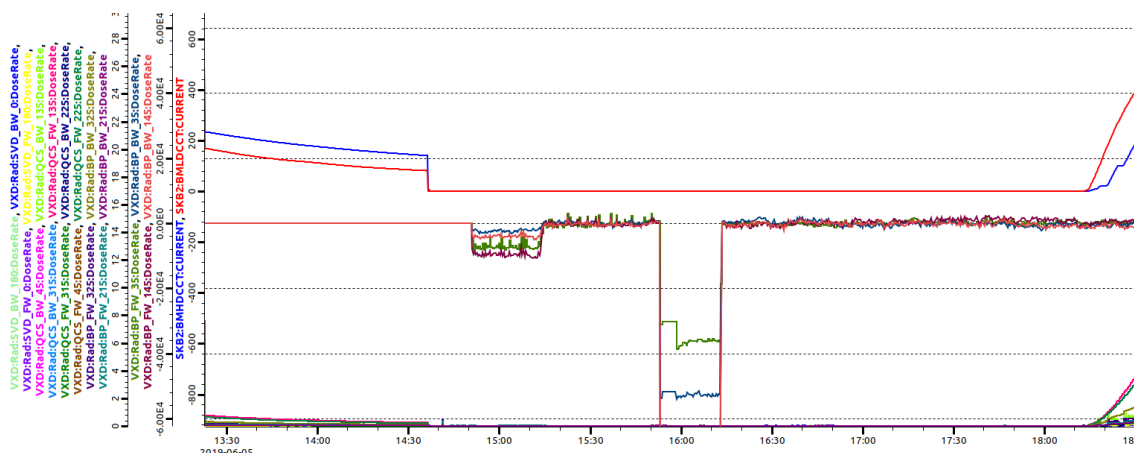
Figure 3.7: Beam currents (red and blue lines) and diamond dose rates (other colored lines) as functions of time. Various shifts of pedestal values were observed while beams were off and I was working on the DCUs configuration.
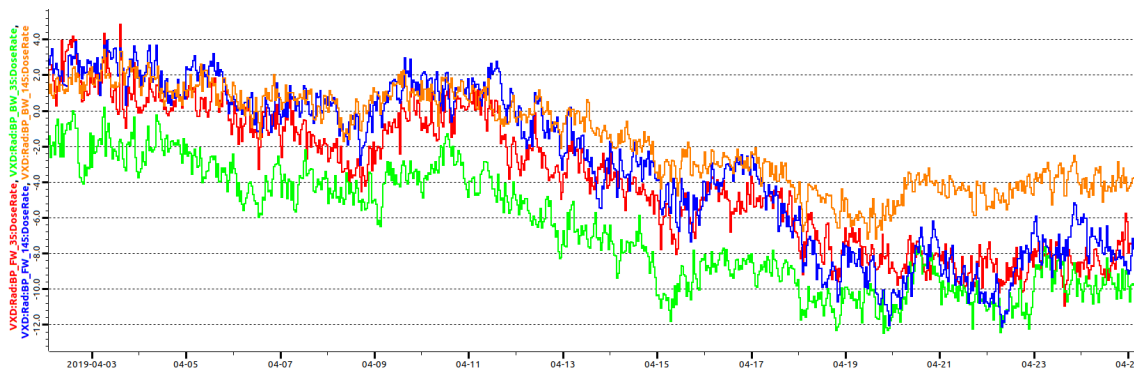


Figure 3.8: Beam-pipe diamonds (one color per sensor) dose rates as functions of time during a long period without circulating beams (April 3rd to April 25th). Pedestal drifts of more than 10 mrad are evident.

phenomenology. Since the time evolution of beam losses in abort events is not unique, post-mortem data were needed to identify patterns of possible precursors of dangerous beam losses. Some examples of dose-rate phenomenology from diamond 100 kHz data are shown in Fig. 3.9: in different beam-abort events, the dose rate as a function of time may increase very rapidly or more smoothly, and either reach the beam-abort threshold or not, when some other SuperKEKB loss monitor issued the beam-abort request earlier.

Because machine conditions varied significantly during early physics data-taking, setting appropriate thresholds was a challenge. Too high thresholds may expose the detector to possible radiation damage; too low thresholds result in misguided aborts, due to noise fluctuations, that compromise data taking efficiency.

Tab. 3.4 reports the thresholds I set during this part of Phase 3. I first incremented them, because machine injection caused too high backgrounds, resulting in diamonds repeatedly aborting beams during injections and disturbing the ongoing optimization of beam optics by SuperKEKB. The example of Fig. 3.10 shows many beam aborts (with beam currents dropping to zero) from March 2019. Spikes in the diamond signals are not visible because the 10 Hz sampling averages them to lower values.

After this change, operations continued smoothly until a major accident happened, which is detailed in the next section. Because of this accident, I had to change the cur-
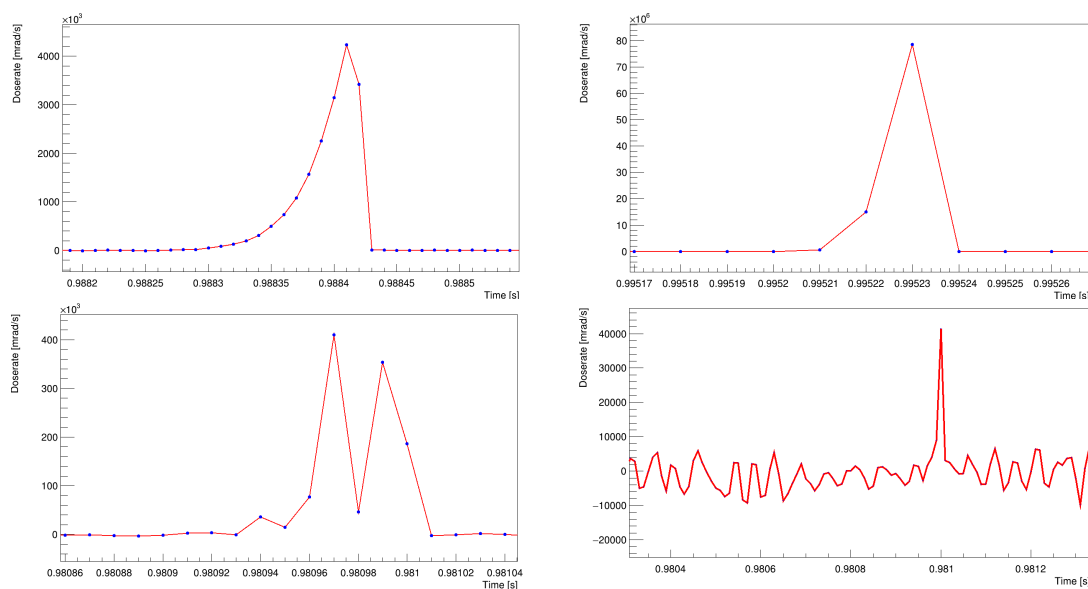
Figure 3.9: Examples of dose rate seen by diamonds in various aborts as a function of time. The top panels show dose-rate associated with losses that triggered diamond aborts. The bottom left plot shows a peculiar dose-rate shape. The bottom right plot shows the dose-rate corresponding to an abort issued by another SuperKEKB loss monitor: a background spike is visible, but the dose-rate seen by diamonds is lower in this case with respect to the three other examples.
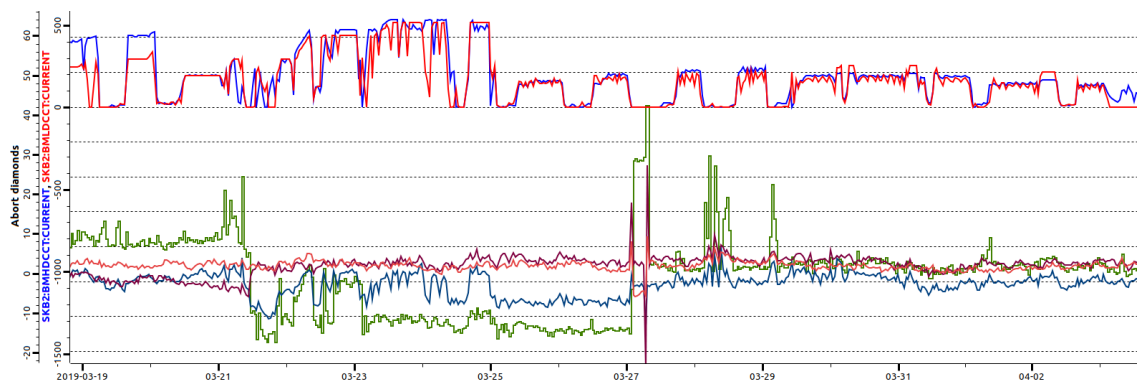


Figure 3.10: Beam currents (red and blue lines) and DCU 1 diamond dose-rates (other colored lines) as a function of time during early Phase 3.

rent range of the four abort-enabled diamonds to the highest setting, and to increment thresholds as a consequence of the larger noise fluctuations. However, I further studied the noise fluctuations and observed that they were much lower than expected: I therefore decreased the fast threshold back to the initial value (10 mrad in 1 ms), because of the evident improvement in backgrounds with respect to the beginning of Phase 3. Although the 1 ms noise fluctuation was well below the threshold, slow aborts were frequently issued, due to larger-than-expected pedestal drifts observed using this range. It happened twice that the pedestal had so high an offset to continuously trigger the slow threshold.

Finally, part of my standard tasks also included minor hardware interventions. For instance, I investigated the causes anomalous behaviour shown by DCU 4, and tracked it down to excessive noise and communication issues. As shown in Fig. 3.11, one channel showed sudden, short-lasting shifts of pedestals and an overall noisier signal. Following my findings, the DCU 4 was shipped back to Trieste for further debugging and two new units

| Period | Fast threshold (in 1 ms) | Slow threshold (in 1 s) |
|---|---|---|
| March 11 - 27 | 10 mrad | 200 mrad |
| March 27 - June 05 | 50 mrad | 1000 mrad |
| June 05 - June 12 | 70 mrad | 2200 mrad |
| June 12 - June 27 | 10 mrad | 5000 mrad |
| June 27 - July 01 | 10 mrad | 10000 mrad |

Table 3.4: Thresholds implemented on abort diamonds in the first months of Phase 3.

arrived at KEK. I tested their base functionalities with a Labview program [33] provided by the manufacturer, to verify they were not damaged while travelling to Japan, and installed them during the summer shutdown.
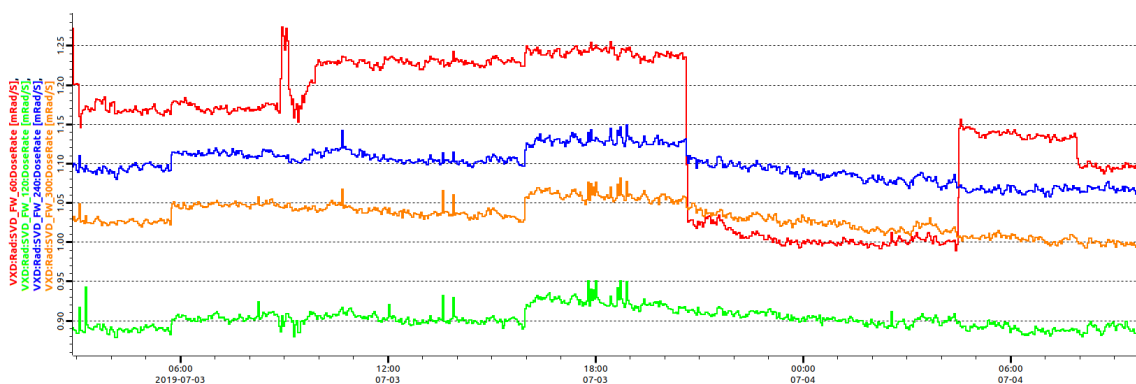


Figure 3.11: DCU 4 diamonds dose rates as a function of time (one color per sensor). The anomalous behavior of the SVD_FW_60 signal (red line) is evident, with spikes and several pedestals shifts with no such changes in the other diamonds.

### 3.2.2 Exceptional interventions

During my work as an on-site diamond expert, a few out-of-ordinary issues occurred that required exceptional interventions. The two major events were a power-supply failure of one QCS magnet and a exceptionally large background spike.

#### 3.2.2.1 May 28 QCS power supply failure

On May 28, the power supply of one of the forward QCS magnets had a failure. Power first went through a slow ramp-down pattern, which went undetected by the accelerator control system. This generated growing beam losses that started to hit the magnet, heating it until it lost its superconducting properties (magnet quench). Because of the quench, the beam ceased to be properly focused right in the critical position along the ring adjacent to the interaction region. Hence the detector was illuminated by a much higher than normal flux of background particles until an abort was delivered by an accelerator loss monitor (and not by the diamond system).

Such high doses received by the detector in a short time can cause damage both to the sensors and the readout electronics, especially in the innermost layers. The key question in this occurrence was why the diamond system did not issue an abort.

By analysing post-abort memory dumps, I observed that diamonds did not issue an abort because their current saturated the measurement range. The distribution of the saturating dose rate as a function of time is shown in Fig. 3.12. If the dose rates read by diamonds saturate, the abort logic integrates the potentially much lower full-scale value ($\approx$160 mrad/s) instead of the actual dose. To issue an abort in such situation, the DCU needs to integrate about 30 samplings of saturated values, which correspond to $\approx$300 $\mu$s, too long a time to ensure detector safety. In this accident, the abort was issued after $\approx$100 $\mu$s by other SuperKEKB loss monitors, still too late to avoid temporary damages, especially to the PXD.
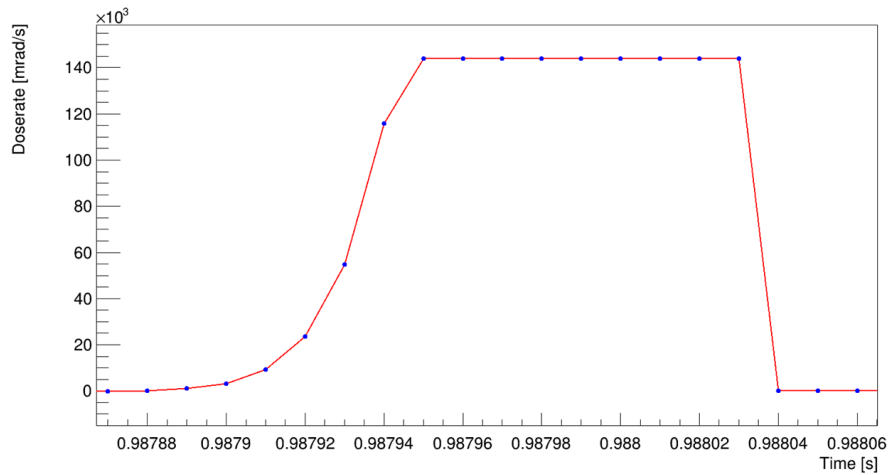


Figure 3.12: Dose rate seen by the most affected diamond as a function of time, for the QCS quench event of May 28th. The clipping at $\approx$ 146 mrad shows that the high dose saturated the readout.

After this accident, we switched the measurement range for abort diamonds to the largest value. New thresholds of 70 mrad (fast) and 2000 mrad (slow), were set basing on extrapolations. This procedure required time without beams to

- reprogram the DCU from a new configuration file with updated range and threshold;

- update pedestals based on the 10 Hz data stream;

- issue manual abort signals to evaluate noise in 100 kHz data available in post-abort memory dump files;

- determine if thresholds were too low and might trigger fake aborts from a fast evaluation of noise at 100 kHz.

The initial threshold value was based on 100 kHz noise-values extrapolated from 10 Hz data. To analyze noise fluctuations after the change, data collected with simulated aborts were summed in intervals of 1 ms and used to fill histograms. The standard deviation, used to decide which threshold to set, was observed to be a factor of ten lower than expected, as shown in Fig. 3.13, allowing some further margin to lower the threshold. Hence I decided to keep a fast threshold of 70 mrad/s and to possibly lower it later.

The range change showed immediately to be effective: on June 6, another power-supply failure affected the same QCS magnet. The diamonds electronics did not saturate, as shown in Fig. 3.14, and delivered the abort after a few readings, about $\approx$ 70 $\mu$s before other independent loss monitors could react. The magnet quenched again but following
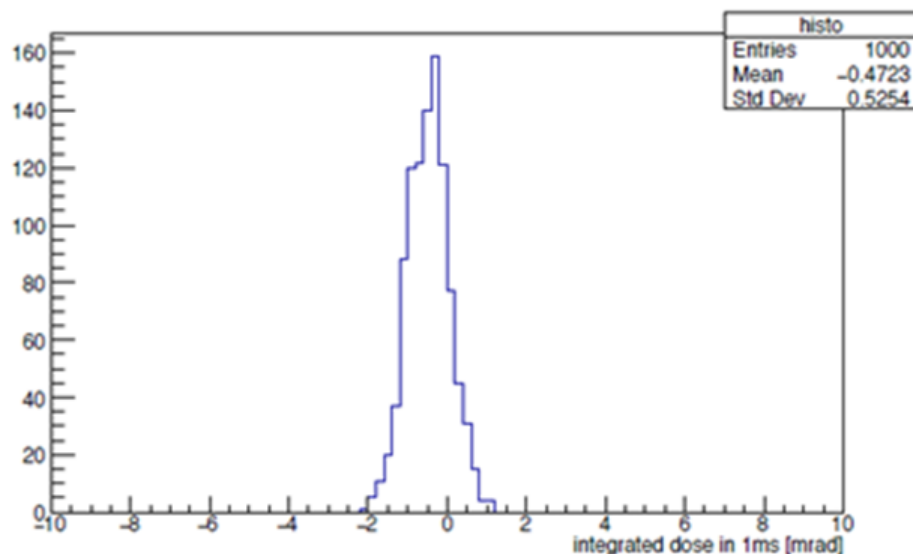
Figure 3.13: Dose-rate distribution of 100 kHz pedestal data summed in independent 1-ms-time intervals; the standard deviation is of $\approx 0.5$ mrad, much lower than the "fast" threshold set.

my improvement the detector remained protected, integrating a much lower radiation and reporting no damage.
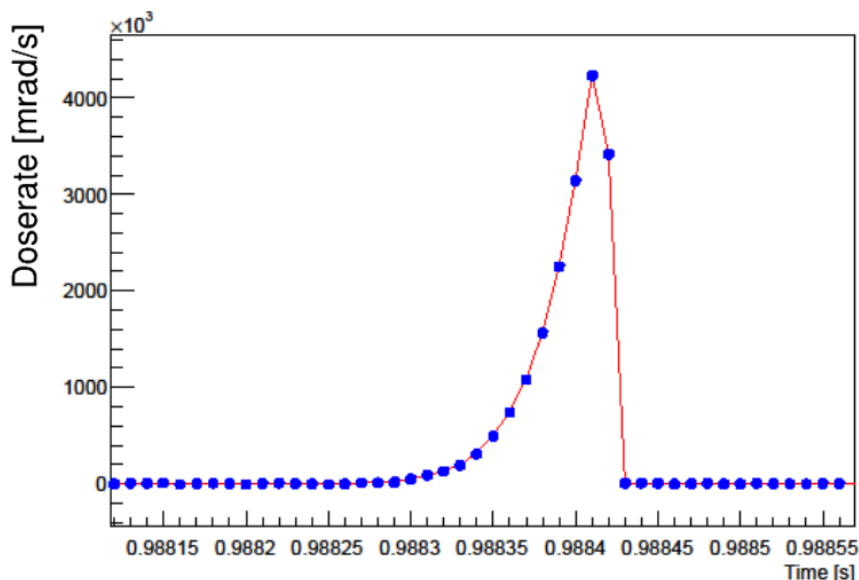


Figure 3.14: Dose-rate seen by BP_FW_45, as a function of time, in the QCS quench of June 6th, 2019. With the new dynamic range, the diamond signal did not saturate and the full background radiation spike is properly sampled.

#### 3.2.2.2 June 9 (alleged) beam-dust event

On June 9, a large background-radiation spike was observed. Although a beam abort was issued by the diamond system, the detector reported malfunctions, especially in the PXD electronics. The dose rate seen by diamonds from 100 kHz post-abort data is shown in Fig. 3.15, showing values so high that they saturated for a few 10s of microseconds

even with the least-sensitive range. Furthermore, one of the diamonds reached the peak of its dose rate at a later time with respect to the other three, which could be explained by a beam deviation caused by non ideal functioning of the abort mechanism. This may have perturbed the beam during abort, resulting in uncontrolled beam losses hitting other diamonds for a few revolutions, before the abort was completed. A possible interpretation given by accelerator colleagues to this burst is a "beam-dust"-like event, that is, scattering of beam particles with a residual dust fragment inside the beam pipe.
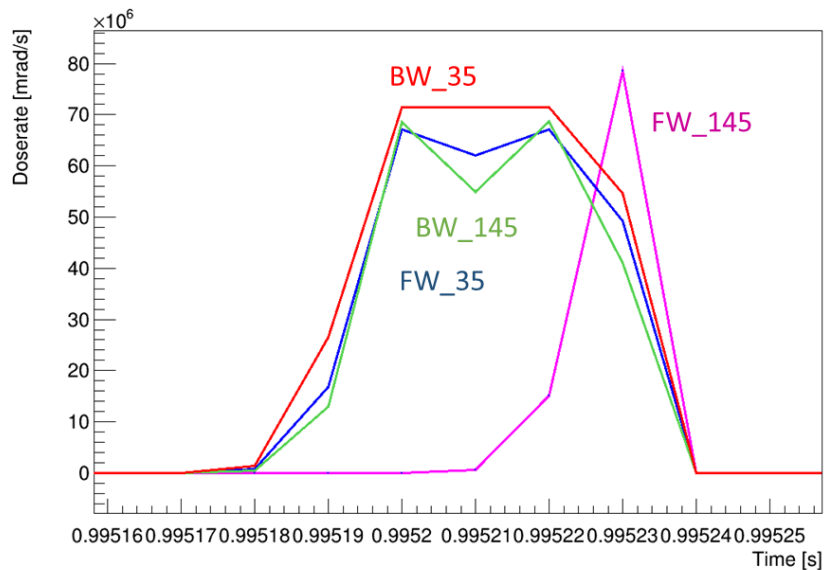


Figure 3.15: Dose rate as a function of time for the four abort-enabled diamonds (DCU 1).

The severity of the temporary malfunctions registered in the detector, even if the abort was issued very rapidly, caused some concern in the collaboration. Besides damage to the detector, one of SuperKEKB PiN diodes ceased to function after this event, and a collimator was damaged.

In order to achieve a more detailed characterization of the event, and possibly derive countermeasures, I evaluated the integrated dose by reproducing offline the conditions of the abort logic. I chose a moving time window of 1 ms (Fig. 3.16), summing every 10 $\mu$s the next value and subtracting the oldest one. This allowed to identify the specific measurement that caused the abort. A significant delay was observed between when the abort was issued and its completion, as shown in Fig. 3.16: the first data point higher than 10 mrad corresponds to the abort request by diamonds, while the plateau starts when the abort is completed and beam losses vanish. The delay between these two events is of approximately 50 µs; most of the dose integrated by detector is due to this delay.

Before this event, the 50 $\mu$s difference between abort request and completion was not noticed, because diamonds with the more sensitive range were taking more time to issue aborts, due to saturation, and the difference in the dose integrated until abort issuing or until completion was negligible. However, in this event the dose integrated up to the abort-request issuing is of 100 mrad, while the total integrated dose until abort completion is of $\approx 2.7$ rad. This large dose caused temporary malfunctions in various detectors of Belle II and raised awareness on the issue. After I reported this result to the collaboration, we
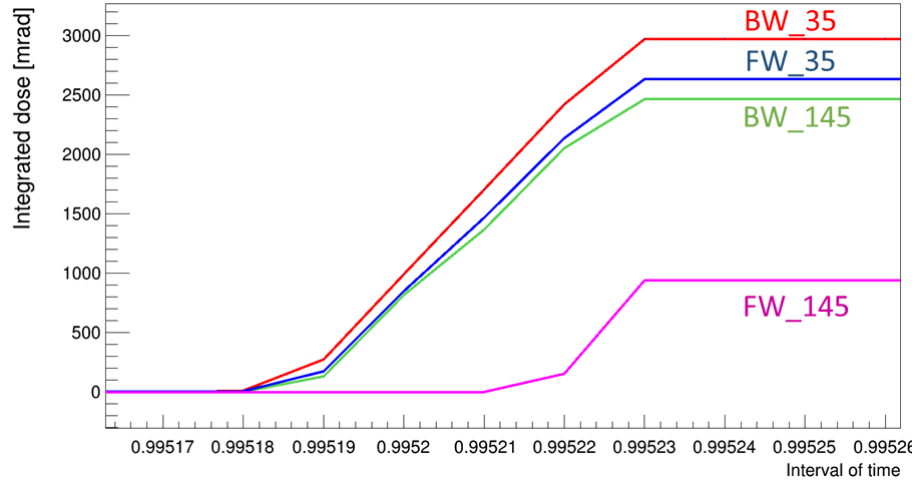
Figure 3.16: Integrated dose as a function of time for the four abort diamonds (DCU 1). The integration is performed in a moving 1 ms-window, updated every 10 µs. The integrals reach their maxima when the beams are actually aborted and the beam losses go to zero

investigated the causes of the delay. We performed a detailed analysis of the timing of the abort process, identifying the chain of possible delays, from the time an abort is issued to its completion, ending up in estimating about 40 µs. A scheme of this delay chain is shown in Fig. 3.17.
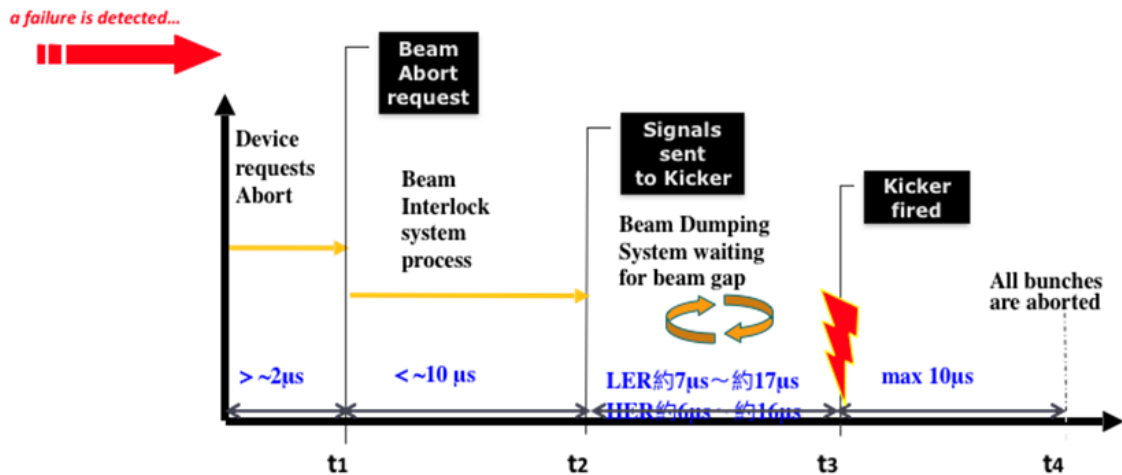


Figure 3.17: Scheme of the abort delays: the contributions to the total delay are shown.

We then investigated the feasibility of improvements to reduce delay where the detector is subjected to radiation even if a beam-abort is ongoing. We figured out that one of the main limitations of the current configuration is that the SuperKEKB control room, where all abort signal are gathered at the global logic of abort delivering, is opposite to Belle II location on the accelerator ring, at ≈ 1 km distance, which implies up to ≈ 10 µs of propagating time from the diamond system.

Following my work, various proposals are under discussion to mitigate the effect. One is to send the abort signal from diamonds directly to the kicker magnet. Another option is to install additional diamond sensors in other sections of the ring to integrate the SuperKEKB loss monitor coverage. Alternatively, doubling the abort gaps would reduce the waiting

time but would have non trivial impact on beam dynamics and luminosity reach. On the radiation-monitor side, a modification of the FPGA firmware is in progress that allows comparing moving sums with thresholds every 2.5 μs, instead of 10 μs.

### 3.2.3 Background studies

A third contribution I gave to the diamond system consisted in performing preliminary analyses aimed at estimating the nature and composition of beam-backgrounds. The goal of these studies is to provide SuperKEKB physicists feedback that assists them in understanding which tunings can be attempted to reduce the global beam background. One example of such analyses is described as follows.

One limitation in any data-simulation comparison of beam phenomenology is that SuperKEKB operators have access to simulated samples generated with only a restricted subset of operation configurations of those used in collecting experimental data. Therefore we use measurements on real diamond data to extrapolate back to the configurations available in simulation, so that consistent comparisons are possible. This extrapolation involves various approximations described as follows.

I used diamond data collected in single beam operations, and assumed that only two components contribute to the single beam background: Touschek and beam-gas Coulomb scattering. This simplified, heuristic model, takes into account both the independence of the beam-gas scattering rate from the beam size and the inverse proportionality of the latter with the Touschek rate. The model parametrizes the dose rate seen in diamonds as

$$D_R = B \cdot IP \ + \ T \cdot \frac{I^2}{n_b \sigma_y}, \tag{3.1}$$

where $B$ and $T$ are the coefficients that are related to the fractions of beam-gas and Touschek contributions respectively, $I$ is the beam current, $P$ the pressure in the beam pipe, $n_b$ the number of bunches, and $\sigma_y$ the vertical beam size at the interaction point. I measured the parameters $B$ and $T$ in single-beam data, then extrapolated the dose rate from these two effects to the design conditions implemented in the standard SuperKEKB beam simulation, and finally compared my results with simulation.

To determine the parameters $T$ and $B$ in data, I aligned the information of diamond data, sampled at 10 Hz, with the other relevant beam informations, sampled at 1 Hz. Since beam parameters and dose rates vary slowly during storage, I averaged diamond data over 30-s-periods and synchronized the results with beam parameters samplings using time-stamps. The study focused on storage-regime backgrounds, therefore I excluded data taken during injections. In addition, because I used LER data only, I excluded data from the QCS_BW_135 and QCS_BW_225 sensors, which are sensitive mostly to HER, and did not include SVD diamonds in the analysis, for which no simulation was yet implemented at the time of this study. Because the simulation was available only for beams with 1576 circulating bunches, and the ratio of the two radiation sources depends on the number of bunches, I used only data collected with $n_b = 1576$ to mirror the simulated setup.

To determine $T$ and $B$, I performed a $\chi^2$ fit of the data with the function

$$\frac{D_R}{IP} = B \ + \ T \cdot \frac{I}{P n_b \sigma_y}. \tag{3.2}$$

For these preliminary studies, the small uncertainties on the beam parameters $I$, $P$, $n_b$, $\sigma_y$, were marginally relevant, and only uncertainties on the diamond dose-rate average were considered. An example of data from two diamonds is shown in Fig 3.18 with fits

overlaid. Even though the model used to fit is simplified, all the fits yield a reasonable reduced $\chi^2$.
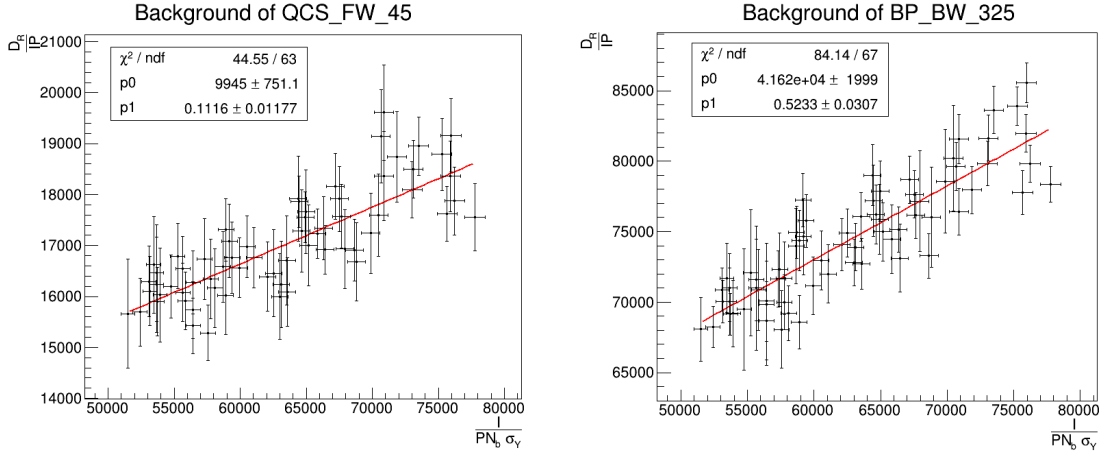


Figure 3.18: Results of the fit of dose-rate data seen by two diamonds.

Once I obtained the $B$ and $T$ coefficients, I extrapolated the two background contributions at the design condition using the relation (3.1) which makes them comparable with the background simulation. The reference beam values used are $I = 1.2\,\mathrm{A}$ for LER and $I = 1.0\,\mathrm{A}$ for HER, $P = 1\,\mathrm{nTorr}$ for both beams, $n_b = 1576$ for both beams, $\sigma_y = 38\,\mathrm{\mu m}$ for LER and $\sigma_y = 36\,\mathrm{\mu m}$ for HER. Table 3.5 shows the extrapolation of the fit results and the ratio between those and the simulated values. The relative uncertainties on the Touschek and beam-gas fractions are about 10 %, by taking into account the uncertainty on the parameters derived from the fit only. The uncertainties on the simulated values are neglected because of the large sample-size.

These preliminary results show that, to a first approximation, the contributions of beam-gas and Touschek background illuminating the beam pipe are comparable in size and consistent with similar results based on PXD and SVD data. On the other hand, QCS diamonds indicate that the Touschek effect is the dominant contribution to the beam background in that region. The agreement with simulation is reasonable on the beam pipe region, while a greater discrepancy is observed for the QCS regions and needs to be investigated.

Many factors can contribute to these discrepancies. Probably, an important contribution is due to the heuristic relation used, which approximates background to be caused by just these two effects. The approximated relation (3.1) is probably adequate near the IP, where the beams are shaped in the peculiar configuration of the nano-beam scheme. The rapidly changing beam shape in the QCS region may introduce nonlinearities that spoil the approximation of (3.1). In addition, the approximations in the SuperKEKB simulation are known not to reproduce exactly beam background in the QCS regions. A more detailed offline analysis both of single-beam data and of the simulation model will be needed, but it is outside the scope of this thesis.

|  | Extrapolated Touschek frac. | Extrapolated beam-gas frac. | Touschek data/MC | Beam-gas data/MC |
|---|---|---|---|---|
| BP_FW_325 | 0.56 | 0.44 | 1.78 | 0.18 |
| BP_FW_215 | 0.38 | 0.62 | 1.79 | 0.64 |
| BP_BW_325 | 0.32 | 0.68 | 1.53 | 0.85 |
| BP_BW_215 | 0.65 | 0.35 | 2.8 | 0.64 |
| QCS_FW_135 | 0.86 | 0.14 | 0.1 | 5.25 |
| QCS_FW_45 | 0.65 | 0.35 | 0.14 | 1.43 |
| QCS_BW_45 | 0.51 | 0.49 | 10.0 | 11.8 |
| QCS_FW_225 | 0.82 | 0.18 | 0.13 | 3.82 |
| QCS_FW_315 | 0.7 | 0.3 | 0.08 | 0.99 |
| QCS_BW_315 | 0.62 | 0.39 | 5.28 | 8.92 |

Table 3.5: Results of preliminary beam-background studies using LER single-beam data. The table shows the fractions of Touschek and beam-gas components expected at the reference simulated conditions and the ratio of the dose-rate extrapolated to the value obtained solely from simulations. Relative uncertainties on the fractions are $\approx 10$ % for all measurements, and they are the same also for the ratio to simulated values, which are considered without uncertainties. They are not indicated in the table.

## 3.3   Impact on diamond-system operations

In my stay in Japan I was on-site expert of the diamond system during the beginning of the Belle II physics operations. The principal results achieved are

- I reduced data-taking time losses by promptly solving ordinary issues of the diamond system;

- I improved the reliability and efficiency of the system by defining a semi-automatic procedure for pedestal setting that significantly reduced the data taking inefficiency;

- I analyzed data from major accidents and optimized the measurement ranges of the diamonds, to reduce the likelihood of repetitions of such events;

- I optimized the thresholds to ensure safe operation while coping with the increase of aborts due to noise and pedestals fluctuations;

- My offline analyses of diamond data and comparison with simulation offered important insight on the source and nature of beam backgrounds.

All of these improvements resulted significantly smoother and safer operations of the Belle II data taking for physics and will be crucial in the upcoming data-taking period expected in mid-October.

# Chapter 4

# A novel method for determining track-finding efficiency

This chapter describes the second part of my work. I first give an overview of charged-particle tracking at Belle II, then I introduce the original method I devised to determine track-finding efficiency and define its implementation on simulated samples. Finally, I apply the method on experimental data.

## 4.1 Motivation

Tracking is fundamental for the Belle II program. A large fraction of final states of $B$- and $D$-meson decays contain charged particles only, and in an even larger fraction tracks are the majority of final-states particles. Strong tracking is key to suppress background, thanks to the discriminating power against smoothly distributed backgrounds of the narrow signal-mass peaks due to precisely reconstructed momenta. In addition, reconstruction of momentum and decay position enables the determination of the decay time, which is an essential capability in many flavor-physics measurements. Similar considerations apply to $\tau$ studies.

In addition to tracking resolutions, track-finding efficiency is important. It is an essential input in all measurements in which determination of the absolute rate of a certain process is required. Moreover, a reliable determination of the tracking efficiency allows understanding the high-level detector performances paving the way for future improvements.

## 4.2 Tracking in Belle II

When a charged particle traverses an array of position-sensitive layers of tracking detectors, it deposits energy on the sensors traversed along its trajectory; such energies ionize charge that drifts and induces current signals on readout electronics. Figure 4.1 shows a Belle II collision event. Usually events have about ten charged particles in their final states, each leaving about 10 signals in the silicon detector layers and 50 signals in the drift chamber, for a total of about 600 measurement points. If the signals associated with the passage of tracks are sufficiently distinguishable from noise, a fine-grained sampling of the particle trajectory emerges, from which kinematic and decay-distance properties of the incident particle can be inferred. This is the goal of tracking, whose task is conventionally divided into steps:
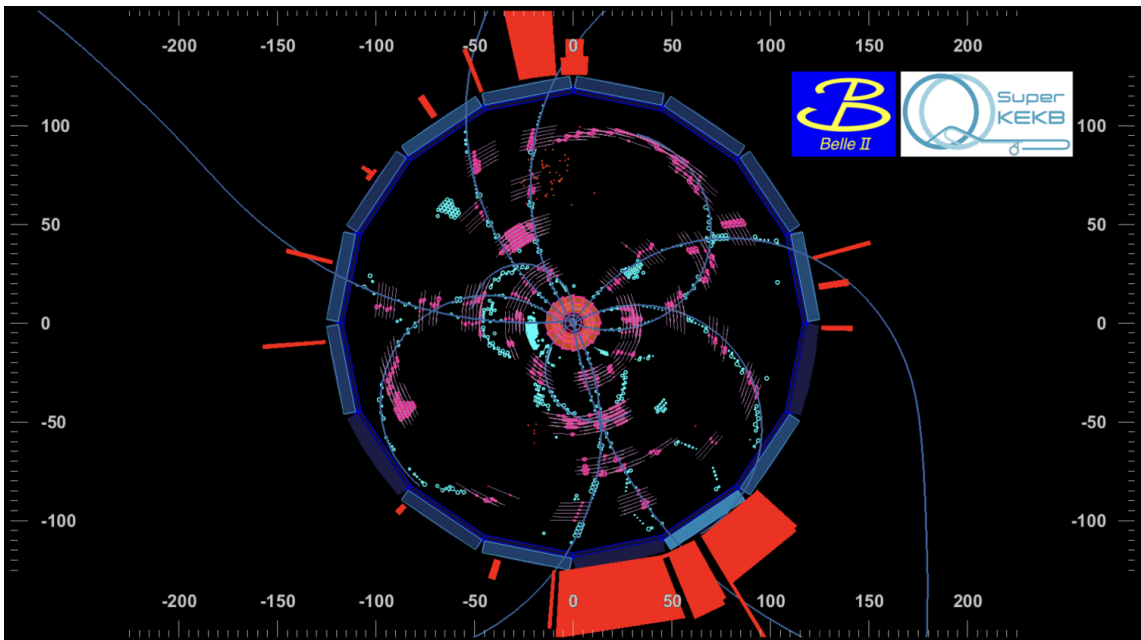
Figure 4.1: Example of a typical hadronic event in Belle II.

1. maximize the probability that an incident charged-particle produces signals in the tracking detector layers;

2. identify the measurement-points likely associated to the charged particles;

3. cluster them into "hits" to improve position resolution ("clustering");

4. combine them into sequences likely to be associated with the trajectories of charged particles ("pattern recognition");

5. fit them to the trajectories expected for charged particles, possibly exploiting the existing kinematic constraints, to estimate with maximum precision the final track parameters ("fitting").

The combination of the latter two tasks is called "track-finding" for the purpose of this work.

Not all tracks produced in a collision are reconstructed. Tracks that are outside of the detector acceptance are obviously lost. But other sources of inefficiencies exist. High beam-related backgrounds or noisy channels in the tracking detectors increase detector occupancy (the fraction of channels associated with signals over the total), which yield pattern-recognition difficulties because of the challenging combinatorial problem of sorting genuine track-related signals from the large number of overlapping signals. Interactions of the charged-particles with the detector material occasionally cause significant deviations in their trajectories. Because signals detected significantly away from the expected trajectory may not be properly associated by pattern recognition and track-fitting algorithms, this makes for another source of inefficiency. The amount of tracks that fail to be reconstructed is quantified with the track-finding efficiency.

The ideal trajectory of charged particles in an axial magnetic field parallel to the beam direction (as in Belle II) is an helix, where the longitudinal motion is driven by the component of the particle momentum along the field ($p_z$, longitudinal momentum),

the radius of gyration is determined by the component of the momentum in the plane transverse to the field direction ($p_T$, transverse momentum), and the rotation direction is determined by the particle charge. The position of the orbit in the transverse plane with respect to the detector axis depends on the space-point where the particle was originated: it includes the $e^+e^-$ interaction point for particles produced directly in the collision, but can also be displaced if the particle is originated from the decay of a long-lived parent.

Such model is described with five parameters. Because some of them vary along the trajectory, they are referred in Belle II to the point of closest approach (POCA) to the IP, shown in Fig. 4.2. They are

**$d_0$**: distance of the POCA to the IP in the $x$-$y$ plane (namely "transverse plane");

**$z_0$**: longitudinal distance of the POCA to the IP;

**$\tan \lambda$**: tangent of the angle between the transverse plane and the tangent to the helix in the POCA;

**$\phi_0$**: angle between the tangent to the helix at the POCA in the transverse plane and the $x$ axis;

**$\omega$**: signature of the curvature in the transverse plane;
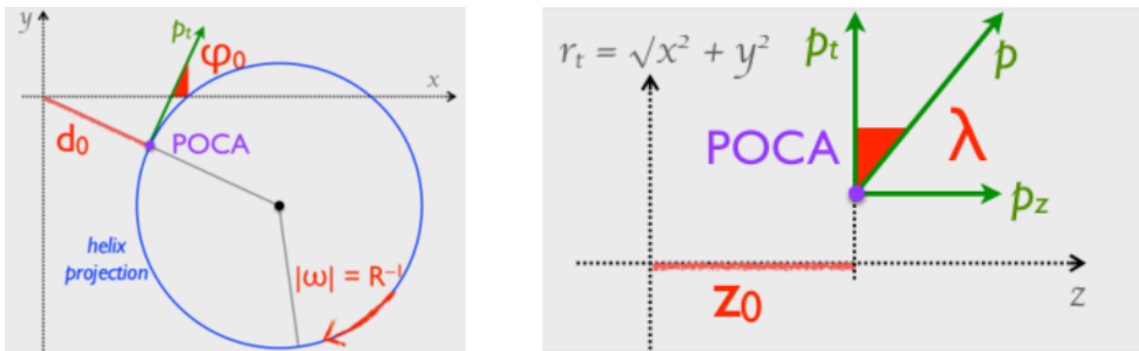


Figure 4.2: Illustration of the helix parameters used in track parametrization at Belle II. The parameter $\omega$ is not shown.

Charge, momentum, and space-point of origin of the charged particle are derived from these parameters.

Since particles usually "excite" more than one channel in each silicon sensor, sets of neighbouring measurement points are clustered into "hits" to use the distribution of charge over the excited channels to improve position resolution. In Belle II such clustering is performed directly at detector readout level. Space coordinates of clustered hits are directly fed to the pattern recognition algorithm.

Beam-background makes occupancy in PXD excessively high for efficient pattern recognition, which is performed using only CDC and SVD information. Various algorithms are used to identify the hits most likely associated with tracks, distinguishing them from noise or beam-background-induced hits and taking into account the known inoperative channels.

Both CDC and SVD use an algorithm that forms combinations of three hits (tracklets) on radially adjacent layers. The combinatorial complexity due to the high hit-density in SVD is reduced by means of filters that constrain the parameters of the candidate tracklets to lie within the predetermined ranges expected for typical Belle II tracks. Proceeding radially outward, tracklets are connected to each other to form longer track "stubs" , if they

share two hits. Every connection between triplets is assigned with a weight; the top CDC track candidate is the stub yielding the highest sum of weights. A complementary algorithm based on a global Legendre transformation of the hit positions is also implemented. In the approximation that trajectories are circles passing trough the IP, which is sufficiently accurate within the track-parameter resolution afforded by the CDC, every circle in the $x$-$y$ plane is mapped in a point in the Legendre space. Identifying an accumulation in such space leads to a rough determination of the parameters of the track.

Candidates from CDC and SVD are finally combined into track candidates, which may contain duplicates. The final selection of tracks chooses the best track candidates based on fit quality. Each pair of the final tracks cannot share more than a hit.

In the track fitting process, a first iteration uses $\chi^2$ minimization to find a rough approximation of the helix parameters. Since trajectories may deviate significantly from the ideal path a simple $\chi^2$ fit is insufficient for efficient track fitting and precise determination of track parameters. Hence Belle II uses an iterative approach based on the Kalman filter. The trajectory of the track is discretized into radial "steps" and the algorithm determines the "evolution" of the track from one step to the next. For every hit, the algorithm takes into account both the measurement, and the predicted position of the next hit, based on the track parameters at the previous step and on a statistical parametrization of multiple scattering effects based on the known distribution of material along the trajectory. Informations on measurement and prediction are combined to define the most likely hit position. To further improve this procedure, the algorithm is applied both starting from the innermost hits and vice versa.

## 4.3 Track finding efficiency

In general, efficiency is defined as the fraction of positive outcomes ($n_{\text{ON}}$) out of a fixed number of total trials $n_{\text{TOT}} = n_{\text{ON}} + n_{\text{OFF}}$,

$$\varepsilon = \frac{n_{\text{ON}}}{n_{\text{TOT}}}.$$

Efficiency has a binomial distribution. For an unbiased determination of efficiencies, the fixed number of trials should be known without using information associated with the process of which we desire to infer the efficiency. In addition, the effect of detector acceptance should also be considered. Genuine charged particles produced in the collision can go unreconstructed either for intrinsic inefficiency or because they are fully or partially outside of the acceptance region (geometric inefficiency). In terms of efficiency definition, this reflects into specifying precisely what $n_{\text{TOT}}$ is. For simplicity, we choose not to distinguish the two effects in this explorative work aimed at demonstrating the feasibility of the method. However, no conceptual obstacle prevents from determining separately two sources in a further refinement. Therefore I refer to the product of intrinsic efficiency and acceptance as "efficiency" in what follows.

Current methods used to measure track-finding efficiency at Belle II are based on the use of radiative Bhabha decays or on $\tau$ lepton pairs.

In radiative Bhabha decays, $e^+e^- \rightarrow e^+e^-\gamma$, the kinematic properties of one track can be determined from the other track and the radiated photon. Even if the other track is not reconstructed in the tracking detector, it will still leave an energy cluster in the ECL and be reconstructed as a photon. Efficiency is determined using events that have a reconstructed $e\gamma$ pair and an energy deposit in the ECL, using the fraction of events in which the third track is correctly reconstructed. Because of the large radiative Bhabha cross section of

$\approx 300\,\mathrm{nb}$, which results in a rate of 3000 events per second at current luminosities, this method exploits abundant samples even after the accept-rate suppression imposed by the trigger on these "less interesting" processes. The principal limitation of this approach is the poor reach at low $p_T$ values, because Bhabha electrons from 10 GeV collisions have momenta of a few $\mathrm{GeV}/c$ typically (see Fig. 4.5 right).

The $\tau$-pair-method uses $e^+e^- \rightarrow \tau^+\tau^-$ events in which one $\tau$ decays in a leptonic final state $l\overline{\nu}_l\nu_\tau$ and the other in an hadronic final state. Events are selected in which there are three tracks and a lepton. In a $\tau$ decay where only two tracks are reconstructed, charge conservation imposes the presence of the third track. The ratio of the events with three tracks and a lepton, to the sum of them and the events reconstructed with two tracks and a lepton, is used to determine the track-finding efficiency. Thanks to the large branching fractions of $\tau$ decays, this method exploits large samples, as with current luminosities it has a rate of about 1.4 events per second. As a drawback, the broad $\tau$ mass distribution resulting from a non fully reconstructed peak makes it challenging to select signal events without conspicuous inputs from simulations. In addition, the probed momenta do not extend below $\approx 1\,\mathrm{GeV}/c$ (see Fig. 4.5 left).

## 4.4   A novel approach

A method for measuring track-finding efficiency needs to infer both the number of total tracks traversing the tracker and the number of those reconstructed. The use of a fully reconstructable (i.e., without neutrinos) decay channel helps to determine $n_{\mathrm{ON}}$ because the strongly distinctive invariant masses facilitate separation of signal from background. However, the determination of $n_{\mathrm{TOT}}$ is usually more challenging. In fact, if the decay is fully reconstructed to get $n_{\mathrm{ON}}$, the unavoidable lack of one track in the reconstruction of $n_{\mathrm{TOT}}$ spoils the discriminating power of the invariant mass, making the determination of the efficiency denominator harder. This is usually circumvented by using decays whose final states can be fully reconstructed using independent detectors. A standard example are $J/\Psi \rightarrow \mu^+\mu^-$ decays, where a peaking signal may still be identified using muon detector information only, provided they offer sufficient momentum resolution. However, in $B$-factories, the production of $J/\Psi$ mesons is quite suppressed and unable to yield a sufficiently large sample for satisfactory efficiency determination. We therefore investigated if any abundant decay exists, with kinematic properties such that $n_{\mathrm{TOT}}$ can still be determined precisely while keeping the efficiency determination unbiased. A promising option is offered by the decay

$$D^{*+} \rightarrow D^0[\rightarrow K^0_S(\rightarrow \pi^+\pi^-)\pi^+\pi^-]\pi^+,$$

where an orbitally excited $D^{*+}$ meson decays through the strong interaction into a $D^0$ meson and a low-momentum pion just after production. The $D^0$ meson flies and then decays into two opposite-charge pions and a $K^0_S$ meson, which flies further and then decays into other two pions. The final state has five charged pions. Here and in what follows, charge-conjugate decays are always implied.

The key feature here is that the small mass difference between $D^{*+}$ and $D^0$ mesons strongly reduces the kinetic energy available in the $D^{*+} \rightarrow D^0\pi^+$ decay to $Q \approx 7\,\mathrm{MeV}$. Such small released energy allows to see a $D^{*+}-D^0$ mass-difference signal also if one $\pi$ from the $D^0$ decay is not reconstructed. This striking enabling feature is displayed in Fig. 4.4, where the mass-difference distributions of simulated $D^{*+} \rightarrow D^0[\rightarrow K^0_S(\rightarrow \pi^+\pi^-)\pi^+\pi^-]\pi^+$, decays reconstructed by using all five tracks (full reconstruction) or by missing a $D^0$ pion partial reconstruction) are shown. A scheme of what is meant by partially reconstructing

a decay is shown in Fig. 4.3. Therefore, if one manages to extract a visible partially reconstructed signal even in presence of background, one achieves a determination of $n_{\mathrm{TOT}}$ that is unbiased against the missing pion.
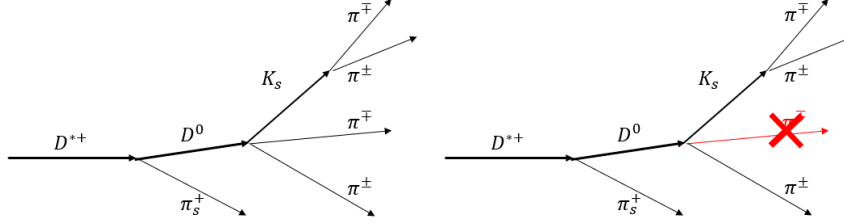


Figure 4.3: Conceptual sketch of (left) a fully and (right) a partially reconstructed $D^{*+} \to D^0[\to K_S^0(\to \pi^+\pi^-)\pi^+\pi^-]\pi^+$, decay. The probe track is a pion from the $D^0$ decay while the $K_S^0$ pions are always reconstructed.

This process is all the more attractive for it is also relatively abundant. The $e^+e^- \to c\bar{c}$ cross section is 1.30 nb and $c$-quarks form $D^{*+}$ mesons with 25.5% probability, $D^{*+}$ mesons decay in $D^0$ with a branching fraction of 67.7% and then the $D^0$ branching fraction into the desired final state is 2.85%, resulting in a few thousand decays per day at the at the current luminosity. Furthermore, $D^{*+}$ mesons can also be produced in $B$-meson decays, providing additional signal.
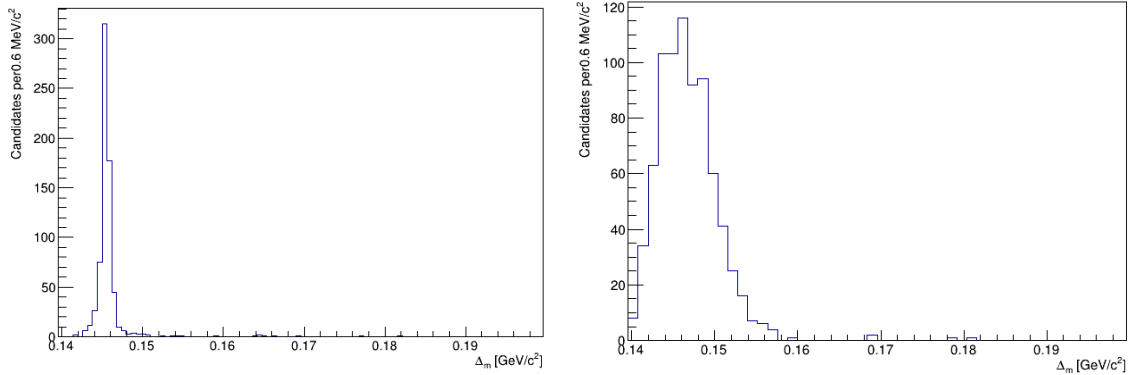


Figure 4.4: Distributions of $D^{*+} - D^0$ mass difference for fully (left) and partially (right) reconstructed simulated signal decays.

The track-finding efficiency for the probe pion is determined by

$$\varepsilon\left(\pi^{\mp}\right) = \frac{N_{\mathrm{FR}}}{N_{\mathrm{PR}}} = \frac{N\left[K_S^0(\to \pi^+\pi^-)\pi^+\pi^-\right]\pi_s^+}{N\left[K_S^0(\to \pi^+\pi^-)\pi^{\pm}\right]\pi_s^+},$$

where the denominator is the number of partially reconstructed signal decays and the numerator is the subset of these that gets fully reconstructed. To exploit the kinematic advantage we determine the event yields from the $D^{*+} - D^0$ mass difference distribution. While partially reconstructed $D^0$ and $D^{*+}$ do not show a peaking signal, in the mass difference the broadening due to the missing kinematic information from the unreconstructed pion is reduced, yielding a distinctively narrow structure that differs from the background.

This method is innovative for Belle II, but similar approaches have been studied in LHCb [34] and Belle [35].

The challenges in performing this measurement are

- extracting signals sufficiently distinctive from background. This is most critical for the partially reconstructed signal, which is significantly broader than the fully reconstructed signal and therefore subject to larger background contamination.

- ensuring that $n_{\text{FR}}$, i.e. the fully reconstructed signal yield, is a proper subset of $n_{\text{PR}}$ to avoid biases in the efficiency determination. This is particularly critical when defining the selection criteria.

- properly accounting for the presence of "peaking backgrounds" in the mass-difference distributions of both partially and fully reconstructed decay. Peaking backgrounds are non-signal decays that have signal-like mass-difference distribution, and therefore may not be distinguished from signal in a fit. Their contribution could bias the efficiency, unless they are suppressed or modelled properly.

This method has the potential of offering significant advantages over the methods already in use at Belle II. It is naturally data-driven, as it does not need any direct input from simulation because the efficiency is measured directly from experimental data. It also allows probing much lower momentum ranges than the other methods, extending possibly down to nearly zero, as shown in Fig. 4.5. This is particularly attractive since at low momenta is where the effects of multiple scattering become more relevant and a detailed probing of the efficiencies is more needed. The minor limitation of our method with respect to the approaches existing in Belle II is that it requires larger samples to meet similar precisions.

As a general strategy for the exploration of a viable implementation of this approach, I decided to first define the whole analyses procedure on simulated data to ensure that the obtained performances are free from biases. In addition, defining the strategy on simulation allows to use the Monte-carlo-truth information, which is crucially useful to understand the sample and optimize the analysis procedure. The measurement followed the following steps:

- Processing and reconstruction of simulated and experimental data, which are subject to standard baseline requirements.

- Investigation of sample composition by means of MC-truth information to identify the major contributions to the sample and determine the nature and severity of peaking backgrounds.

- Investigation of a viable selection capable of keeping signal visible in the partially reconstructed sample while not penalizing excessively its yield. Selection requirements must be defined and applied on the events that populate the efficiency denominator and applied consistently on the same quantities for numerator candidates too, to keep the numerator a proper subset of denominator. Otherwise, fully reconstructed signal decays could exist that do not have a partially reconstructed counterpart, yielding a conceptual nonsense and biases in the determination of the efficiency.

- Accurate modeling of the mass-difference distributions for performing the fits of signal yields necessary to determine the efficiency.

- Extraction of the signal yields from the mass-difference distributions in samples of partially and fully reconstructed candidates and determination the efficiency for simulated decays.

- Application of the procedure on experimental data.
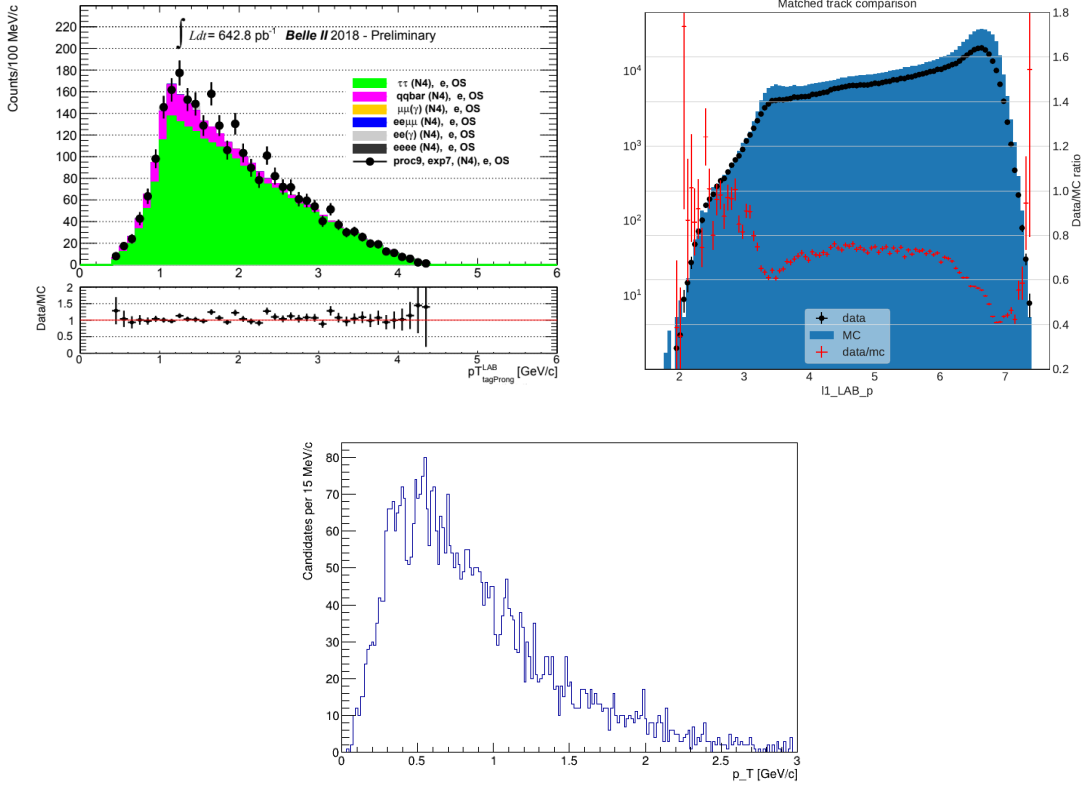
Figure 4.5: Momentum (total or transverse) spectra of the probe particles used for track-finding efficiency determination with $\tau$-pair method (top left), the radiative Bhabha method (top right) and with the method proposed in this work (bottom). Plots referring to the Bhabha and $\tau$-pair samples reproduced from Belle II internal notes.

## 4.5 Data and tools

The feasibility of the method depends crucially on the capability to identify and understand the properties of the three main components of the sample:

- **Signal**: $D^{*+} \to D^0[\to K_S^0(\to \pi^+\pi^-)\pi^+\pi^-]\pi^+$ decays;

- **Non-peaking background**: generic $e^+e^- \to q\bar{q}$ processes generating random combinations of multiple tracks that have smooth mass-difference distributions;

- **Peaking backgrounds**: processes showing mass-difference distributions indistinguishable from the signal distribution; because of the peculiar nature of the mass difference distribution, they can only be due to genuine $D^{*+} \to D^0\pi^+$ decays where the $D^0$ meson decays to final states other than $K_S^0\pi^+\pi^-$.

The most powerful instrument to gain such capability is the simulation, which is used to

1. understand the sample composition;

2. understand and model the relevant distributions of each of these components;

3. exercise the whole procedure on a realistic proxy of the experimental data.

I used the standard Belle II simulation to generate samples of all $e^+e^- \to q\bar{q}$ processes without any constraints on the $q\bar{q}$ evolution, resulting in a data set that mimics realistically the composition and size of the experimental data sample.

The simulation is known not to reproduce optimally some data features, mainly the PID efficiency and the intensity of beam backgrounds; however, in this study no PID information is used, and any additional track from beam-background processes would contribute as combinatorial background, which is typically properly identified by the fit. I simulated a sample corresponding to a 6 fb$^{-1}$ to mirror the size of the current Belle II data set.

Distributions of some relevant track variables from simulated signal events are shown in Fig. 4.6, to offer a quantitative feeling of the kinematic regime of our signal. For instance, it is evident how the momentum distribution supports our claim that the method is suited for probing efficiency at low momentum.
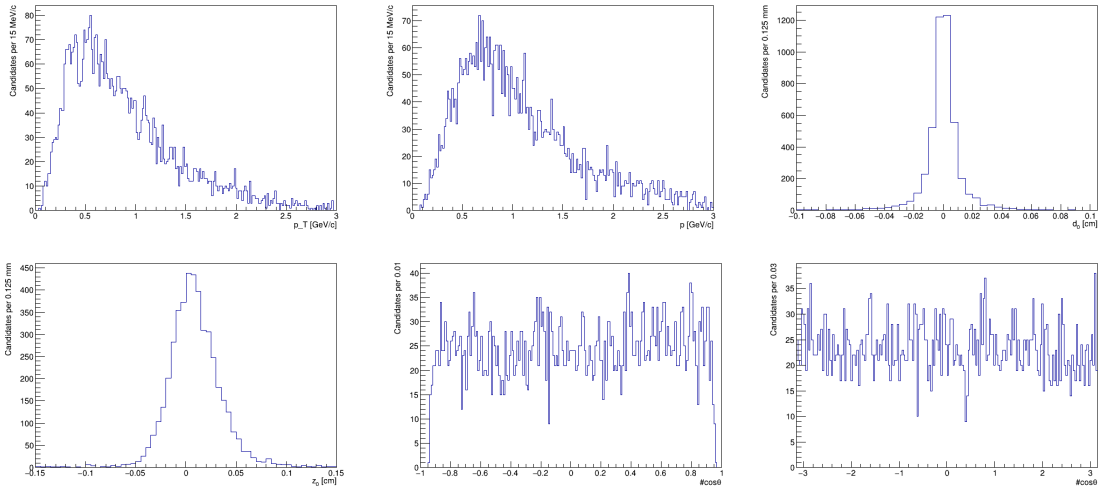


Figure 4.6: Distributions of transverse momentum (top left), total momentum (top middle), impact parameter (top right), longitudinal impact parameter (bottom left), $\cos\theta$ (bottom middle), and $\phi$ (bottom right) of tracks from signal decays in the simulated sample.

As for experimental data, I used the first physics data of Belle II, collected between March and June 2019, and processed with the standard calibration and alignment constants prepared for the 2019 Lepton-Photon conference. Due to delays in the data processing, for this work I could use only about half of the Belle II physics data set, corresponding to an integrated luminosity of about $\approx 3\,\mathrm{fb}^{-1}$.

To determine signal yields, I fitted mass-difference distributions using least-squared fits implemented in ROOT which interfaces with the MINUIT minimizer.

## 4.6   Reconstruction and selection

The standard Belle II reconstruction software is used to reconstruct both simulated and experimental data. Conceptually, a software algorithm first reconstructs all tracks in each event assuming the charged-pion mass for them and accounting for all detector alignment and calibration constants. For simplicity, no PID information is used in this work, because PID performances in Belle II 2019 data are not accurately modeled by the simulation. In addition, the PID impact in reducing background in a pion-only final state would be anyhow limited since genuine pions are also the majority of charged particles from background. The reconstructed charged-pion candidates are first selected with baseline requirements,

$|d_0| < 0.5\,\mathrm{cm}$ and $|z_0| < 3\,\mathrm{cm}$, devised for a first clean-up of first data, where these restrictions are shown to reduce strongly the fraction of tracks from beam backgrounds and material interactions. Selected charged-pion candidates are then combined into opposite-sign pairs consistent with decays of $K_S^0$ mesons and further selected through a requirement on the quality of the reconstructed vertex. Partially reconstructed $D^0$ candidates are then reconstructed combining a third charged-pion candidate with the $K_S^0$ candidate, consistent with a $D^0 \rightarrow K_S^0 \pi^\pm [\pi^\mp]$ topology. Partially reconstructed $D^{*+}$ candidates are reconstructed by combining another charged-pion candidate.

Fully reconstructed candidates are obtained similarly, with just the addition of a charge-matched charged-pion candidate both in the $D^0$ and $D^{*+}$ candidate reconstruction. The fact that the probe track is simply combined (by summing the four-momenta) with the partially reconstructed candidate rather than adjoined to the candidate through a vertex fit is important. Only this way the efficiency we measure is genuinely the track finding efficiency, rather than the combination of it with the vertexing efficiency. In principle, our method could be applied both ways, yielding two different efficiency determinations that could be used to achieve an independent determination of the vertexing efficiency.

The mass-difference distributions of the resulting samples are shown in Fig. 4.7. They are dominated by smoothly distributed background with the expected square-root-like increasing trend starting from the kinematic threshold. No mass difference signal is visible at this stage. A further, more discriminating selection is needed to isolate a visible signal from the large combinatorial background dominated by random combinations of multiplets of tracks that meet the baseline and reconstruction requirements.

Given the explorative character of this work, I did not attempt at devising any systematically optimized selection to improve the statistical performance of the method. While such an optimization is certainly feasible and probably useful, it is left to a further development. In this work, I choose to apply selections on straightforward, well-controlled quantities for the sake of robustness and simplicity of the results.
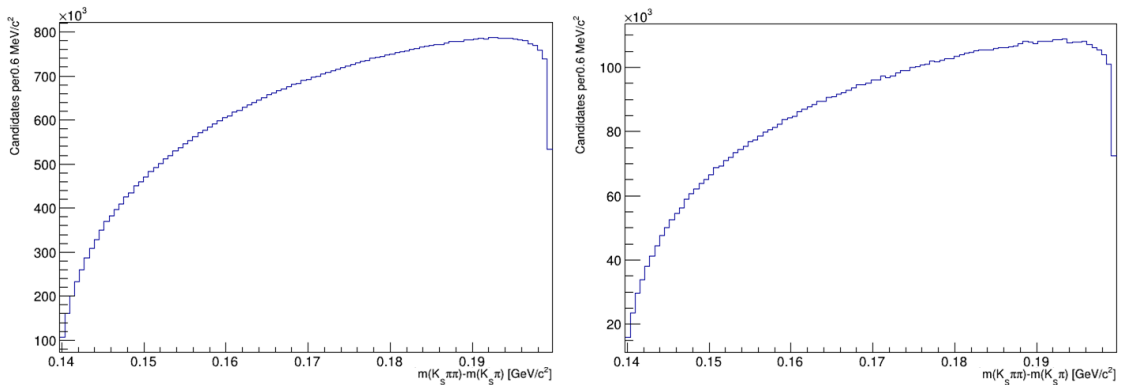


Figure 4.7: Distribution of $D^{*+} - D^0$ mass-difference for fully (left) and partially (right) reconstructed decays from simulated signal-only data subjected to the baseline selection.

### 4.6.1 Combinatorial background suppression

Our signal features a fully reconstructed $K_S^0 \to \pi^+\pi^-$ decay, which has distinctive dipion-mass and decay-length distributions that can be used to discriminate against all combinatorial backgrounds sources that do not generate a $K_S^0$ meson. The $\pi^+\pi^-$ mass distribution for simulated signal and background events is shown in Fig. 4.8. The signal component shows the expected narrow peak centered on the known value of the $K_S^0$ mass, while the background is smoothly distributed, with a small residual signal peak, probably due to $K_S^0$ mesons from other $c\bar{c}$ decays or $s\bar{s}$ processes. A simple requirement of $0.494 < m_{K_S^0} < 0.501$ is already sufficient to reject a large fraction of background.
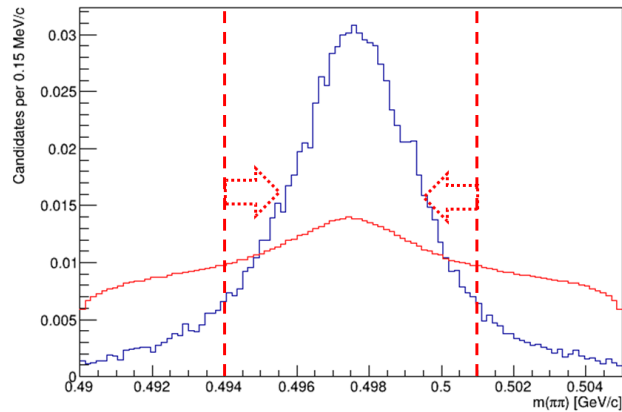


Figure 4.8: Dipion mass distribution for simulated signal (blue) and background (red) events, normalized to each other. The selected range is also shown.

Similarly, the $0.9 \times 10^{-10}$ s $K_S^0$ lifetime, which is long compared to nearly all other unstable particles produced in the collisions, results in a strongly distinctive distribution of $K_S^0$ decay length (Fig. 4.9). A simple requirement on the flight distance to be greater than $0.01$ cm is already a powerfully discriminating condition in reducing the background.
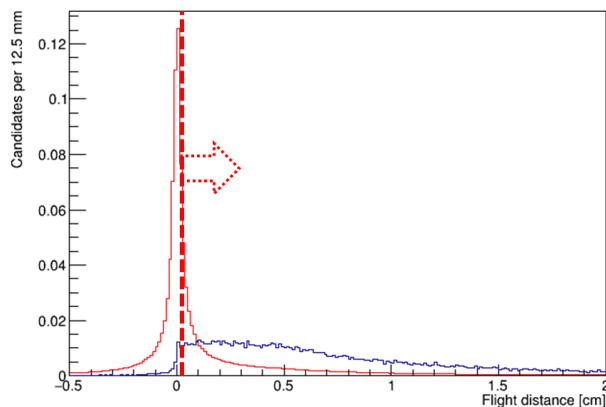


Figure 4.9: Distribution of $K_S^0$ candidate decay-length for simulated signal (blue) and background (red) events, normalized to each other. The selected range is also shown.

In addition, I explored a selection on the momentum of the partially reconstructed $D^{*+}$ meson, calculated in the collision-center-of-mass reference frame to further suppress the combinatorial background. A lower threshold on the momentum of the partially re-

constructed $D^{*+}$ candidate removes a significant fraction of $e^+e^- \rightarrow b\overline{b}$ decays, where decay products are in average less energetic because of the presence of the intermediate $B$ meson produced nearly at rest in the center-of-mass frame. The resulting combinatorial-background reduction is accompanied by a reduction of potentially usable signal events from $e^+e^- \rightarrow b\overline{b} \rightarrow c/\overline{c} + X$ processes, which in principle could contribute precision to the final efficiency result. However, in the sake of simplicity and robustness, the benefit from the combinatorial suppression is certainly preferable in this demonstration of feasibility.
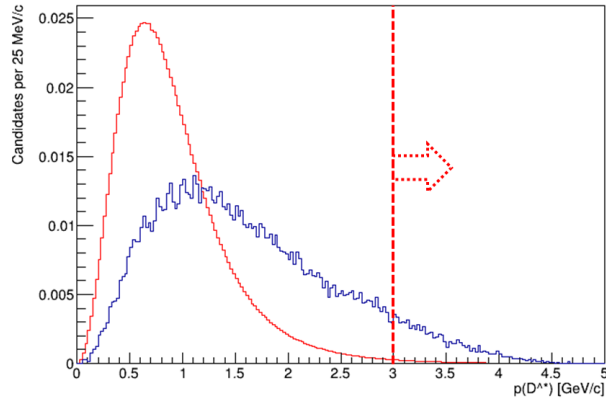


Figure 4.10: Momentum distribution for partially reconstructed $D^{*+}$ candidates in signal (blue) and background (red) events, normalized to each other. The selected range is also shown.

The mass-difference distributions for partially and fully reconstructed simulated candidates resulting from this simple selection are shown in Fig. 4.11. In both plots, a signal-like shape over the smooth background is visible.
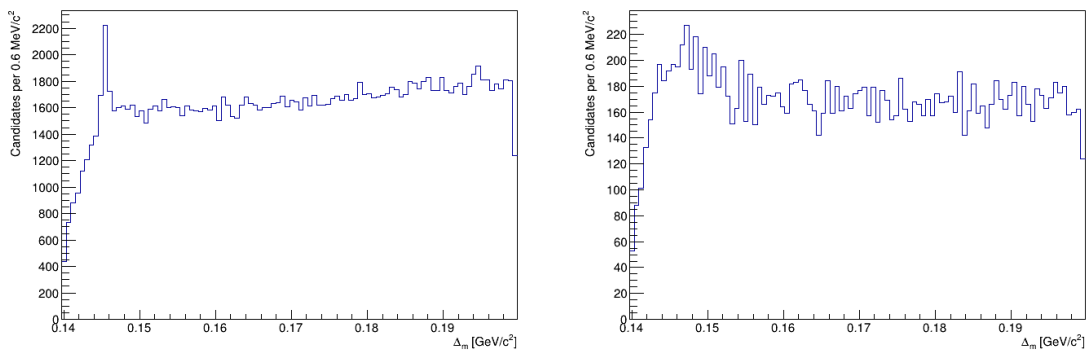


Figure 4.11: Distributions of $D^{*+} - D^0$ mass difference for simulated fully (left) and partially (right) reconstructed events subjected to the combinatorial-background suppression.

### 4.6.2 Peaking background suppression

Now that signal-like excesses are visible, an understanding of the sample composition is essential to check for the presence of peaking-background events. Events with similar mass-difference shape to the signal can not be sufficiently distinguished from the fit, which would absorb their yields into the signal yield, inducing biases in the efficiency results that may go unnoticed. Because of the particular nature of the mass-difference in such a kinematically constrained decay, contributions that peak right where our signal peak with similar width can only be due to $D^{*+} \to D^0 \pi^+$ decays where the topology of the subsequent $D^0$ decay mirrors closely that of our signal, e.g., with five or more final-state tracks, two of which possibly originating from a $K_S^0$. These considerations prompt us to carry a systematic survey of the charm decays that have these features and rates 10% of our signal rate or higher. Such a survey is conducted by searching for known contributions from tabulated charm decay-modes in the MC-truth information. Following this study, I identified the main potential sources of peaking backgrounds in the following modes:

- $D^0 \to K_S^0 K^+ K^-$ ($\mathcal{B} = 0.5\%$);

- $D^0 \to K^- \pi^+ \pi^- \pi^+$ ($\mathcal{B} = 8.1\%$);

- $D^0 \to K_S^0 \pi^+ \pi^- \pi^0$ ($\mathcal{B} = 5.2\%$);

- $D^0 \to K_S^0 \pi^- e^+ \nu_e$ ($\mathcal{B} = 2.7\%$)

Mass-difference distributions for simulated samples of each of these decays individually confirm that these decays contribute in a sizeable manner to both the partially and fully reconstructed samples, as shown in Fig. 4.12. If not adequately suppressed they may introduce biases to the signal yields, and therefore to the efficiencies. Therefore a dedicated selection is needed to reduce contamination from these events.
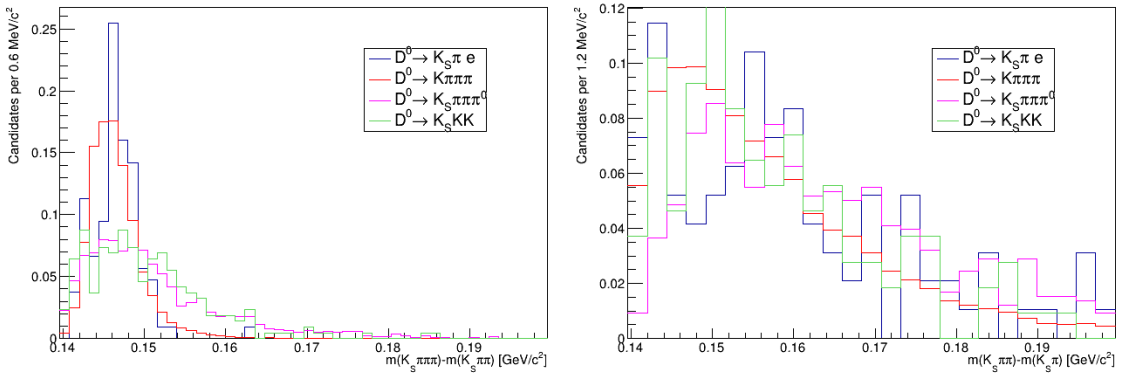


Figure 4.12: Distributions of $D^{*+} - D^0$ mass-difference for simulated fully (left) and partially (right) reconstructed peaking-background decays subjected to the combinatorial-background suppression.

After several trials and a number of possibly discriminating variables explored, we found that the $K_S^0 \pi^+$ mass (where the pion originates from the $D^0$ decay, so that the variable corresponds to the "visible mass" of the partially reconstructed $D^0$ candidate, $m_{D^0}^{\mathrm{PR}}$) carries significant discriminating information between signal and peaking backgrounds. In fact, misreconstruction or missed reconstruction of $D^0$ tracks typically results in lower values of the mass of partially reconstructed $D^0$ candidates as shown in 4.13. The requirement $m_{D^0}^{\mathrm{PR}} > 1.4 \, \mathrm{GeV}/c^2$ is highly effective in reducing the yield of such processes. In addition, it reduces further the combinatorial background contamination even though it also impact

the signal yield. In a further refinement of this work, a dedicated strategy at suppressing these background might found alternative requirements that are less punitive on the signal.
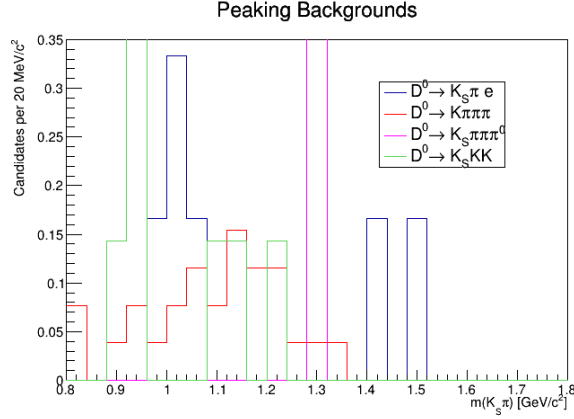


Figure 4.13:  Distribution of $K_S^0\pi$-mass ("partially reconstructed $D^0$ mass", $m_{D^0}^{\mathrm{PR}}$) for partially reconstructed simulated peaking-background decays subjected to the combinatorial-background suppression.

### 4.6.3   Final sample

The mass-difference distributions for partially and fully reconstructed candidates in simulated samples after the full selection are shown in Fig. 4.14. Prominent signals are visible over the smooth backgrounds fully dominated by the combinatorial component. At this stage, the combinatorial background is dominated by genuine $D^0$ decays associated with random soft pions that form erroneously reconstructed $D^{*+}$ candidates.

Before moving onto the efficiency determination, we checked for the presence and frequency of multiple candidates per event. Multiple candidates are particularly an issue in the partially reconstructed signal because their presence can bias the efficiency measurement. After the full selection, less than 5 % of the events had multiple candidates, and for these, I randomly chose one. Multiple candidates are less of a concern in the fully reconstructed sample because kinematics imposes that only the truly reconstructed candidate, if any, contributes to the much narrower $D^{*+} - D^0$ mass-difference signal. Contamination from other possible candidates distributed along the smooth background is expected to be properly accounted for by the fit, which correctly classify them as background.
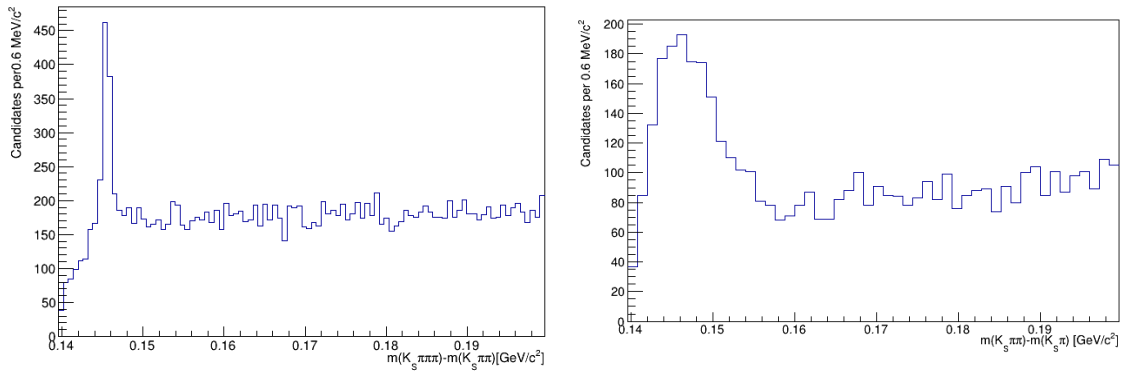
Figure 4.14: Distributions of $D^{*+} - D^0$ mass difference for simulated fully (left) and partially (right) reconstructed candidates, after application of the full selection.
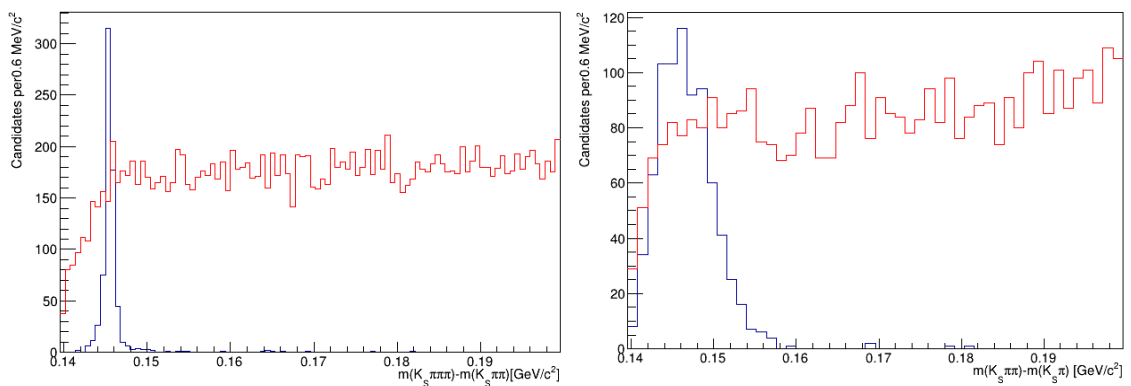


Figure 4.15: Distributions of $D^{*+} - D^0$ mass difference for simulated signal (blue) and background (red) fully (left) and partially (right) reconstructed candidates, after application of the full selection.

## 4.7 Fit of the partially reconstructed sample

To devise an adequate fit model, I studied separately signal and background components, as shown in Fig. 4.16. The mass-difference peak is approximated with a Breit-Wigner distribution convoluted with a Gaussian to account for tracking resolution effects. For the combinatorial background model, I used a function that empirically parametrizes the observed shape in the signal region, found to be

$$f(\Delta_m) = \left[1 - e^{-\frac{(\Delta_m - m_0)}{C}}\right]\left(\frac{\Delta_m}{m_0}\right)^A + B\left(\frac{\Delta_m}{m_0} - 1\right),$$

with free parameters $A$, $B$, $C$ and $m_0$, complemented with a 2nd-degree polynomial component to parametrize the background at higher mass-difference values.
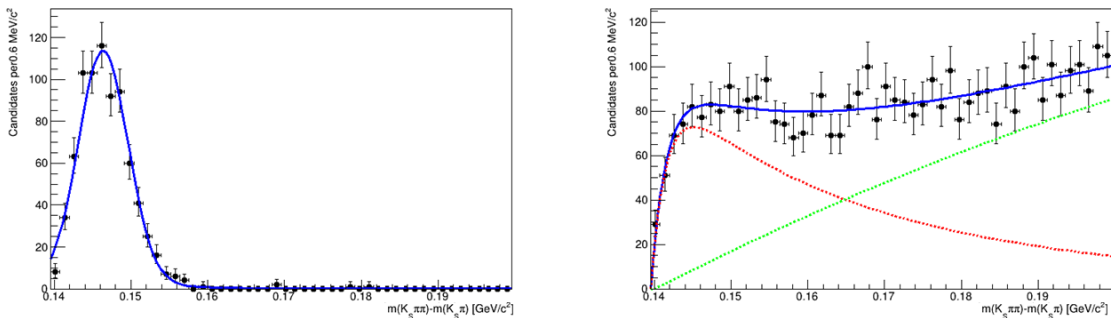


Figure 4.16: Mass-difference distributions for partially reconstructed, simulated signal (left) and background (right) candidates with the corresponding fit model overlaid.

I defined the total fit function as the sum of the models used in these fits and fixed all the shape parameters, leaving as free parameters to be determined by the fit just the yields of the two contributions, to minimize the variance of the efficiency measurement. The result of the fit is show in Fig. 4.17.
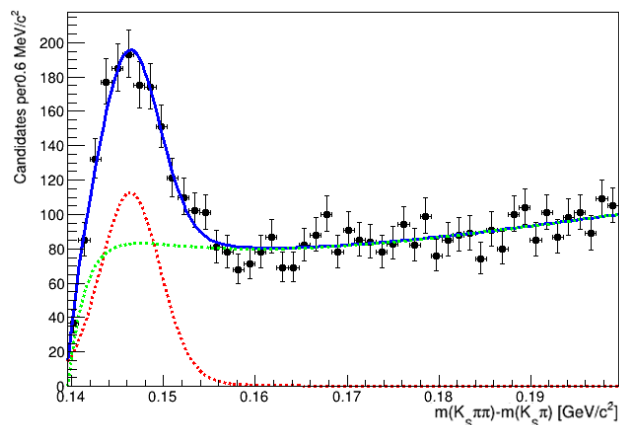


Figure 4.17: Mass-difference distributions for partially reconstructed, simulated candidates with fit projections overlaid.

## 4.8 Fit of the fully reconstructed sample

I selected partially reconstructed candidates and combined them with all other pions in the same event, to reconstruct fully reconstructed decays. The fit function is constructed using the same models as in the partially reconstructed sample.
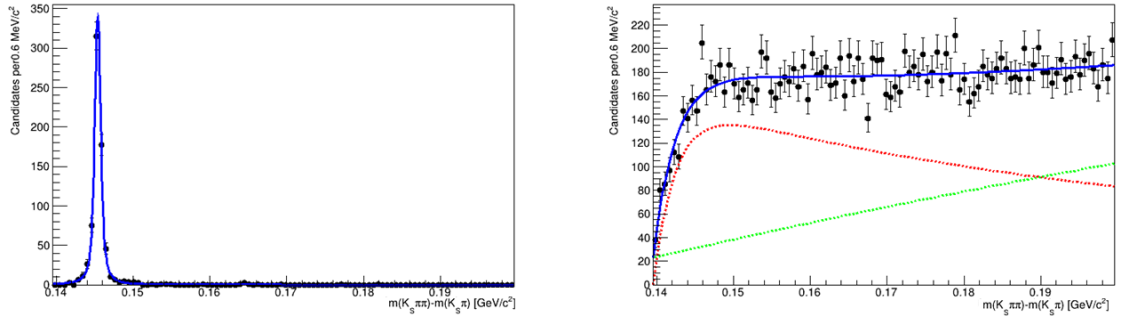


Figure 4.18: Mass-difference distributions for fully reconstructed, simulated signal (left) and background (right) candidates with the corresponding fit model overlaid.

I fitted the distribution with all shape parameters fixed and obtained fully reconstructed signal and background yields. The result of the fit is show in Fig. 4.19.
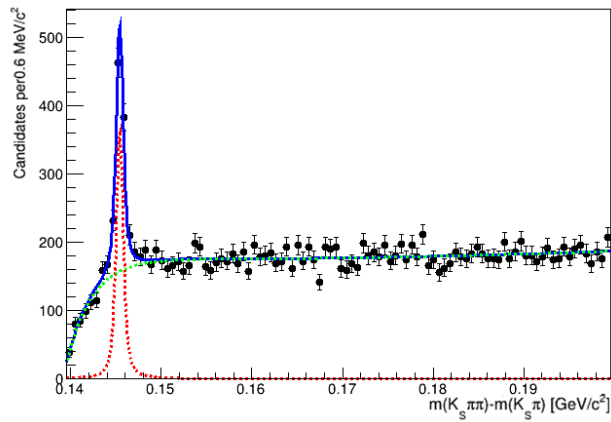


Figure 4.19: Mass-difference distributions for fully reconstructed simulated candidates with fit projections overlaid.

## 4.9  Efficiency determination

The track-finding efficiency for unbiased pions integrated over the tracking volume and data-taking time is determined as

$$\varepsilon = \frac{n_{\mathrm{FR}}}{n_{\mathrm{PR}}} = \frac{n_{\mathrm{ON}}}{n_{\mathrm{TOT}}},$$

where $n_{\mathrm{ON}}$ and $n_{\mathrm{TOT}}$ are, respectively, the signal yields determined by the fit from the mass-difference distribution in the fully and partially reconstructed samples. I found $n_{\mathrm{FR}} = 742 \pm 40$ and $n_{\mathrm{PR}} = 771 \pm 59$. Hence, with the results of the fits of partially and fully reconstructed simulated samples, I estimate the efficiency to be $\hat{\varepsilon} = 0.96$.

The evaluation of the uncertainties is not straightforward. In a general counting experiment the efficiency has a binomial distribution and would have a standard deviation $\sigma_{\varepsilon} = \sqrt{(\varepsilon\,(1-\varepsilon)\,/n_{\mathrm{TOT}})}$, where $\varepsilon$ is the real efficiency, not the estimated one $\hat{\varepsilon}$. Our case, however, is different, as the total number of trials is not known exactly but determined with a fit.

The ideal solution in this case would be to define the efficiency as $\varepsilon = \frac{n_{\mathrm{ON}}}{n_{\mathrm{TOT}}} = \frac{n_{\mathrm{ON}}}{n_{\mathrm{ON}}+n_{\mathrm{OFF}}}$, with $n_{\mathrm{ON}} = \varepsilon n_{\mathrm{TOT}}$ and $n_{\mathrm{OFF}} = (1-\varepsilon)\,n_{\mathrm{TOT}}$ and to fit simultaneously the $n_{\mathrm{ON}}$ and $n_{\mathrm{OFF}}$ yields using the efficiency as a free parameter, so that the fit would directly estimate statistical uncertainty, properly accounting for the correlations. This procedure is under study but it was not ready yet to be implemented.

Hence, we estimate an upper limit to the statistical uncertainty by assuming $n_{\mathrm{ON}}$ and $n_{\mathrm{TOT}}$ uncorrelated. This is known to be inaccurate but gives a sufficiently precise information at this stage to compare our results with existing methods.

Systematic uncertainties expected from the possible mismodelings of the fit shapes and residual contaminations from rarer peaking backgrounds are expected to be significantly smaller than the statistical uncertainty and therefore neglected at this stage. The charge-averaged track-finding efficiency for charged pions in data simulated according to early Belle II data-taking conditions is $\hat{\varepsilon} = 0.96 \pm (0.08)$, where the parenthesis around the uncertainty indicates that this has not to be considered a genuine 68.3% confidence-level range due to the approximations assumed in estimating it.

## 4.10   Efficiency in experimental data

After defining the procedure on simulated samples, I applied it to data. Before fitting the higher-level distributions of mass differences, I performed numerous lower-level consistency checks on the basic track variables. An example of these preliminary studies are the distributions of baseline low-level variables in data shown in Fig. 4.20. These are compared to the same variables for simulated data, to check for large inconsistencies that would spoil our strategy of applying in data a procedure devised entirely in simulation. Momentum, transverse momentum and angular distributions are in reasonable to good agreement. On the other hand, variables associated to the coordinates of the point of origin of the track show significant anomalies. Transverse and longitudinal impact parameters in data depart significantly from the expected shapes. This was tracked down to a technical issue of the early Belle II sample, due to erroneous unpacking and storage of informations one the measured position of the collision vertex, which is done centrally. This issue was solved by overriding the erroneously stored interaction-position coordinates with the correct one recovered offline by studying dimuons, but we did not include the correction in our analysis since the impact of the mismatch is marginal, if any, in this work, where no information on the $D^0$ decay length is used. However, in further refinements of the selection, $D^0$ decays lengths might be used to further discriminate against combinatorial backgrounds from light-quark production.
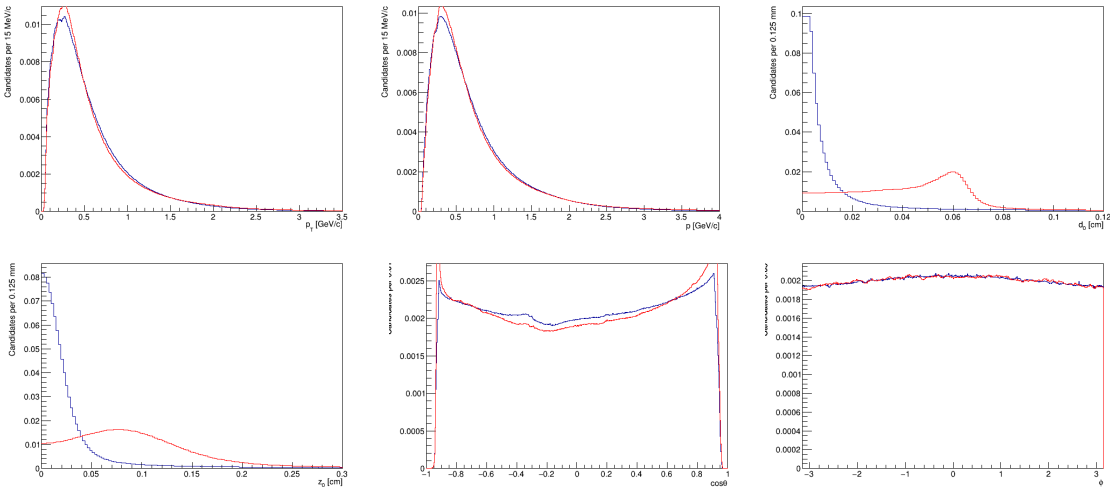


Figure 4.20: Distributions of transverse momentum (top left), momentum (top middle), impact parameter (top right), longitudinal impact parameter (bottom left), $\cos\theta$ (bottom middle), and $\phi$ (bottom right) of tracks from signal decays in the simulated sample (blue) and experimental data sample (red). In each plot, distributions are normalized to each other.

To maintain the procedure unbiased I apply on data the selection devised in simulated samples using the same code. I also used the same model to fit the $D^{*+} - D^0$ mass-difference distributions, and provide an upper estimate of the uncertainty using the same approximation of uncorrelated $n_{ON}$ and $n_{TOT}$. Mass-difference distributions of candidates fully and partially reconstructed from spring 2019 Belle II experimental data are shown in Figs. 4.21 and 4.22, respectively, with fit results overlaid. The fit determines a fully reconstructed signal yield of $n_{FR} = 293 \pm 31$ decays out of $n_{PR} = 311 \pm 43$ partially reconstructed signal decays.

The resulting charge-averaged track-finding efficiency for charged pions reconstructed

in Belle II early data is

$$\varepsilon = 0.94 \pm (0.16), \tag{4.1}$$

where the parenthesis around the uncertainty indicates that this has not to be considered a genuine 68.3% confidence-level range, due to the approximations assumed in estimating it. Within its generous uncertainty, this result is consistent with the results determined on simulation and with independent, but more precise, determinations made using Bhabha and $\tau$-lepton-pair events. We emphasize that the scientific impact of this work does not reside on the precision of the above determination. Quoting the numerical result aims chiefly at demonstrating with a quantitative figure that the method works, and has a promising reach, especially when the numerous approximations and simplifications associated with this first study will be refined.
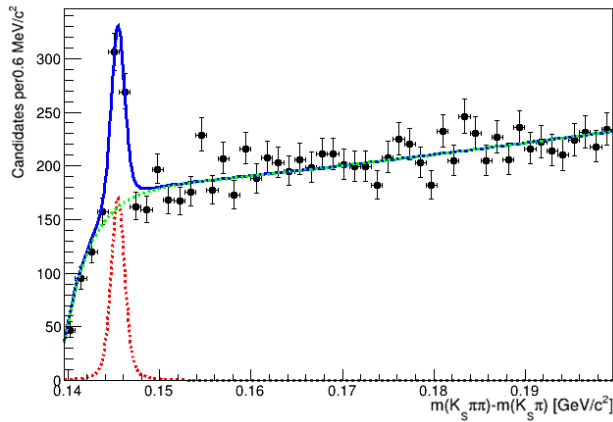


Figure 4.21: Distribution of $D^{*+} - D^0$ mass difference for decays fully reconstructed in Belle II data collected in spring 2019 and corresponding to an integrated luminosity of 3 fb$^{-1}$ sample with fit projections overlaid.
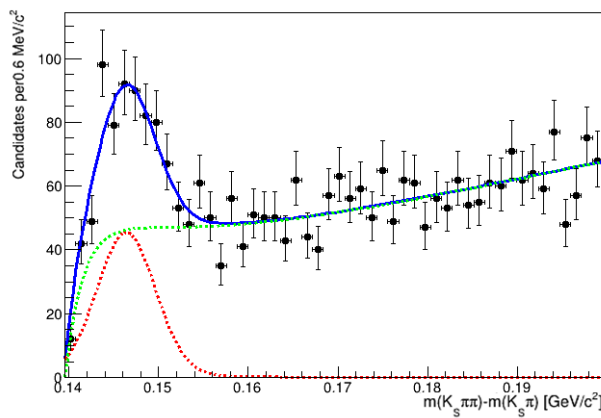


Figure 4.22: Distribution of $D^{*+} - D^0$ mass difference for decays partially reconstructed in Belle II data collected in spring 2019 and corresponding to an integrated luminosity of 3 fb$^{-1}$ sample with fit projections overlaid.

## 4.11 Impact on tracking

Having demonstrated the feasibility and promising performances of a conceptually novel method to determine track-finding efficiency has a very significant impact on Belle II tracking. This method, unlike current Belle II approaches, measures track-finding efficiency with no input from simulation and allows for probing charged-particle momenta down to 0.5 GeV/$c$ and less, where a thorough understanding of track-finding efficiency is most critical, since in that kinematic regime charged particles are subjected to stronger multiple scattering, contributing to higher pattern-recognition and track-fitting inefficiencies. Developments and refinements are already in progress to exploit the understanding of the sample we gained in a properly optimized selection that enhances the efficiency determination and allows measuring it precisely as a function of a number of relevant variables including particle charge, data-taking time, momentum position in the tracking volume, and so forth. In addition, the method applicability is not restricted to Belle II, but can in principle be extended to all experiments where high-rate charm-decay samples can be collected and fully reconstructed.

# Summary

The Belle II experiment, with its target of nearly 1000 collected $B$-meson decays per second and a newly upgraded detector, will co-lead the progress in flavor physics for the next decade, guiding the next steps in indirect searches for the completion of the Standard Model at the intensity frontier. An efficient and precise charged-particle tracking performance is key for the Belle II physics program. Precise measurements of charged-particle momenta yield precise determination of signal invariant masses, which are the main discriminators against backgrounds. Precise determinations of decay times of long-lived particles are essential ingredients in many crucial flavor measurements. Not only tracking performances should be optimized; they also need to be protected from the intense radiation environment that pervades the inner layers of the tracking detectors.

My work, conducted for a large portion in Japan during early physics data-taking, improved significantly the tracking performance with two synergic and complementary contributions. My improvements of the diamond radiation-monitoring and beam-abort system greatly streamlined the Belle II operations while optimizing protection from radiation. This ensured safe and efficient data-taking extending the long-term operational lifetime of the tracking system. My original contributions to the determination of tracking efficiency provide Belle II with a novel instrument, solely based on data, which probes a previously inaccessible momentum regime. The main achievements of my work are

- increased data-taking efficiency and extended lifetime of tracking detectors, thanks to my improvements and optimizations of the operating-configuration of the radiation monitoring system;

- a safer and robust detector protection from exceptional radiation events, thanks to detailed, data-motivated configurations of diamond-detector pedestal and threshold settings;

- a deeper insight into the beam-background composition in SuperKEKB, thanks to my work of correlating offline diamond data with the accelerator parameters;

- the development and introduction in Belle II of a novel method to determine track-finding efficiency, which offers a supplementary approach that use no input from simulation and has unique reach at low momentum;

In mid-October Belle II will resume physics data taking. The higher target luminosities will pose renewed challenges to the detector operations, but my improvements to the diamond system will continue to be essential to protect the silicon detector and ensure safe and efficient data taking. In addition, the larger expected data-set size will allow for applying my tracking-efficiency approach with enough resolution to study efficiency as a function of time and track-position. All of this is expected to have a significant long-term impact in the quality of the physics produced by Belle II.

The work of this thesis is being documented in one internal Belle II document and on two technical papers in preparation.

# Bibliography

[1] To a good approximation, the attractive force between quarks grows linearly with distance. As two quarks are separated, putting energy into the bounded system, it becomes energetically favorable for a new quark–antiquark pair to appear, rather than extending the distance further. As a consequence new bounded states are generated instead of separeted and free quarks.

[2] M. S. Sozzi, *Discrete symmetries and CP violation: From experiment to theory.* Oxford University Press, 1st ed., 2008.

[3] D. Tonelli, *Flavor physics to overcome the Standard Model*, Phd school trieste, 2018. `https://wwwusers.ts.infn.it/~dtonelli/FlavorPhysics/`.

[4] M. Tanabashi et al., Particle Data Group, *Review of Particle Physics*, Phys. Rev. D **98** (2018) 030001.

[5] M. Gell-Mann and M. Lévy, *The axial vector current in beta decay*, Il Nuovo Cimento (1955-1965) **16** (May, 1960) 705–726.

[6] N. Cabibbo, *Unitary Symmetry and Leptonic Decays*, Phys. Rev. Lett. **10** (1963) 531–533.

[7] S. L. Glashow, J. Iliopoulos, and L. Maiani, *Weak Interactions with Lepton-Hadron Symmetry*, Phys. Rev. D **2** (Oct, 1970) 1285–1292.

[8] M. Kobayashi and T. Maskawa, *CP-Violation in the Renormalizable Theory of Weak Interaction*, Prog. Theor. Phys. **49** (1973) 652–657.

[9] A general $N{\times}N$ complex matrix $U$ is defined with $2N^2$ free parameters. The unitary condition $UU^\dagger = \mathbb{1}$ eliminates $N^2$ degrees of freedom. We can then redefine $(N-1)$ quark fields to absorb $(N-1)^2$ free parameters.
We end up with $2N^2 - N^2 - (2N-1) = (N-1)^2$ free parameters.

[10] L. Wolfenstein, *Parametrization of the Kobayashi-Maskawa Matrix*, Phys. Rev. Lett. **51** (Nov, 1983) 1945–1947.

[11] M. Gell-Mann and A. Pais, *Behavior of Neutral Particles under Charge Conjugation*, Phys. Rev. **97** (Mar, 1955) 1387–1389.

[12] Y. Ahmis et al., Belle II Collaboration, *Averages of b-hadron, c-hadron, and $\tau$-lepton properties as of summer 2016*, The European Physical Journal C **77** (2017) no. 12, 895.

[13] CKMfitter Group (J. Charles et al.). Eur. phys. j. c41, 1-31 (2005) [hep-ph/0406184], updated plots available at: `http://www.ni.com/white-paper/4752/en/`.

[14] R. Aaij et al., LHCb Collaboration, *Observation of CP Violation in Charm Decays*, Phys. Rev. Lett. **122** (2019) no. 21, 211803, `arXiv:1903.08726 [hep-ex]`.

[15] Belle II Collaboration and B2TiP theory Community, *The Belle II Physics Book*. Prog. Theor. Exp. Phys., 1st ed., 2018.

[16] Y. Ohnishi et al., *Accelerator design at SuperKEKB*, Prog. Theo. Exp. Phys. **2013** (2013) 03A011.

[17] Raimondi et al., *Beam-beam issues for colliding schemes with large Piwinski angle and crabbed waist*, arXiv e-print (2007) , `arXiv:physics/0702033`.

[18] C. Marinas, DEPFET, *The Belle II pixel detector: High precision with low material*, Nucl. Instrum. Meth. **A731** (2013) 31–35.

[19] K. Adamczyk et al., Belle-II SVD Collaboration, *The Belle II silicon vertex detector assembly and mechanics*, Nucl. Instrum. Meth. **A845** (2017) 38–42.

[20] N. Taniguchi, Belle II Collaboration, *Central Drift Chamber for Belle-II*, JINST **12** (2017) no. 06, C06014.

[21] K. Inami and I. Belle, *TOP counter for particle identification at the Belle II experiment*, Nuclear Instruments and Methods in Physics Research Section A: Accelerators, Spectrometers, Detectors and Associated Equipment **766** (2014) 5–8.

[22] S. Iwata et al., *Particle identification performance of the prototype aerogel RICH counter for the Belle II experiment*, PTEP **2016** (2016) no. 3, 033H01, `arXiv:1603.02503 [physics.ins-det]`.

[23] V. Aulchenko et al., *Electromagnetic calorimeter for Belle II*, J. Phys. Conf. Ser. **587** (2015) no. 1, 012045.

[24] A. Abashian et al., Belle Collaboration, *The K(L) / mu detector subsystem for the BELLE experiment at the KEK B factory*, Nucl. Instrum. Meth. **A449** (2000) 112–124.

[25] T. Abe et al., Belle II Collaboration, *Belle II Technical Design Report*, ArXiv e-prints (2010) , `arXiv:1011.0352`.

[26] P. M. Lewis et al., *First Measurements of Beam Backgrounds at SuperKEKB*, arXiv e-prints (2018) , `arXiv:1802.01366`.

[27] L. Vitale, *The Belle II Silicon-strip Vertex Detector*, in *Vertex 2014*, p. 017. 2015.

[28] V. Re et al., *Radiation damage studies for the BaBar Silicon Vertex Tracker*, Nucl. Instrum. Meth. A **549** (2005) 11 – 15.

[29] T. I. Meyer, *PIN photodiodes for radiation monitoring and protection in the BABAR Silicon Vertex Tracker*, Int. J. Mod. Phys. **A16S1C** (2001) 1084–1086.

[30] D. Zontar, *Radiation monitoring at Belle*, Nucl. Instrum. Meth. **A501** (2003) 164–166.

[31] R. Muller and T. I. Kamins, *Device Electronics for Integrated Circuits*. Wiley, 3rd ed., 2002.

[32] E. Berdermann, *Diamond for Particle and Photon Detection in Extreme Conditions*, p. 407–467. Elsevier Science, 2014.

[33] National Instruments, *Virtual Instrumentation*, `http://www.ni.com/white-paper/4752/en/`.

[34] R. Aaij et al., *Measurement of the flavour-specific CP-violating asymmetry asls in Bs0 decays*, Physics Letters B **728** (2014) 607 − 615.

[35] B. Bhuyan, *High-pT tracking efficiency using partially reconstructed D\* decays*, Belle Note **1165** (2010) .